

AD-A108 555

GRUMMAN AEROSPACE CORP BETHPAGE NY RESEARCH DEPT  
INVESTIGATION OF LARGE CAPACITY OPTICAL MEMORIES FOR CORRELATOR--ETC(U)

F49620-78-C-0051

F/G 9/2

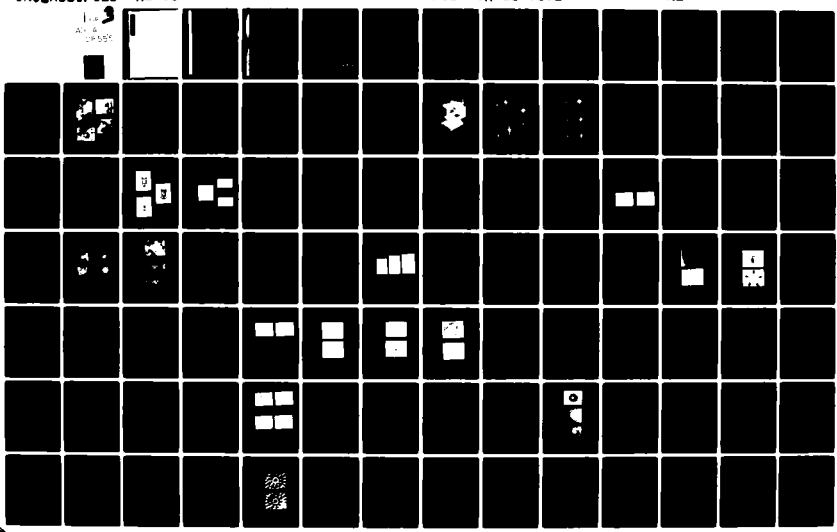
UNCLASSIFIED

OCT 81 K G LEIB, J MENDELSON

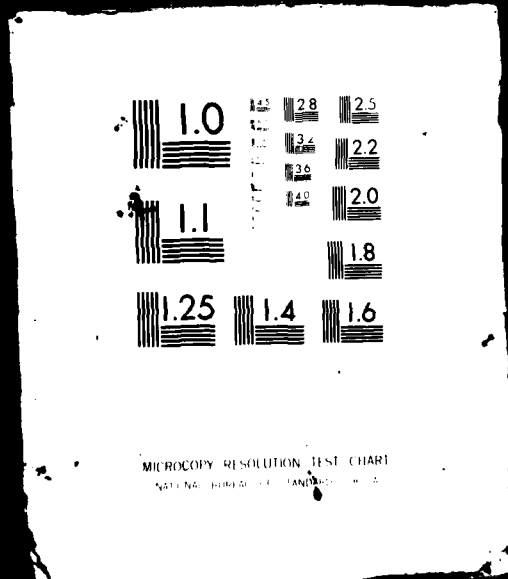
AFOSR-TR-81-0802

NL

RE-634  
1-2  
A-1  
2-551



1 OF  
AD-A  
108555



ADA108555

Unclassified

SECURITY CLASSIFICATION OF THIS PAGE (When Data Entered)

REPORT DOCUMENTATION PAGE		READ INSTRUCTIONS BEFORE COMPLETING FORM
1. REPORT NUMBER <b>AFOSR-TR- 31-0802 AD-A10855</b>	2. GOVT ACCESSION NO.	3. RECIPIENT'S CATALOG NUMBER
4. TITLE (and Subtitle) Investigation of Large Capacity Optical Memories for Correlator Applications	5. TYPE OF REPORT & PERIOD COVERED Final Technical Report April 1, 1978-March 31, 1981	
7. AUTHOR(s) Kenneth G. Leib and Jay Mendelsohn	6. PERFORMING ORG. REPORT NUMBER 14620 78-C-0051	
9. PERFORMING ORGANIZATION NAME AND ADDRESS Grumman Aerospace Corporation Research Department, A08/35 Bethpage, New York 11714	10. PROGRAM ELEMENT, PROJECT, TASK AREA & WORK UNIT NUMBERS <b>61102F 2305/B2</b>	
11. CONTROLLING OFFICE NAME AND ADDRESS AFOSR/NE Building 410, Bolling AFB Washington, D.C. 20332	12. REPORT DATE August 1981	
14. MONITORING AGENCY NAME & ADDRESS (if different from Controlling Office)	13. NUMBER OF PAGES <b>157</b>	
	15. SECURITY CLASS. (of this report) Unclassified	
	15a. DECLASSIFICATION/DOWNGRADING SCHEDULE	
16. DISTRIBUTION STATEMENT (of this Report) Approved for Public Release; Distribution Unlimited		
17. DISTRIBUTION STATEMENT (of the abstract -- insert if block 16 is different from Report)		
18. SUPPLEMENTARY NOTES		
19. KEY WORDS (Continue on reverse side if necessary and identify by block number) Correlators, Optical Dichromated Gelatin Optical Signal/Clutter Ratio	Optical Match Filtering Optical Target Detection Memory Capacity	
20. ABSTRACT (Continue on reverse side if necessary and identify by block number) The purpose of this program was to investigate large capacity optical memories for correlator applications. The basic memory element, the matched filter, was examined in a number of configurations. These included coherent and non-coherent addition, split spectrum, and multiplexed carriers. Three different storage materials were examined: silver halide, dichromated gelatin, and photopolymers. Both thin and thick holographic memories were studied.		

DD FORM 1 JAN 73 1473

EDITION OF 1 NOV 68 IS OBSOLETE  
S/N 0102-014-6601

Unclassified

4116 161 SECURITY CLASSIFICATION OF THIS PAGE (When Data Entered)

Unclassified

SECURITY CLASSIFICATION OF THIS PAGE(When Data Entered)

20. ABSTRACT (contd)

The matched filters were evaluated using complex terrains such as woodlands, roadsides, and villages in which the principal targets (i.e., tanks, trucks and armored personnel carriers) were located. For each terrain and target, the signal-to-clutter ratio (s/c) was measured. These ranged from 5.5 to 11 dB for the target-terrain combinations studied. The complex matched filters that achieved these s/c's were recorded in dichromated gelatin.

It was shown that more than 5 matched filters could be non-coherently added and 15 could be coherently added in the same memory position. In addition, it was demonstrated that carrier multiplexing could be used to achieve 30 matched filters per memory position. It is also shown that the theoretical limit for memory density of matched filters is  $2670 \text{ MF/cm}^2$ . This is equivalent to 1,000,000 bits of digital data. Various modifications of the basic optical matched filter were studied for the purpose of improving s/c ratio and increasing the storage density.

A mathematical model of the optical matched filter and its variations was developed based on the two-dimensional Fourier Transform. This model was used to simulate the optical device digitally. The output of the digital simulation showed excellent agreement with the optical device, using both visual and quantitative measures. The simulation allowed for the parametric study of the optical device under controlled conditions and in much less time than could have been achieved in a laboratory setting. Several digital studies aimed at optimizing the detection capability of the correlator are presented, and the results are compared with those obtained from the optical correlator.

Unclassified

SECURITY CLASSIFICATION OF THIS PAGE(When Data Entered)

Grumman Research Department Report RE-634

INVESTIGATION OF LARGE CAPACITY OPTICAL MEMORIES  
FOR CORRELATOR APPLICATIONS

Kenneth G. Leib and Jay Mendelsohn  
Research Department  
Grumman Aerospace Corporation  
Bethpage, New York 11714

October 1981

Accession For	
NTIS GRA&I	<input checked="" type="checkbox"/>
DTIC TAB	<input type="checkbox"/>
Unannounced	<input type="checkbox"/>
Justification	
By _____	
Distribution/	
Availability Codes	
Dist	Avail and/or Special
A	

Final Technical Report 1 April 1978 - 31 March 1981

Approved for Public Release  
Distribution Unlimited

Prepared for

AIR FORCE OFFICE OF SCIENTIFIC RESEARCH  
Bolling Air Force Base  
Washington, DC 20332

AIR FORCE OFFICE OF SCIENTIFIC RESEARCH (AFSC)  
NOTICE OF TRANSMITTAL TO DTIC  
This technical report has been reviewed and is  
approved for public release IAW AFR 190-12.  
Distribution is unlimited.  
MATTHEW J. KERPER  
Chief, Technical Information Division

Approved by

Richard A. Scheuing  
Director of Research

*Richard A. Scheuing*

## TABLE OF CONTENTS

<u>Section</u>		<u>Page</u>
1	<b>INTRODUCTION</b>	1-1
2	<b>DESCRIPTION</b>	2-1
2.1	Experimental Setup	2-1
2.2	Simulation Validation	2-1
2.3	Matched Filter Formation and Playback	2-11
3	<b>TECHNIQUES FOR RECORDING MEMORY ELEMENTS</b>	3-1
3.1	Geometrical Configurations	3-1
3.2	Split Spectrum	3-4
3.3	Matched Filter Additions	3-7
3.3.1	Noncoherent Addition	3-15
3.3.2	Coherent Addition	3-15
3.3.3	5X COH and Non-COH Comparisons	3-24
3.3.4	Multiplexed Carriers	3-41
4	<b>MEMORY RECORDING MEDIA</b>	4-1
5	<b>OPTICAL MEMORY CAPACITY</b>	5-1
5.1	Capacity Based Upon Frequency Content of MF	5-1
5.2	Capacity Based Upon Film Limits	5-3
6	<b>SUMMARY</b>	6-1
7	<b>REFERENCES</b>	7-1
8	<b>PROFESSIONAL ACTIVITIES</b>	8-1
9	<b>PERSONNEL</b>	9-1
 <u>Appendices</u>		
A	Use of Dichromated Gelatin for Matched Filters	A-1
B	Construction of Multicapacity Matched Filters Using Birefringent Object Film	B-1
C	Kowarschik's Equations for Sequentially Stored Gratings	C-1
D	The Fourier Transform of Coherently Added Images	D-1
E	Additional Simulations	E-1
F	Analysis of an Optical Matched Filter Guidance System for Tactical Housing Applications	F-1

## LIST OF ILLUSTRATIONS

<u>Figure</u>		<u>Page</u>
1-1	Optical Matched Filter Image Correlator . . . . .	1-2
1-2	Details Of An Offset Memory . . . . .	1-4
1-3	Terrain Scenes Used In Program . . . . .	1-5
1-4	Cumulative Distribution Function Of Cross Correlation (Tank vs. Terrain Scenes) . . . . .	1-6
2-1	Arrangement For Matched Filter Fabrication, S/C And Correlation Measurements . . . . .	2-2
2-2	Matched Filter Holder . . . . .	2-3
2-3	Analog Version of (Fourier Transforms) <sup>2</sup> At Two Exposures . . .	2-4
2-4	Digital Version of (Fourier Transforms) <sup>2</sup> At Two Exposures . . .	2-5
2-5	M-60 Power Spectrum Scan Perpendicular to Major Tank Axis (Ref 8) . . . . .	2-6
2-6	(FT) <sup>2</sup> of Digitized M-60 Tank Image . . . . .	2-6
2-7	Power Spectrum of Three Digitized Terrain Scenes . . . . .	2-8
2-8	Reimaging of M-60 Matched Filters (Analog) . . . . .	2-12
2-9	Reimaging of M-60 Matched Filters (Digital) . . . . .	2-13
2-10	Normalized Fringe Spacing vs. Spatial Frequency Along Axis M-60 Tank Axis . . . . .	2-14
2-11	Fringe Spacing At $\nu = 0$ For Different Object Position During MF Fabrication . . . . .	2-16
3-1	Techniques For Recording Memory Elements . . . . .	3-2
3-2	Geometrical Placement of Memory Elements . . . . .	3-3
3-3	Comparison of COH/Non-COH M-60 Tank (Fourier Transform) <sup>2</sup> . . . . .	3-8
3-4	Intraelement Interference In A 4X Tank Image MF . . . . .	3-9
3-5	Autocorrelations of M-60 Tank From 5 x 5 Array (All Identical) . . . . .	3-13
3-6	Scan Along Major Tank Axis In Correlation Plane Using 5 x 5 HL Transform Lens . . . . .	3-14
3-7	Non-Coherent Addition At Constant Carrier Frequency . . . . .	3-17

## LIST OF ILLUSTRATIONS (contd)

<u>Figure</u>		<u>Page</u>
3-8	Non-Coherently Added MF in Dichromated Gelatin . . . . .	3-18
3-9	Impulse Response of 5X Image MF in Dichromated Gelatin . . . . .	3-19
3-10	Scan Across Correlation Plane Using 5X Non-COH Matched Filter (Dichromated Gelatin) . . . . .	3-20
3-11	Coherent Arrays . . . . .	3-23
3-12	Autocorrelation of Single M-60 Tank Playing Through 5X Non-COH MF . . . . .	3-25
3-13	Autocorrelation of a Single M-60 Tank Playing Through 5X COH MF . . . . .	3-26
3-14	Autocorrelation Planes When Entire 5X Image Plays Through Non-COH and COH Made Matched Filters . . . . .	3-27
3-15	Correlation Plane of a 5X Non-COH Matched Filter Using SE Asian Terrain Image Input Upon Playback . . . . .	3-28
3-16	5X MF Translational Sensitivity . . . . .	3-32
3-17	X-Positional Sensitivity of 1X and 10X Matched Filters in Thick and Thin Emulsions . . . . .	3-33
3-18	Y-Positional Sensitivity of 1X and 10X Matched Filters in Thick and Thin Emulsions . . . . .	3-34
3-19	Azimuth Angular Response of Thin and Thick Emulsions . . . . .	3-36
3-20	Rotational Sensitivity of Matched Filter . . . . .	3-37
3-21	Correlation Plane of 10X COH MF for Two Terrains . . . . .	3-38
3-22	A S/C Ratio of 15X MF in Dichromated Gelatin Using 3 Terrains . . . . .	3-43
3-23	15X Matched Filter in Dichromated Gelatin . . . . .	3-44
3-24	Limits on Fringe Angles in Thick Media, $N = 1.53$ . . . . .	3-47
3-25	Kowarschik Formulation Applied to $O_R = +10^\circ$ . . . . .	3-49
3-26	Response of Multicarrier Gratings and MF in DCG . . . . .	3-51
3-27	Azimuth Sensitivity of MF with Multiplexed Carrier . . . . .	3-52
3-28	5X MF in DCG with One and Two Carriers . . . . .	3-53
3-29	Response of 15X COH with Two Carrier Frequencies . . . . .	3-54
3-30	S/C Ratio of a Multiplexed Carrier 15X MF in DCG Using SE Asian Scene . . . . .	3-55
4-1	Memory Recording Mechanisms for Media . . . . .	4-2
4-2	Thickness Criteria . . . . .	4-3
4-3	Scan with Microdensitometer of Higher Orders of Matched Filter . .	4-4

## LIST OF ILLUSTRATIONS (contd)

<u>Figure</u>		<u>Page</u>
4-4	200X SEM of 5X COH MF in Dichromated Gelatin . . . . .	4-7
4-5	Efficiency of Recording Medium, $\theta_S = 0$ . . . . .	4-14
4-6	Efficiency of Recording Medium, $\theta_S = \theta_R$ . . . . .	4-15
5-1	Fringe Plane Angles vs. Focal Length $\theta_S = 0$ , $\xi/F = 0$ . . . . .	5-4
5-2	Effect of Finite Resolution of Media on Matched Filter Weighting Function H . . . . .	5-7
6-1	Digital Version of Multiple Array Matched Filter . . . . .	6-3
6-2	2 x 2 Array and Correlation Results . . . . .	6-4
6-3	Optical Memory Requirements . . . . .	6-5

## LIST OF TABLES

<u>Table</u>		<u>Page</u>
2-1 Validation of Simulation Through S/C Ratio Measurement . . . . .	2-9	
2-2 Autocorrelation and S/C Ratio for M-60 in Three Terrains as a Function of the Spatial Frequency Cutoff for 3rd Order MF . . . . .	2-10	
3-1 Split-Spectrum Simulation Results . . . . .	3-5	
3-2 Accuracy of Correlation Location with the Split Spectrum . . . . .	3-6	
3-3 Autocorrelations from Regularly Placed 1X, 4X and 8X Input Objects . . . . .	3-11	
3-4 Effect of Interference on Correlation and S/C Ratio . . . . .	3-12	
3-5 Performance of Non-Coherently Added MF in Dichromated Gelatin . . . . .	3-16	
3-6 Positional Distribution of Autocorrelations of Coherent MF Using Thin Silver Halide . . . . .	3-22	
3-7 5X COH and Non-COH MF Performance . . . . .	3-29	
3-8 S/C Ratio for COH and Non-COH 5X Matched Filters . . . . .	3-30	
3-9 Orientational Sensitivity of Coherent Addition MF . . . . .	3-39	
3-10 S/C Ratio for Multiple COH Matched Filters Using SE Asian Terrain Imagery . . . . .	3-41	
3-11 Range of Carrier Frequencies for a Spatial Frequency Spread of $\pm 9.5$ c/mm . . . . .	3-46	
4-1 Positional Distribution of Autocorrelations of Coherent Matched Filters Using Thick and Thin Emulsions . . . . .	4-5	
4-2 Matched Filter Media Comparison . . . . .	4-8	
4-3 Parameters for Equations 4-2, -3, -4 . . . . .	4-11	
4-4 Average Efficiency for $n_1 = .04$ ; Index Interval: 1.52-1.56 . . . . .	4-12	
4-5 Average Efficiency for $n_1 = .04$ at $N = 1.55$ for Various $\nu$ . . . . .	4-13	
5-1 Unit Capacity for Some Practical Cases . . . . .	5-2	

## 1 - INTRODUCTION

There are a number of potential Air Force applications for which the matched filter optical correlator could provide a significant improvement in performance. Typically these might include missile guidance, smart sensors, and target identification for reconnaissance. The techniques available in Fourier optics and holographic technology make the implementation of two-dimensional matched filters (MF) for correlators a feasible approach to the general problem of multiple pattern or target recognition in any Air Force program concerned with real-time target recognition. Appendix F describes in some detail one such Air Force application within the overall context of this program.

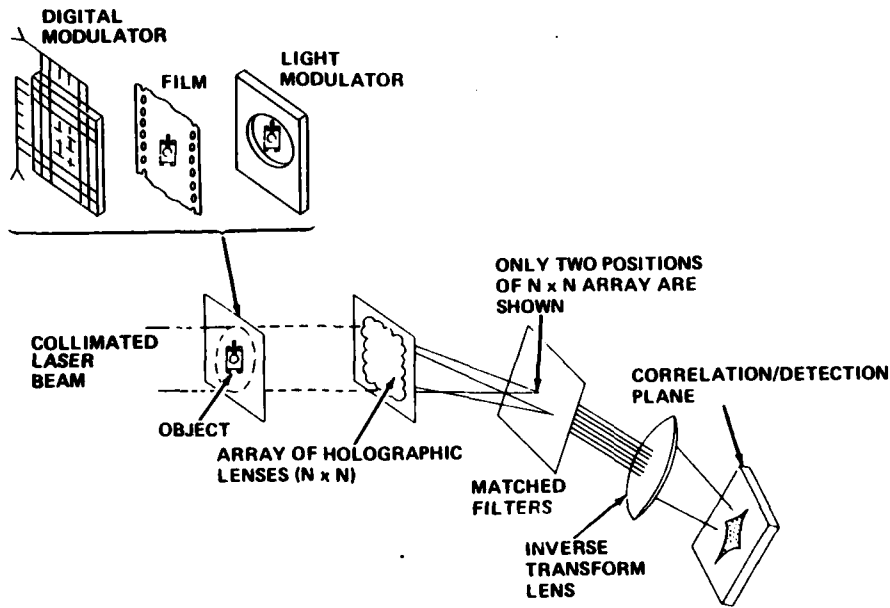
The purpose of this program is to investigate large capacity optical memories for correlator applications (Ref 1). The basic memory element in the correlator is the matched filter.

The essential elements of correlators with coherent optical memories are illustrated in Fig. 1-1 (Ref 2). The Grumman innovation for storing large memories (Ref 3) is to utilize combinations of multiple holographic lenses and MF arrays or memories. High repetition rate input transducers for correlators might soon be available as indicated by recent progress with such devices as microchannel light modulators (Ref 4), CCD array light modulators (Ref 5), and thermoplastic transducers (Ref 6) upon which targets have been imaged.

However derived, the Fourier transform of the object image in Fig. 1-1 is replicated by a multiple holographic lens addressed to a coordinated optical memory bank of matched filters. An inverse transform lens and detector complete the correlator. Our concern is with the matched filter optical memory as part of, and as measured and evaluated in the optical correlator.

The experimental approach taken in this program is one in which various models of a matched filter are constructed, and the parameters affecting their performance determined.

For example, a MF (not limited by optical constraints) has, in principle, an unlimited spatial bandwidth which, in any packing arrangement, would give rise



1283-81-001(T)

Fig. 1-1 Optical Matched Filter Image Correlation

to crosstalk with contiguous matched filters in the memory bank (see Fig. 1-2). Yet, one can predict and verify that a limited filter bandwidth will yield an acceptable signal/clutter (S/C) ratio with little or no crosstalk (Ref 7). This optimization then gives rise to a high packing density. Other parameters affecting filter performance interact with the detection process. In this program, the position is taken that large capacity optical memories are not isolated entities, but large only when the associated correlation signals can be properly detected and used. This is considered an important aspect of Air Force applications.

In this program, the basic target of interest is the US Army M-60 tank, used in an overhead view, and used at different times in various terrains. The latter are shown in Fig. 1-3. Figure 1-3a represents a "SE Asian" scene with competing vehicles; Fig. 1-3b, c and d represent woodland, village, and roadside scenes respectively. Other scenes are occasionally referred to and are described when used. All terrain images were obtained from the US Army 400/1 scaled simulation model located at the Night Vision Laboratory at Fort Belvoir.

Figure 1-4 shows the result of determining the cumulative distribution of the cross correlation between the M-60 tank and the terrain scenes illustrated in Fig. 1-3, b-d. The cross correlation is, of course, a measure of clutter presented by each of the terrains. The abscissa expresses clutter in terms of the ratio of the cross correlation to the autocorrelation. For any particular value of clutter, the corresponding ordinate is the probability that the clutter is less than that value. Therefore, the more steeply rising curve present the least clutter. In the figure we see that for the tank the woodland has the least clutter and the village the most. This is as expected since the village has many more straight edges.

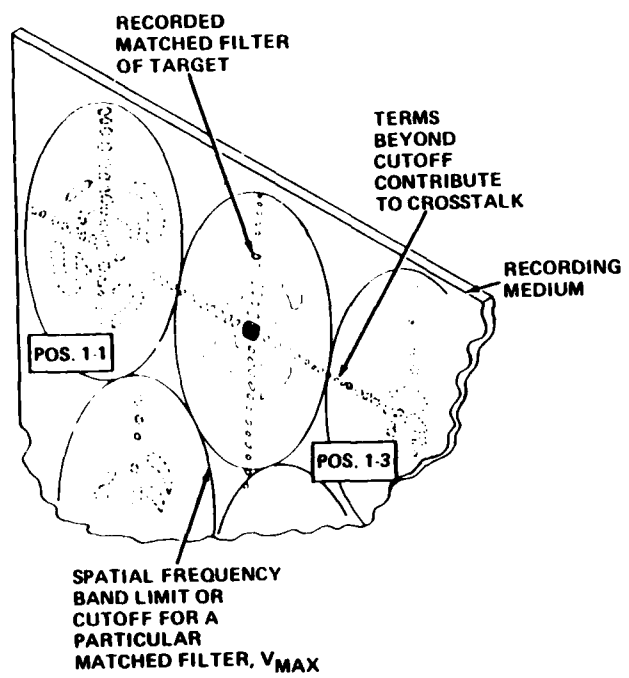
The matched filter is the optimum linear filter for signal detection in white gaussian noise. Optically, the transfer function of the matched filter is  $S^*(v_x, v_y)$ , the complex conjugate of the Fourier transform  $S(v_x, v_y)$  of the desired signal:

$$S(v_x, v_y) = \iint_{-\infty}^{\infty} s(x, y) e^{j\phi_x(x, y)} e^{-i2\pi(v_x x + v_y y)} dx dy \quad (1-1)$$

When interfered with a unit reference beam,  $e^{j\beta\omega_x}$ , it forms the FT hologram or matched filter, MF. The size sensitivity of the filter is:

$$S = v_{x,y} / \xi = (\lambda F)^{-1} \text{ (cycles/mm) per mm} \quad (1-2)$$

$\lambda$  is the wavelength and  $F$  the focal length of the transform lens in Figure 1-1.



1283-81-002(T)

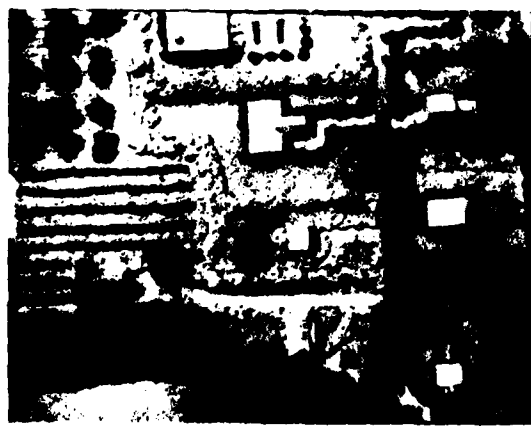
Fig. 1-2 Details of an Offset Memory



(a) SOUTHEAST ASIAN SCENE



(b) WOODLAND SCENE



(c) VILLAGE SCENE



(d) ROADSIDE

1283-81-003(T)

Fig. 1-3 Terrain Scenes Used in Program

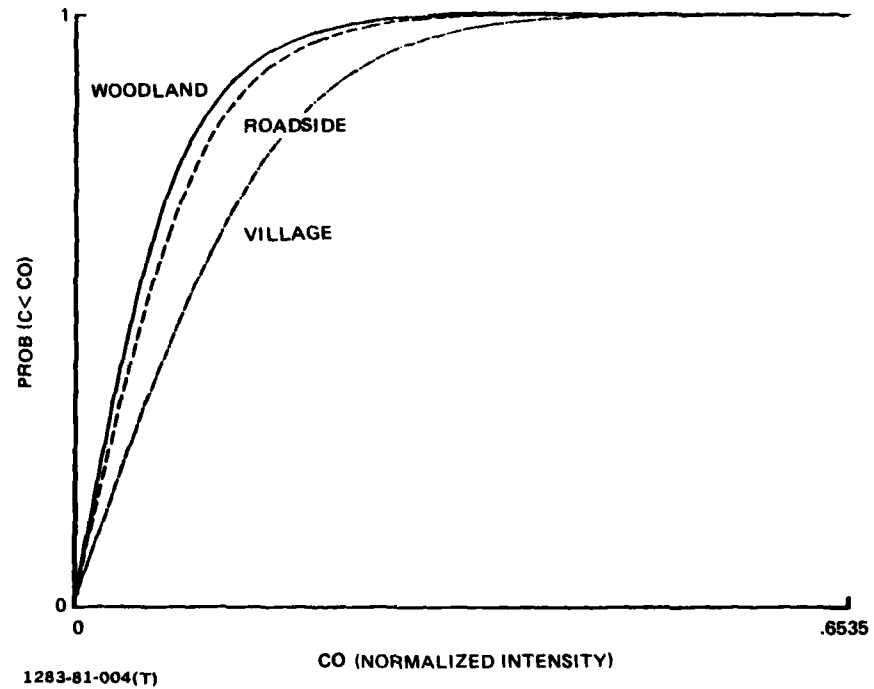


Fig. 1-4 Cumulative Distribution Function of Cross Correlation (Tank vs. Terrain Scenes)

This report is an overall review of the main elements of the program. During the program, the philosophy was to give many presentations. This extensive effort is summarized in Section 8. Many of the details of these presentations have been presented as papers during the course of the program and are referred to at appropriate times in the report. Some are included as appendices in those cases where publication might otherwise have been restricted. Much data is cited to illustrate trend of the results.

Section 2 is an extensive description of the actual system used and the matched filter. Our approach to the simulations is also described and representative results presented. The various techniques for recording memory elements are then presented in Section 3. Representative details for a 5x coherently added image matched filter are given. Details of multiplexed carriers are also given in the absence of coverage in other publications.

Storage media experiences are described in Section 4. A detailed description of one such experience comprises Appendix A.

An optical memory capacity formulation is developed in Section 5 based upon the definition of a memory element and the various techniques investigated. The limitations of media resolution upon storage capacity are also given.

In Section 6, an extensive summary of the results are presented and all references given in Section 7. Sections 8 and 9 summarize the professional activities conducted during the program, and the professional people involved respectively.

A number of appendices are included for added description, supportive material, and essential papers. Publications on evolving progress during the program, and others well documented are not included in the appendices.

We conclude this introduction with a bit of what we believe are the key accomplishments of this research program. We emphasize that while each individual item is important in itself, the total program has made a significant step forward in the application of optical correlator technology to problems of target detection, and reconnaissance.

1. Developed techniques for constructing large capacity memories.
2. Developed techniques for utilizing DCG to generate large memories.
3. Demonstrated that multiple holographic lens - matched filter (MHL-MF) arrays can successfully utilize large capacity storage techniques.
4. Applied large capacity memory techniques to DCG and SIL HAL, and found that the technology for photopolymers needs further development. Thus, amplitude and index-of-refraction change phase matched filters were successfully constructed in thin and thick media.
5. Developed a digital simulation of the optical correlator which was validated by both visual and quantitative comparisons with the device output. The simulation allows the optimization of device parameters under controlled conditions and will significantly reduce the development time of various applications of the correlator.
6. Demonstrated matched filter memory techniques with large signal-to-clutter (s/c) ratios using a variety of terrains.
7. Demonstrated through s/c ratio, a compact MHL-MF array optical correlator.
8. Determined the parametric sensitivities of large memory elements, information usable in establishing large memory banks.
9. Developed a formulation for capacity which shows that large ( $\geq 2000$ ) arrays of MF/cm<sup>2</sup> are theoretically possible.
10. Demonstrated that  $\leq$  SMF non-coherently added and 15X MF coherently added memory banks can be made. These are not limits but there are indications that these are close to the upper limits.
11. Demonstrated that two 15X coherent MF memory elements can be carrier multiplexed to yield 30 memory elements in one memory position - a number which is greater than the memory elements needed for 360° coverage of a tank in one range bin.
12. Demonstrated that the validated model can be applied to large coherent addition memory elements and used with a variety of terrains.

## 2 - DESCRIPTION

### 2.1 EXPERIMENTAL SETUP

The experimental test setup for fabricating and evaluating the matched filters is shown in Fig. 2-1. Using an acetate based film version\* of the M-60 tank placed in the rotating film gate, appropriate matched filters are constructed at the matched filter plane. The latter are recorded on plates held in a specially designed MF mount which has X-Y-Z, and  $\phi$ (azimuth) and (rotation) adjustment freedom. Figure 2-2 is a photograph of this device. The output correlation plane was measured using a scanning fiber optic probe ( $50\mu m$ ) and observed at times with a sensitive television camera and monitor. The probe represents 18% of the tank width when projected back to the image plane, a resolution greater than 5 lines per millimeter.

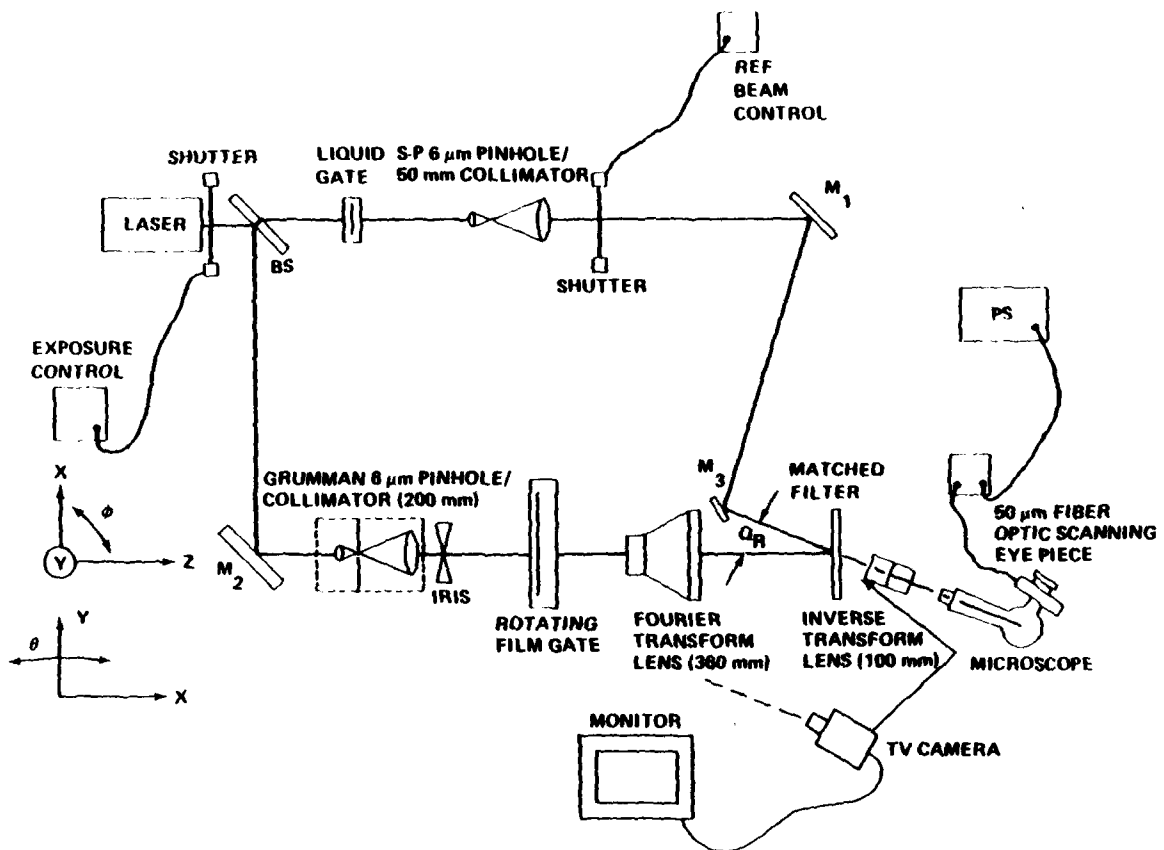
Input imagery was placed in the rotating liquid gate and properly oriented as required. Additional mirrors, like  $M_3$ , were placed along the reference beam line. When multiplexed carriers were investigated, the sequence in recording was usually dictated by minimizing mirror adjustment.

Except for the laser, the arrangement in Fig. 2-1 was maintained throughout the program.

### 2.2 SIMULATION VALIDATION

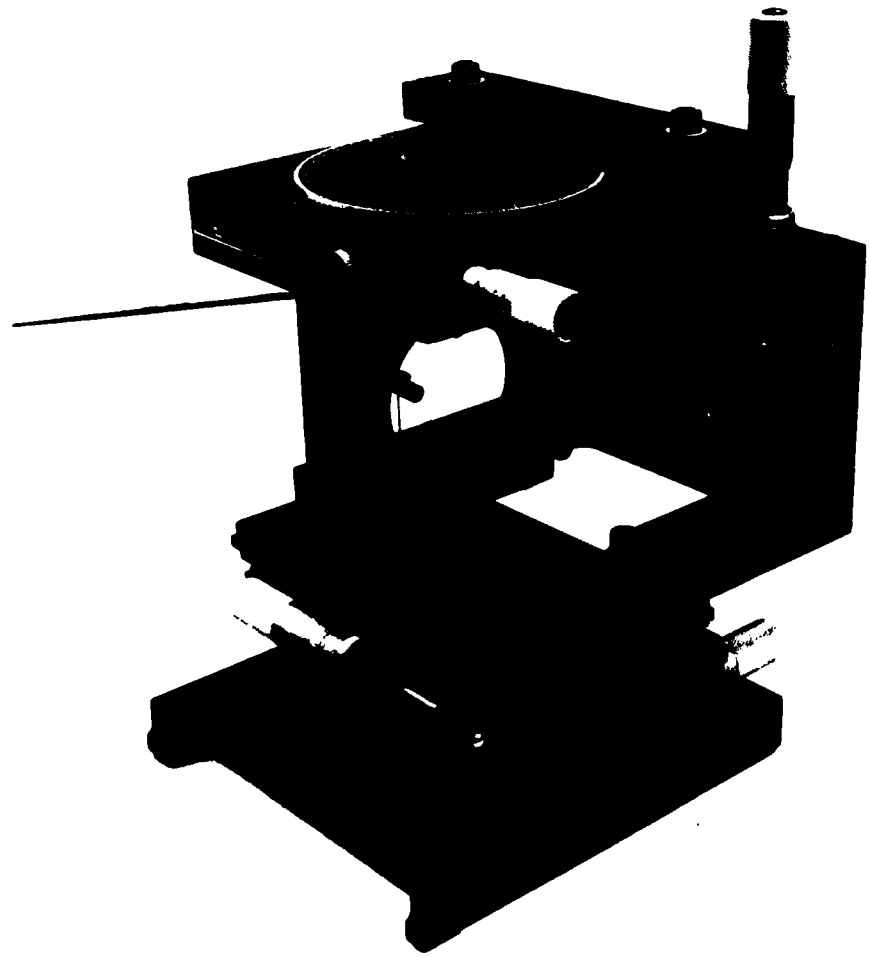
A number of simulations were conducted to augment the empirical aspects of the program. Thus it was necessary to validate the model used for our simulation. The M-60 tank was digitized and the (Fourier transform)<sup>2</sup> obtained in an FFT program. Figures 2-3 and 2-4 illustrate the analog and digital versions of the spectra. Plotting the results along an axis perpendicular to the major tank axis, and comparing them to a scan of an analog version shows a remarkable similarity. These are illustrated in Fig. 2-5 and 2-6. Each of the maxima in the scan

\*Polyester based film is most commonly available and it was necessary to occasionally use it. However, it is more birefringent than acetate based film and some precautions are necessary in MF fabrication. This problem is detailed in the paper contained in Appendix B.



1283-81-005(T)

Fig. 2-1 Arrangement for Matched Filter Fabrication, S/C and Correlation Measurements



1283-81-006(T)

Fig. 2-2 Matched Filter Holder

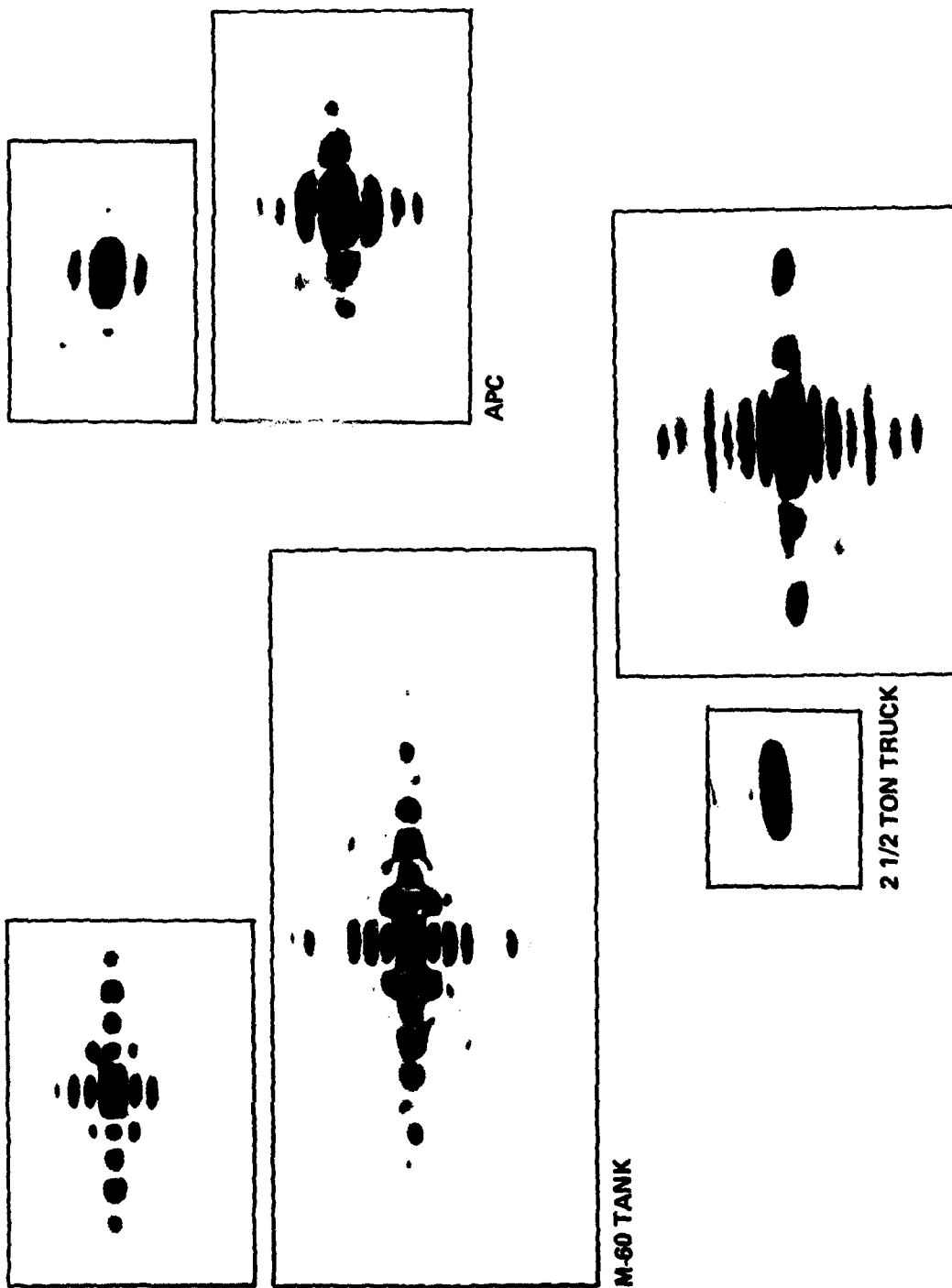
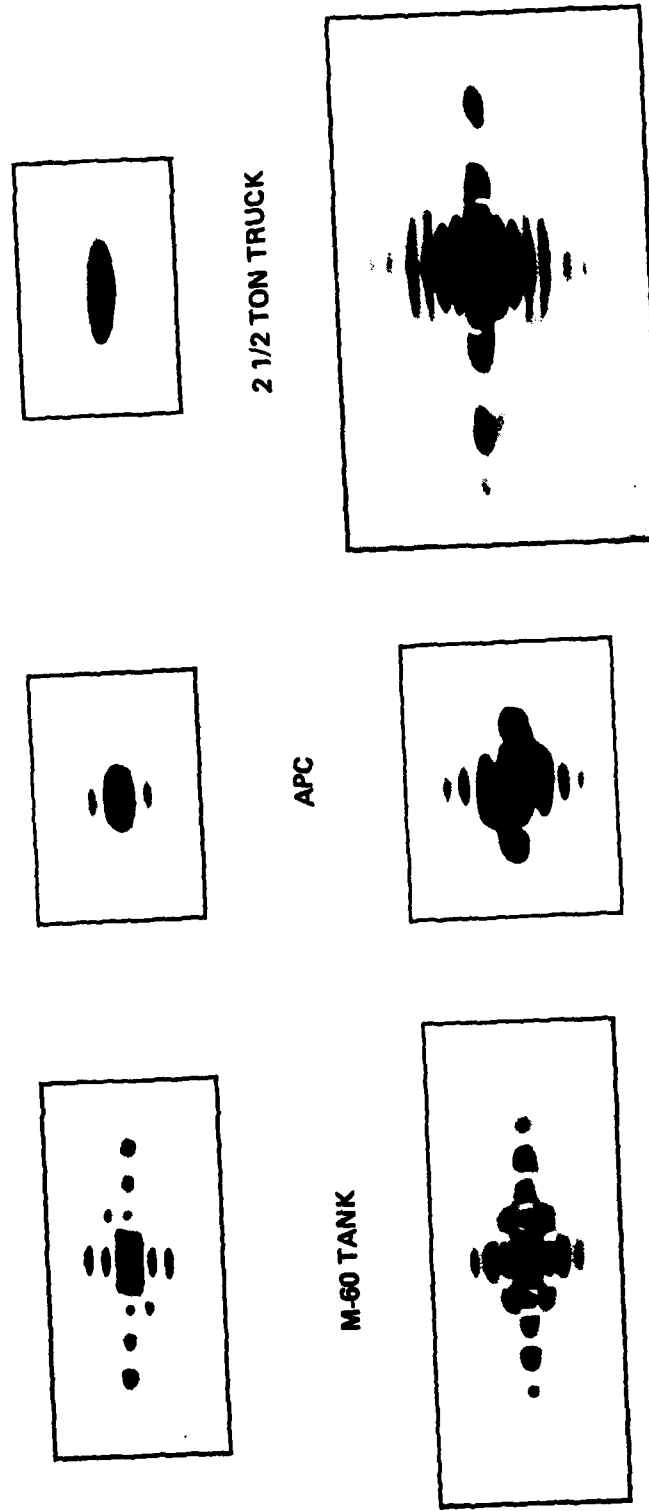


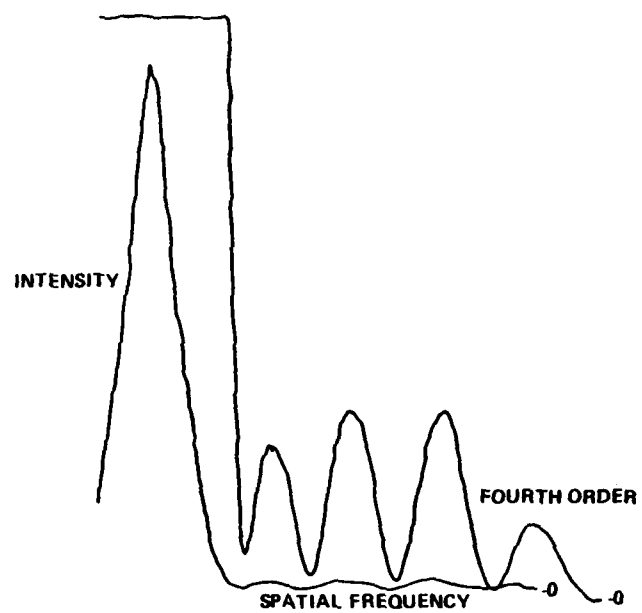
Fig. 2-3 Analog Version of  $(\text{Fourier Transforms})^2$  at 2 Exposures

1283-81-007(T)

Fig. 2-4 Digital Version of (Fourier Transforms)<sup>2</sup> at 2 Thresholds

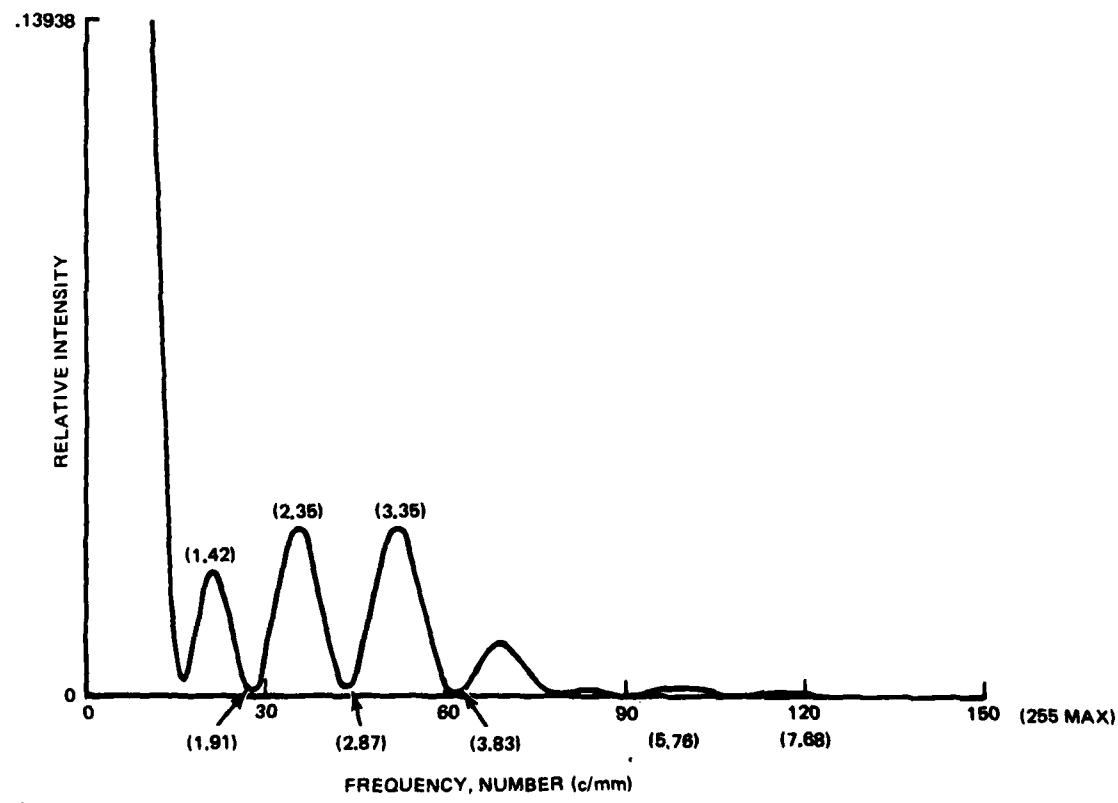
1283-81-008(T)





1283-81-009(T)

Fig. 2-5 M-60 Power Spectrum of Fiber Optic Scan Perpendicular to Major Tank Axis (Ref. 8)



1283-81-010(T)

Fig. 2-6  $(FT)^2$  of Digitized M60 Tank Image

perpendicular to the major axis of the tank is designated an "order". A matched filter optimized for visibility in the center of that spatial frequency band is called a filter of that order in the analog case. For the digital simulation, the cutoff threshold is set at the maximum within that band, and the filter designated as one of that particular order. The validity of our simulations were verified further by determining a signal-to-clutter (S/C) ratio. In this measurement, various terrain scenes are played through various orders of matched filter and the S/C ratio measured. Prior to this, of course, was the need to digitize the terrain. This was done and the  $(FT)^2$  along the major axis of those scenes is shown in Fig. 2-7 to the same scale as the tank spectrum of Fig. 2-4.

Using these terrains<sup>†</sup>, the auto correlation and S/C were measured for various orders of matched filter. The results are shown in Table 2-1 and are quite similar to those obtained on a prior program (Ref 8). Thus, the model used in our simulations was initially considered validated and additional assurance sought.

Use was also made of the simulation in order to determine (a) the auto-correlation variation and (b) the signal-to-clutter (S/C) ratio for the third order filter as the matched filter is cut off at increasing spatial frequencies. The results are shown in Table 2-2.

Through experiments, the physical size of the memory element was established as the restricting spatial frequency filter radius which allowed 95% of the correlation signal to be determined. For the M-60 tank this was found to be 8.25 c/mm, or 2 1/2 times the optimizing spatial frequency. From Table 2-1, it can be seen that the same correlation signal occurs at a slightly lower spatial frequency, suggesting that a smaller MF spatial frequency radius is possible thus leading to a larger memory capacity. Although the simulation-experimental difference is not large, it must be considered that, in the analog case, the recording medium actually provides a low frequency cutoff through film saturation not present in the simulation. Thus, when the overall energy passed by the actual MF is considered, the 95% energy point will be at a higher frequency and the experimental and simulation results will agree.

-----  
<sup>†</sup>In the empirical work, the woodland scene (Fig. 1-3b) was occasionally the only analog common to the simulations. This is one of these occasions.

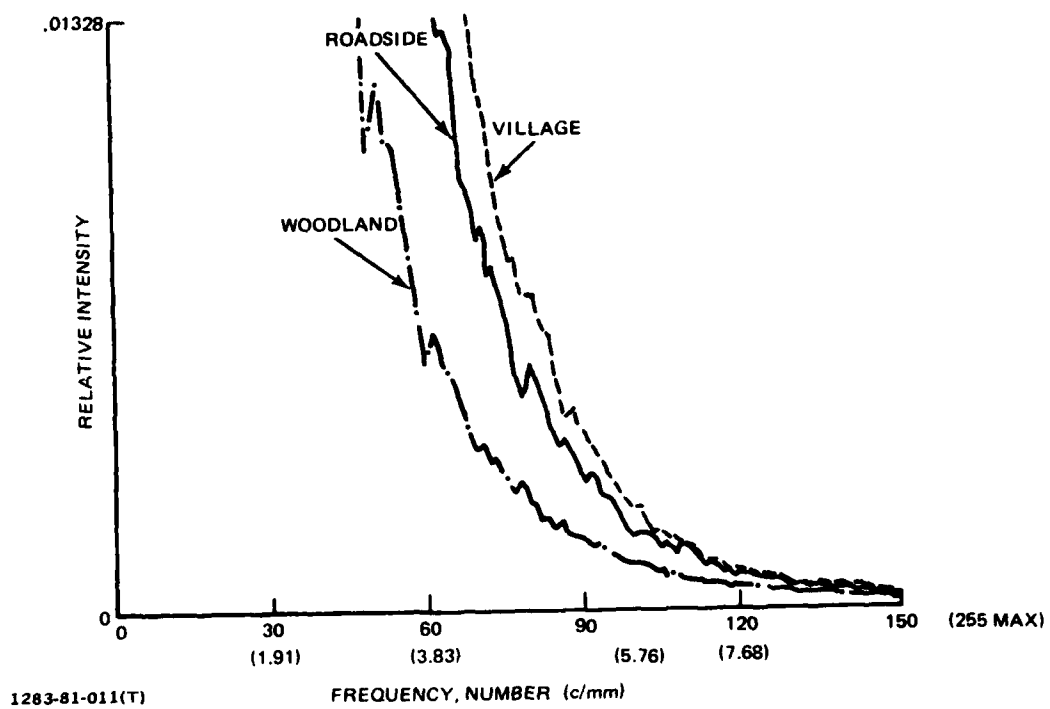


Fig. 2-7 Power Spectrum of Three Digitized Terrain Scenes

MF ORDER	AUTOCORRELATION $\hat{c}_n$	S/C (dB)		
		WOODLAND	ROADSIDE	VILLAGE
0	1.000	- 3.93	- 2.51	- 3.38
1	.182	+ 8.64	+ 5.98	+ 3.58
2	.211	6.48	4.71	3.70
3	.210	6.49	4.66	3.69
4	.100	8.37	4.46	2.48
5	.023	6.83	7.16	3.77
6	.034	8.16	5.88	2.68

1283-015(a)(T)

Table 2-1 Validation of Simulation Through S/C Ratio Measurement

TABLE 2-2 AUTOCORRELATION AND S/C RATIO FOR M-60 IN THREE TERRAINS AS A FUNCTION OF THE SPATIAL FREQUENCY CUTOFF FOR 3RD ORDER MF

SPATIAL FREQUENCY CUTOFF (C/mm)	AUTO- CORRELATION ( $c_N$ )	S/C RATIO		
		WOODLAND (dB)	ROADSIDE (dB)	VILLAGE (dB)
.32	0.000	0.0	0.0	0.0
.96	.143	-5.38	-3.60	-7.86
1.60	.484	+1.10	+2.58	-2.67
2.24	.641	2.70	3.75	-0.02
2.90	.737	3.75	4.66	+1.07
3.54	.881	5.37	5.57	2.52
4.16	.923	5.67	5.83	2.94
4.80	.949	5.94	5.51	3.24
5.44	.975	6.22	5.57	3.46
6.08	.982	6.29	5.52	3.50
6.72	.989	6.39	5.42	3.44
7.36	.993	6.42	5.42	3.62
8.00	.995	6.45	5.40	3.65
16.32	1.000	6.49	5.40	3.69

1283-025(a)(T)

The S/C ratios are seen to closely parallel those previously obtained (Ref 8). In the woodland scene, 95% of the maximum S/C ratio occurs at the same point as the autocorrelation signal, while in the case of the village it occurs at a higher frequency. The roadside is unusual. Ninety-five percent of the maximum S/C ratio occurs just about at the optimizing frequency and then shows a decline to a lower "saturation" value.

The results of this simulation illustrate a valid modeling procedure. A full comparison is made in the last paper presented in this program (Ref 30).

A final check on the validation discussed in that paper is illustrated in Fig. 2-8 and 2-9. In these, the M-60 tank is reimaged through zero, third, and sixth order MF. The similarity in results is once again quite good.

### 2.3 MATCHED FILTER FORMATION AND PLAYBACK

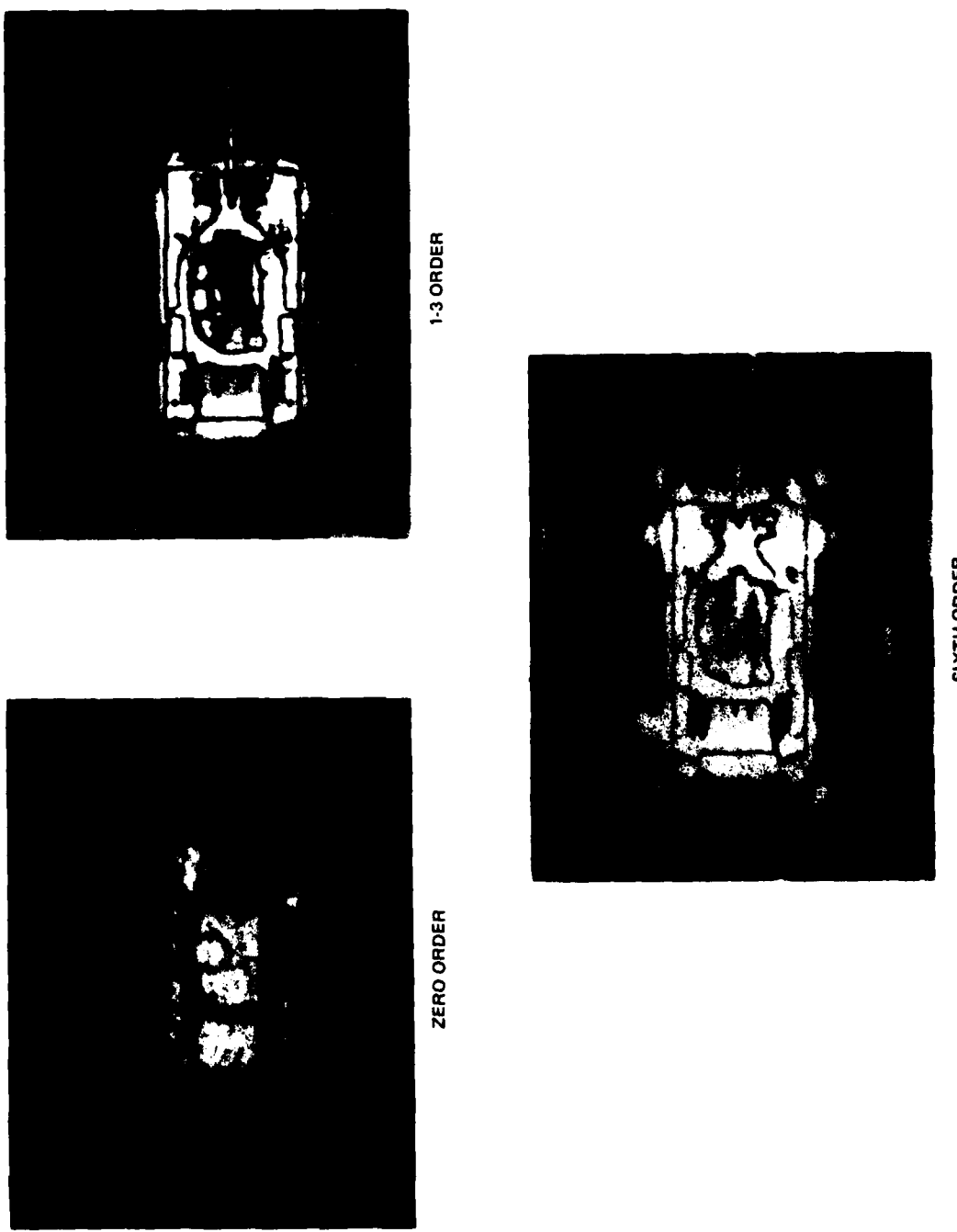
Formation of an M-60 matched filter (MF) using the nonlinear silver halide recording characteristics has been addressed before. See, for example, Ref 9 for the general consideration and Ref 7 for application to the M-60 in particular.

Some insight to the matched filter can be obtained by examining characteristics in the matched filter plane along the axis of symmetry. In the program, the object image is perpendicular to the MF plane. The reference beam is offset but in the MF plane of symmetry which is perpendicular to the MF plane itself. This uniqueness does not, of course, exist in the simulation.

Expressions have been derived for the fringe separation  $d$  of the MF along this axis in the plane of symmetry using the simple geometrical model described above. In the program in all cases the signal beam angle,  $\theta_s$ , was always zero, although comparisons with an equal beam case, i.e.,  $\theta'_s = \theta_R$ , are considered. In those cases we have the condition  $\theta'_s = \theta_R = \theta_s/2$ . The resulting equation is:

$$d\lambda^{-1} = \left[ \sin\theta_R + \sin \left[ \tan^{-1} \left( \frac{\sin\theta_s - V \cos\theta_s + C}{\cos\theta_s + V \sin\theta_s} \right) \right] \right]^{-1} \quad (2-1)$$

with  $F$  being the Fourier transform lens focal length, and  $V = H/F$ , and  $C = \xi/F$  the relative object and spatial frequency locations, respectively.  $H = 0 = \xi$  represents an on-axis object at zero spatial frequency. Figure 2-10 illustrates the results of fringe spacing for the object on-axis case. The results, up to a spatial frequency of  $\pm 15c/mm$ , are most meaningful in terms of the memory element size definition given earlier. It is clear that the matched filter, as constructed,

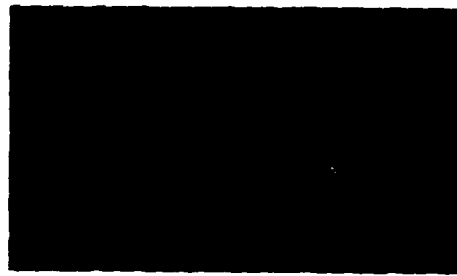


1283-31-012(T)

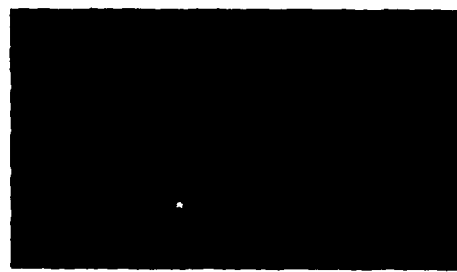
Fig. 2-8 Reimaging of M-80 Matched Filters (Analog)



FIRST ORDER



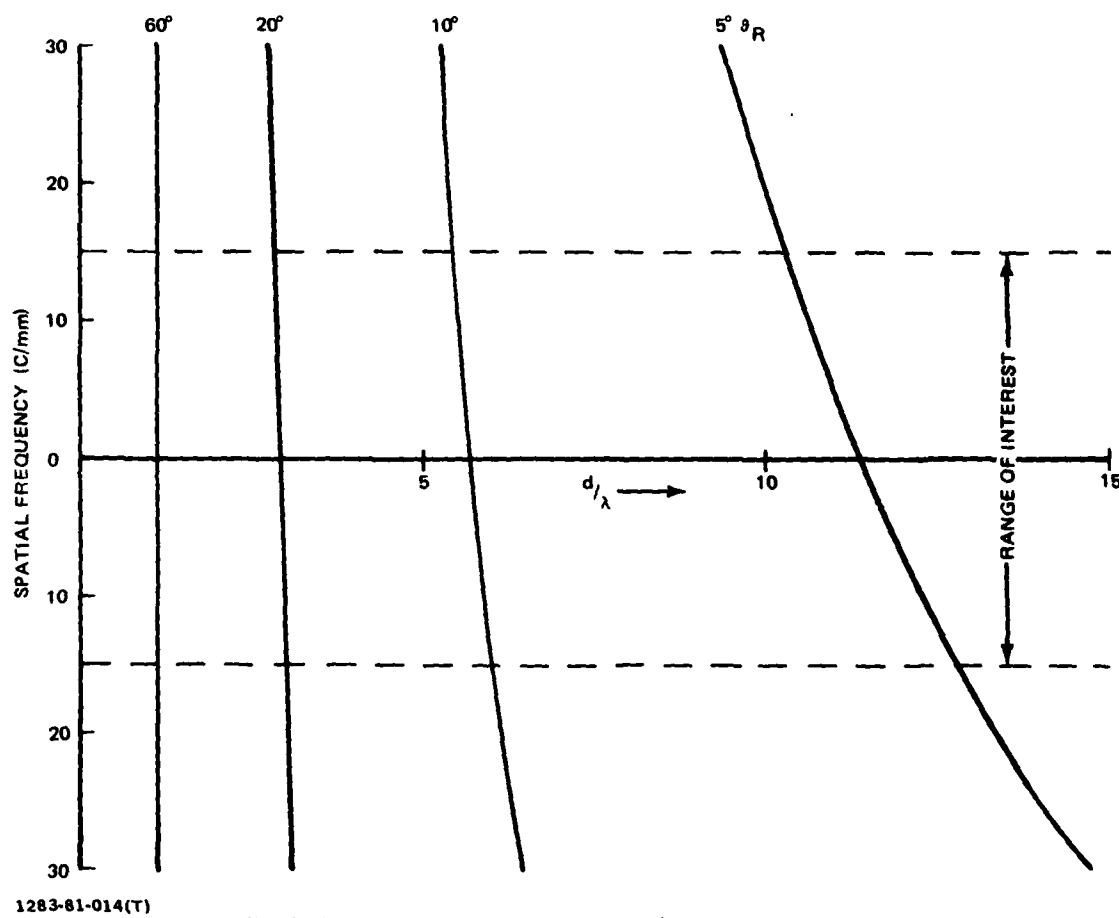
THIRD ORDER



SIXTH ORDER

1283-81-013(T)

Fig. 2-9 Reimaging of M-60 Matched Filters (Digital)



1283-81-014(T)

Fig. 2-10 Normalized Fringe Spacing vs.  $\nu$  ( $\theta_S = 0, V = H/F = 0$ )

is a chirp grating similar to that discussed by Livanos, et al. (Ref 10). When the object position is off-axis, although similar results are obtained, the  $\theta = 0$  cross-over point shifts. These results are more evident in Fig. 2-11. The limits on  $V$  were derived from the assumption of a 35 mm format,  $F = 50$  mm. Looking at the results we find asymmetry. At  $\theta_R = 5^\circ$  and  $\theta_S = 0$ , the ratio  $d/\lambda$  is greater than the corresponding curve for  $\theta_S = \theta_R = 2.5^\circ$  by less than 1%. However, as the reference beam axis angle increases, say to  $60^\circ$ , the variation in  $d/\lambda$  is proportionately larger than the corresponding one for  $\theta_S = \theta_R = 30^\circ$ .

The results of Fig. 2-10 are, of course, independent of the transform lens focal length for the correlator system parameter.  $S = (\lambda F)^{-1}$  accounts for the size but does not alter the spatial frequency characteristics of the pattern.

One extension of Eq (2-1) is the application to multiple holographic lenses in correlators with large memory. In this case the equation still holds except that

$$\theta_S = \tan \left[ \frac{ND \pm \omega}{F} \right] \quad (2-2)$$

where  $N$  is the integral number of offsets of memory position in the corresponding matched filter plane, and  $D$  the MF separation.

The fringe spacing equation holds with this adaptation. Note that the "chirping" becomes different for each matched filter across such an array.

The results of Eq (2-1) can also be used to establish the total number of matched filters between any two reference beam angles for the case in which no two filters have the same carrier frequency. This would be illustrated in Fig. 2-10 if the upper transform spatial frequency limit of one filter would be adjacent to the lower limit for the adjacent filter at some other reference beam angle. For example, if the minimum (physically) realizable reference beam angle were  $5^\circ$ , the adjacent reference beam angle would be the one whose lower transform spatial frequency starts at a normalized carrier frequency of 9.4 ( $v = 30$  c/mm) and decreases. Examination of Fig. 2-10 indicates that at least eight such filters are possible. For a reduced transform bandwidth more are possible, and, in combination with changes in  $R$ , a large array of MF with no common carriers is possible.

On playback, the object may occur anywhere in the input plane including, of course, its position of construction. The former is, in fact, the more probable case.

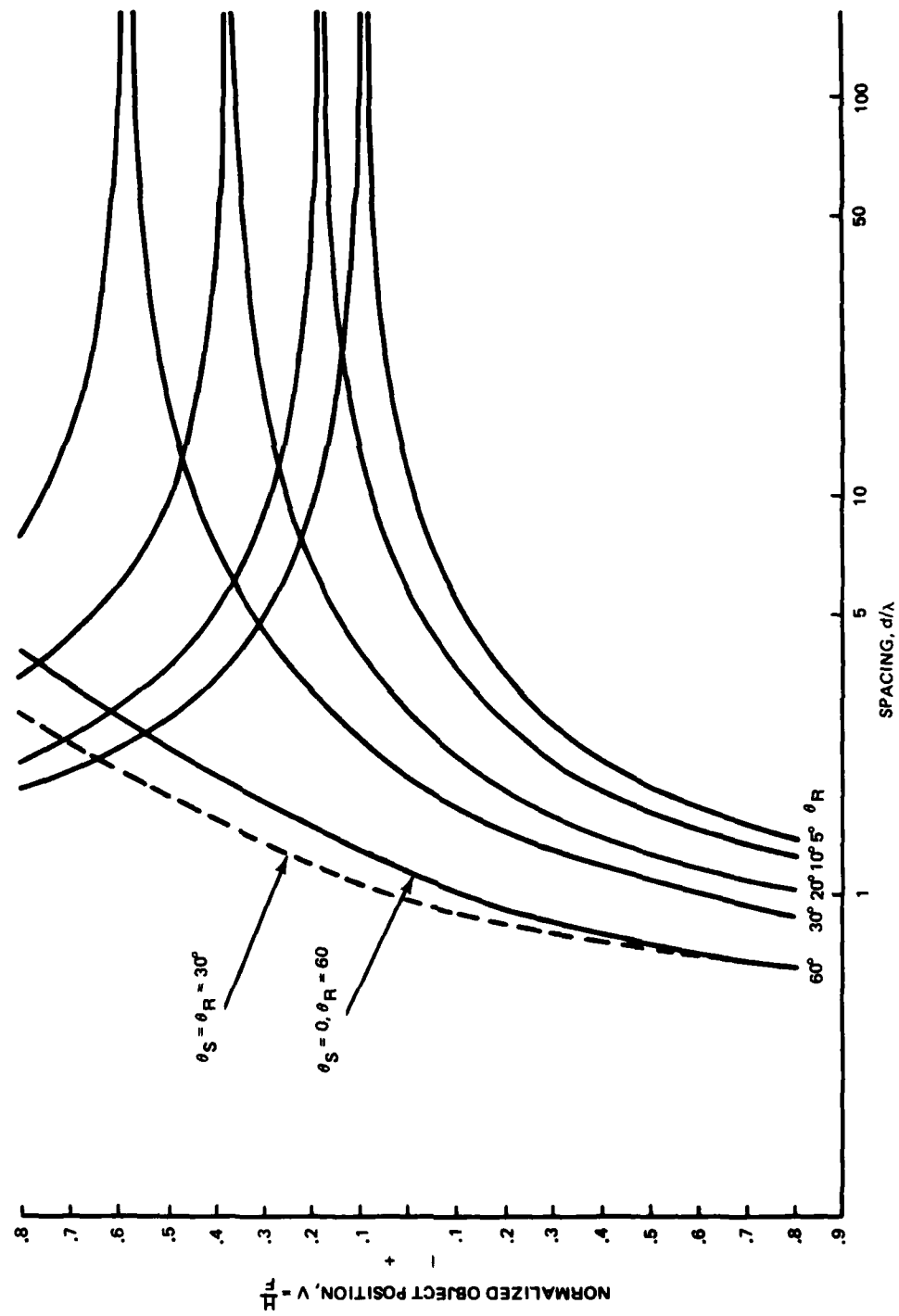


Fig. 2-11 Fringe Spacing at  $\nu = 0$  for Different Object Position During MF Fabrication ( $\theta_S = 0$ )

The MF playback equation is given by

$$\pm \sin R = \sin \theta_R + \sin \left[ \tan^{-1} \left( \frac{\sin \theta_s - V_o \cos \theta_s + c}{\cos \theta_s + V_o \sin \theta_s} \right) \right] \quad (2-3)$$

$$- \sin \left[ \tan^{-1} \left( \frac{\sin \theta_s - V \cos \theta_s + c}{\cos \theta_s + V \sin \theta_s} \right) \right]$$

where  $V_o$  is  $H_o/F$ , the relative object position during MF construction and  $V$ , the relative position during playback. The sign for ( $\sin R$ ) depends upon the relative values for  $H$  and  $\xi$ . Obviously, playback occurs at  $\theta_R$  when construction/playback are the same.

Equation (2-3) can be used to determine the output position of the object in the correlation plane (along the axis defined before) for any position in the object field. When  $H = H_o$ , the last two right-hand terms are not equal. The diffraction angle  $R$  differs from  $\theta_R$ . If we call the difference ( $\theta_R - R$ ) the deviation, i.e.,  $\delta = (\theta_R - R)$ , the input-correlation plane movement is related by:

$$\frac{y}{F_t} = s = \tan \delta = \tan (\theta_R - R) \quad (2-4)$$

where  $F_t$  is the inverse transform lens focal length. If  $F_t$  is equal to the transform lens focal length, we can get a normalized deviation as the limits of a 35 mm film format is traversed (i.e.  $\pm 42$  mm).

Equation (2-4) has been computed for the usual two cases:

$\theta_S = 0$ ,  $\theta_R = \theta$ ;  $\theta_R = \theta/2$ . The deviation increases with increasing total angle but with decreasing input field coverage. Symmetry is best for the smallest angle.

When we consider a holographic lens, MF (square) array in a memory system, the center of any MF is located  $Nd^+$  from the optic axis, where  $N = 0, 1, 2, \dots n$ . Thus,

$$\theta_s = \tan^{-1} \left( \frac{Nd \pm w}{F} \right) \quad (2-5)$$

Using this equation in the previous equations extends them to the one-dimensional "array" of matched filters.

---

<sup>+</sup> Remembering the model covers only the axis in the correlator plane of symmetry

### 3 - TECHNIQUES FOR RECORDING MEMORY ELEMENTS

There are a number of approaches to multiple storage for matched filters which might be considered to increase memory density, with the choice dependent upon the exact correlator configuration, memory requirement, and specific application. The techniques are:

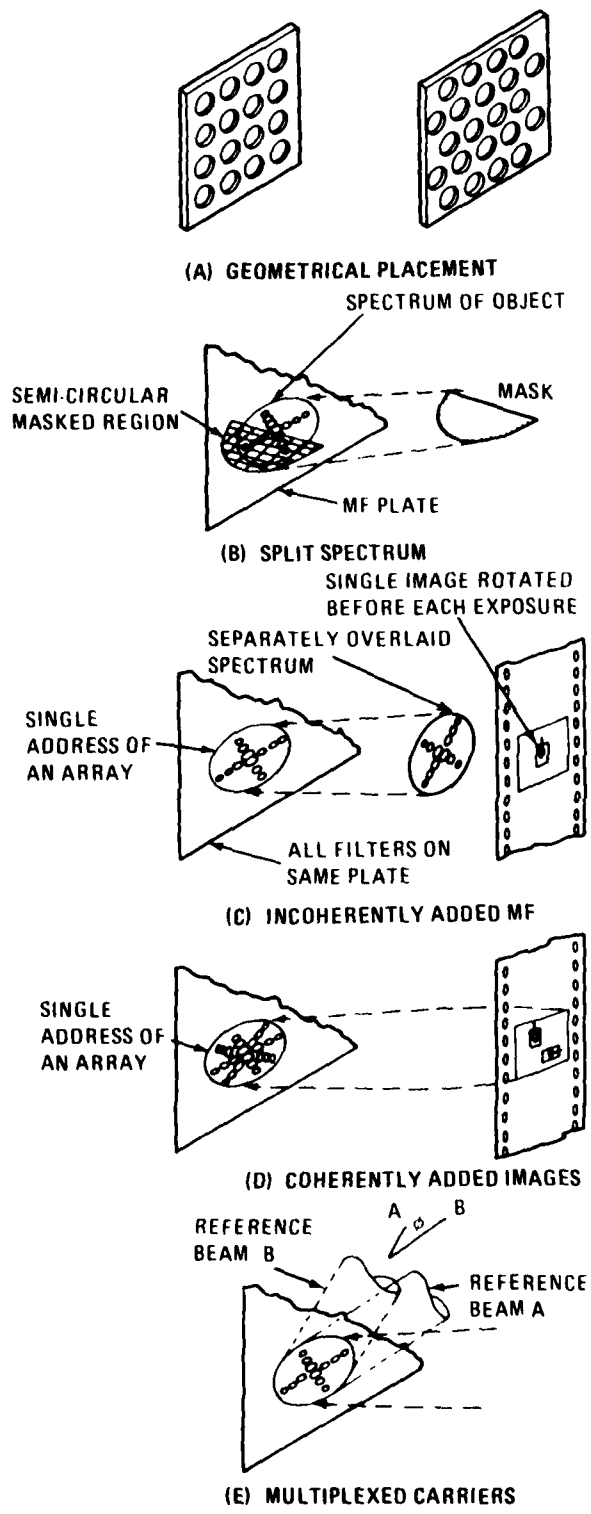
- a. Geometrical configurations
- b. Split Spectrum
- c. Matched filter additions
  - Non-coherent
  - Coherent
- d. Multiplexed carriers

Figure 3-1 illustrates the various techniques.

#### 3.1 GEOMETRICAL CONFIGURATIONS

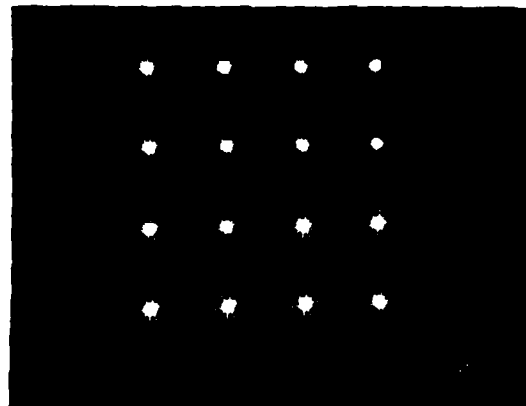
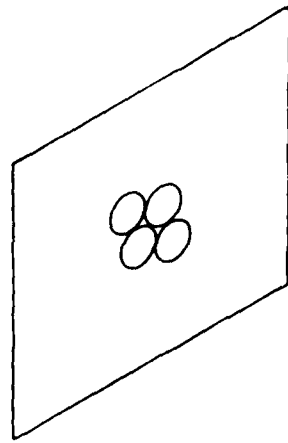
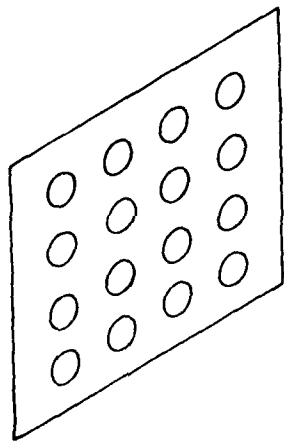
If a memory element is considered to be as defined in Fig. 1.2, then one can establish a regular matrix of elements whose upper frequency cutoff limits are contiguous. When the array is of the same target (and matched filter), the elements can be offset with an increase in the packing density of  $(2/\sqrt{3})$ . Obviously, the combination of several objects whose upper cutoff frequencies differ will lead to a wide variety of packing and require an individual analysis to optimize the efficiency in packing.

Figure 3-2 shows the two packing options, regular and offset, although for the former, they are not contiguous. By way of illustration, a five-coherently-added-image matched filter has been recorded in each of the 16 MF positions (by using a 4x4 multiple holographic lens). Thus, there are basically  $5 \times 16 = 80$  memory positions for the M-60 tank. In the figure they are all the same, when, in fact, each would be modified by an orientation rotation or scale change to provide  $360^\circ$  coverage of the target. Past results have shown that only 23 whole filters are required to cover the M-60 with a  $\pm 19\%$  range bin. Thus, for the memory bank illustrated in Fig. 3-2(a), 3 1/2 range bins could be covered.

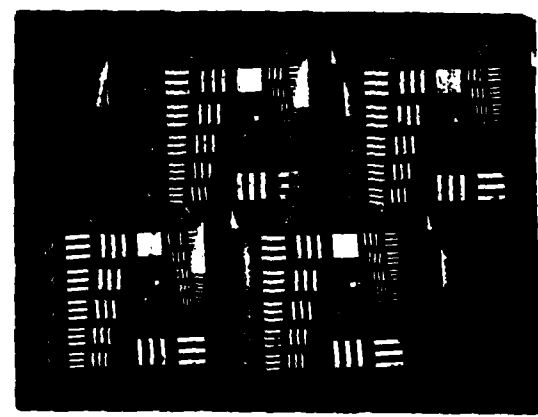


1283-81-016(T)  
70-02-007W

Fig. 3-1 Techniques for Recording Memory Elements



(A) REGULAR ARRAY  
1283-81-017(T)



(B) OFFSET ARRAY

Fig. 3-2 Geometrical Placement of Memory Elements

In Figure 3-2b a reimaging of the AF Tribar target is used to illustrate offset packing. The target was used to evaluate the resolution of several multiple holographic lenses prepared in a new technique.

### 3.2 SPLIT SPECTRUM

From the Fourier transform (FT) equation of any two-dimensional distribution, it can be seen that any axis through  $F(\xi = 0, \eta = 0)$  is an axis of symmetry. One half of the FT hologram or matched filter then, should, in principle, provide sufficient information about the object image to generate autocorrelation signals and acceptable S/C ratios. In practice, as used in the analog system in this investigation, the axis of symmetry is not arbitrary because of the offset, but is uniquely determined by the signal and reference beam vectors. The reason for this uniqueness is the reference beam offset which gives rise to an asymmetric chirp in the matched filter which, in itself, is symmetric above and below the aforementioned plane.

The practical difficulties of implementing a split spectrum experiment far outweighed the anticipated benefits, so resort to our verified simulation was made.

The digital analysis of the split spectrum evaluation was performed by zeroing the redundant portion of the two-dimensional Fourier transform of the tank, the object image. The resulting half-transform was then used to construct the digital MF and various high pass versions of the MF. The woodland scene (Fig. 1-3b), previously digitized, was used to play through the filter.

The results of the split spectrum test show that the autocorrelation signal is halved and the S/C ratio somewhat less than this as shown in Table 3-1.

Clearly, the autocorrelation is as expected, but the cross correlation, and the S/C ratio derived from it, are not. The deviation in the last two are computational artifacts of the simulation attributed to the inclusion of the imaginary terms which do not integrate out when the split spectrum is used.

In a second simulation, four tanks were randomly though squarely placed in the woodland scene. Then the correlation plane was searched and the five largest signals observed as being either a tank or a false alarm. In both the cases, i.e., full and half spectrum matched filters, all four tanks were picked out first. This is summarized in Table 3-2.

TABLE 3-1 SPLIT SPECTRUM SIMULATION RESULTS

	SIMULATION SUPPRESSION LEVEL	NORMALIZED CORRELATION		S/C (dB)
		C <sub>AUTO</sub>	CROSS	
FULL SPECTRUM MF	1.394	1.000	1.571	-3.9
	.026	.182	.068	8.6
	.034	.210	.100	6.5
	.034	.210	.100	6.5
	.010	.100	.038	8.4
	.001	.023	.011	6.7
HALF SPECTRUM MF	1.394	.500	1.110	-6.9
	.026	.091	.037	7.7
	.034	.105	.064	5.7
	.034	.105	.064	5.7
	.010	.050	.021	7.5
	.001	.012	.005	6.8

1283-024(a)(T)

TABLE 3-2 ACCURACY OF CORRELATION LOCATION WITH THE SPLIT-SPECTRUM

	MAXIMUM VALUE	LOCATION		TARGET/ NO TARGET	MISS DISTANCE
		ROW	COL.		
FULL SPECTRUM MF	4.21	44	140	T	1 PIXEL
	4.15	359	111	T	0
	4.00	439	341	T	0
	3.57	139	291	T	0
	1.81	32	187	NT	-
HALF SPECTRUM MF	2.11	(SAME)		T	1 PIXEL
	2.08			T	0
	2.00			T	0
	1.78			T	0
	0.90			NT	-
1283-017(a)(T)					

It can be seen that the half spectrum matched filter (a) provides locational accuracy comparable to the full spectrum MF (with the specified terrain) and (b) enables the four targets to be determined prior to the first false alarm.

As a memory element, the half spectrum performs satisfactorily.

### 3.3 MATCHED FILTER ADDITIONS

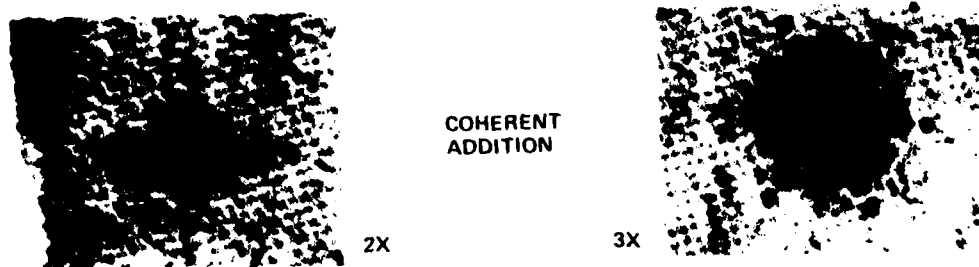
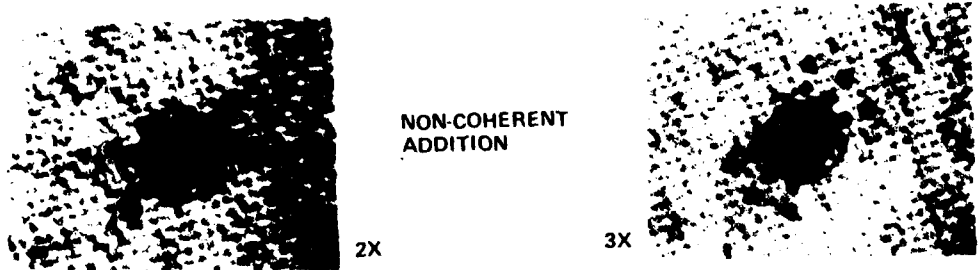
Matched filters can be combined in a noncoherent or coherent manner although one must be careful to distinguish the meaning of the addition. Matched filters can be sequentially overlayed at the same position on the recording medium and we can properly refer to this as the noncoherent addition of matched filters. Alternatively, one can make a single MF as the result of a coherent addition of images in a single exposure. This is referred to as the coherent addition MF, or coherent MF. The distinction between the two should be noted although reference to them will occasionally imply that MFs are coherently added. Figure 3-3 illustrates cases for 2x and 3x coherent and noncoherent addition. In the noncoherent case, rotation of the single tank power spectrum is evident.

Examination of the noncoherent and coherent addition of "n" matched filters can be done using a linear recording response (i.e.,  $T_A = T_O - Et = T_O - \beta It$ ) and obtaining for the amplitude transmittance:

$$T_A = -\beta t [R^2 - T_O / \beta t] - \beta t \sum_{i=1}^n (S_i^2 + R^* S_i + R S_i^*) - \beta t \sum_{\substack{i,j=1 \\ i \neq j}}^n (S_i S_j^*) \quad (3-1)$$

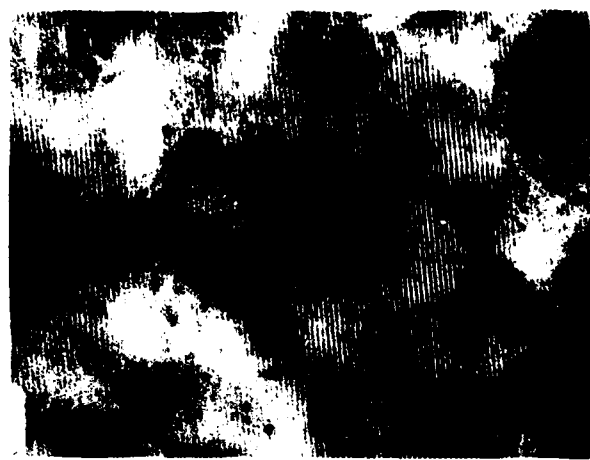
for the coherent case where  $R_1, S_i$  are the reference, signal amplitudes;  $T_O, \beta$  film characteristics; and  $t$  exposure time. The noncoherent result is the same equation without the coupled terms at the right hand side. For simplicity, it was assumed in the latter case  $T_A = T_1 + T_2 + \dots$ . Lang, et al., (Ref 22) developed more extensive relationships for the two cases and an explicit form for the interobject interference terms contained in the coupled term of Eq (3-1). The phenomenon arising from this interference is illustrated in Fig. 3-4. The latter shows the spatial frequency optimization region (called the third lobe or order) for MF of: (a) a single (1x), (b) a four symmetric tank case (4x), and (c) an eight symmetric tank case (8x). The intraobject interference effects can be clearly seen in the last two. Measurement shows the spacing ( $g$ ) dependence is predictable from

$$g = \lambda (\sin \psi)^{-1} \quad (3-2)$$



1283-81-018(T)

Fig. 3-3 Comparison of COH/Non-COH M-60 Tank (Fourier Transform)<sup>2</sup>



(A) 1X



(B) 4X



(C) 8X

1283-81-019(T)

Fig. 3-4 Intralelement Interference in a 4X Tank Image MF

where  $\sin \psi = (h F^{-1}) ((h F^{-1})^2 + 1)^{-1/2} F$ , and  $h$  and  $\lambda$  are the transform lens focal length, image spacing and wavelength, respectively. The carrier interference is clearly visible. Lang, et al., have shown that (image) interference varies according to  $\cos(\alpha_v - \alpha_{v'})$ , where the terms refer to the phases of the objects involved. Thus, when  $(\alpha_v - \alpha_{v'}) = \pi/2$  the deleterious interference effect disappears and the correlation ought to assume its maximum value possible. This occurs at some optimum spacing. As more than two objects are involved, the number of phase terms to be considered rises rapidly.

A question arises as to whether these interobject interferences reduce the autocorrelation or not, and whether or not a random placement, or at least a uniqueness in the geometrical placement, might be advantageous. Matched filters were derived from a set of images consisting of 1x, 4x, and 8x tank placements, and the autocorrelations were obtained with the results shown (Table 3-3).

It seems that the regular placement does not detrimentally impact the autocorrelation. In a second test, an 8x MF was constructed from a 10x image object by using the first eight tanks. In a similar manner, the autocorrelations were measured. The results were (coincidentally) the same, i.e.,  $c_n = .120$ , when compared to a 1x autocorrelation. Both results were obtained with independent tests.

A question also arises as to whether such intersymbol interference arises in the correlation plane since an object is often regularly replicated in an array when there is a multiple holographic lens-MF combination. An experiment was performed in which the center position of a 5 x 5 holographic lens - MF array - was used to obtain an autocorrelation signal. This is shown in Fig. 3-5a. Then, the autocorrelation signal for the center column was obtained as shown in Fig. 3-5b. The spacing between the intraimage interference fringe can be computed from Eq (3-2) by substituting  $h = Nh_0$ ,  $N = 1, 2, 3, 4$ . Finally, when all 25 positions are allowed to transform and the autocorrelation obtained, the signal in Fig. 3-5c results. Clearly this is a worse case situation in which all MF are identical so that, except for spacing effects, interference between all elements is greatest. The situation is similar to a multiple Young experiment.

As with all comparisons, the autocorrelation signal and S/C ratio were measured with the SE Asian scene. The results are summarized in Table 3-4. A scan across the autocorrelation peak of Fig. 3-5c is given in Fig. 3-6. There is a reduction in autocorrelation signal.

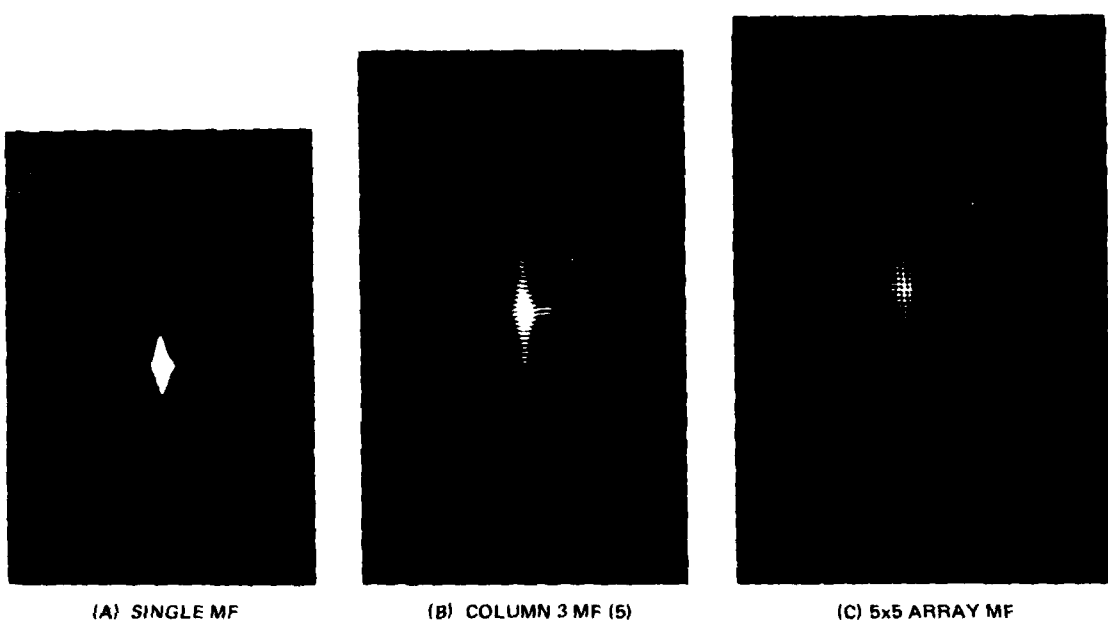
TABLE 3-3 AUTOCORRELATIONS FROM REGULARLY PLACED 1X, 4X AND 8X INPUT OBJECTS

OBJECT SIZE	$\hat{C}_n$ OBTAINED FROM ANGULAR POSITION	NORMALIZED PEAK AUTOCORRELATION $\hat{C}_n$	AVERAGED $\hat{C}_n$
1X	0°	1.000	1.000
4X	0°	.325	.388
	90	.425	
	180	.470	
	270	.333	
8X	0°	.096	.120
	45	.101	
	90	.129	
	135	.135	
	180	.144	
	225	.151	
	270	.118	
	315	.083	

1283-018(a)(T)

TABLE 3-4 EFFECT OF INTERFERENCE ON CORRELATION AND S/C RATIO

MF	AUTOCORRELATION, $c_n$	S/C RATIO (dB)
MF <sub>33</sub>	.60	4.38
COLUMN 3	.65	5.16
ALL 25	1.00	5.00
1283-019(a)(T)		



1283-81-020(T)

Fig. 3-5 Autocorrelations of M-60 Tank from 5x5 Array (All Identical)

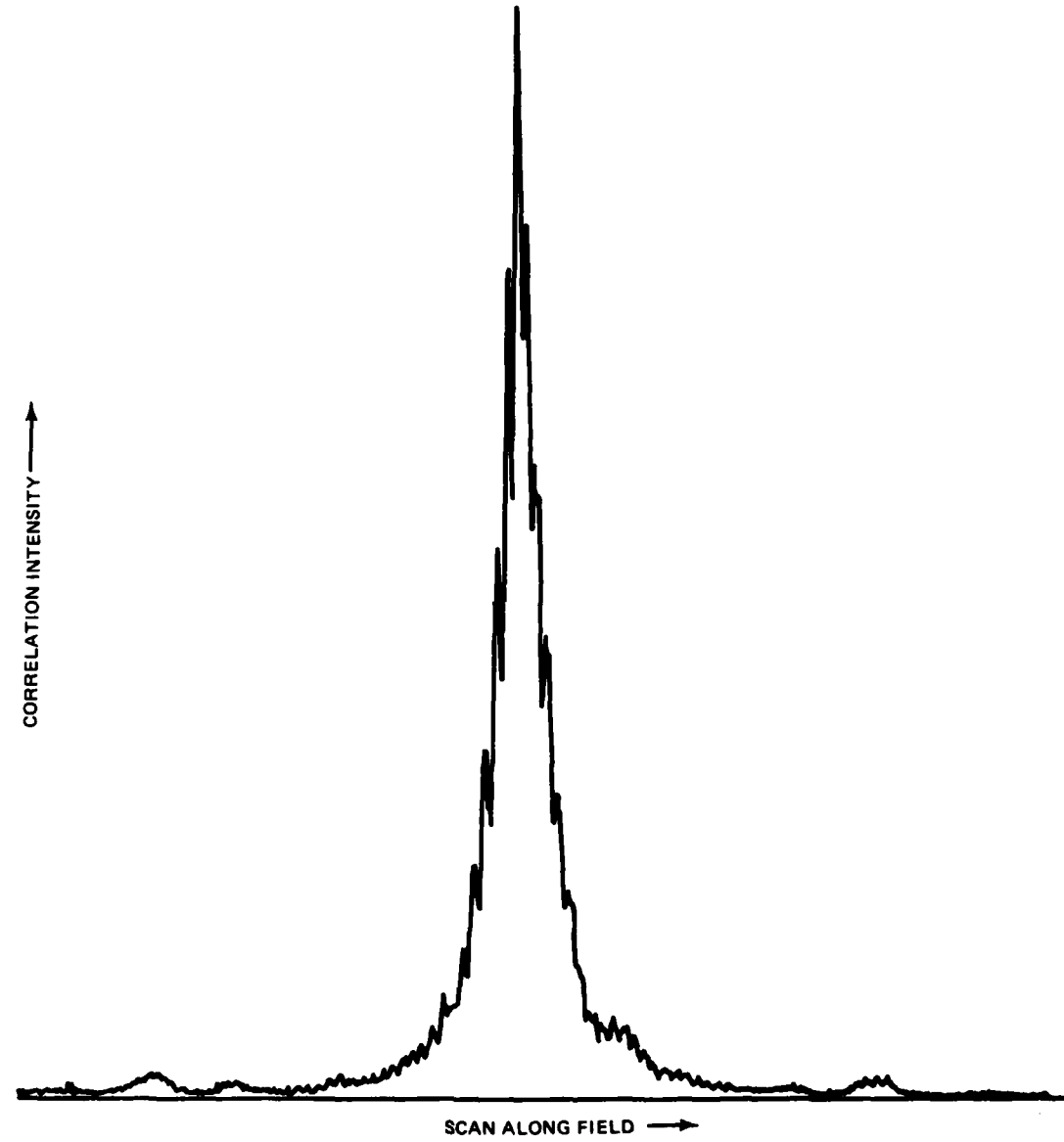


Fig. 3-6 Scan Along Major Tank Axis in Correlation Plane Using 5x5 HL Transform Lens

1283-81-021(T)

### 3.3.1 Noncoherent Addition

Noncoherent addition is a literal overlap or addition of matched filters within the limits of a memory element defined earlier. The MF were optimized in terms of fringe visibility at the desired spatial frequency through the  $R = (\text{Reference Beam}/\text{Signal Beam})$  ratio, and the equal exposure requirements of the amplitude transmittance-exposure ( $\tau_A - E$ ) relationship for silver halide, or efficiency-exposure ( $\eta - E$ ) for dichromated gelatin. Figure 3-7 illustrates a few basic configurations of noncoherent addition including the use of orthogonal carrier beams (see Ref 11). This variant is not covered here but does influence the overall memory capacity. Figure 3-7 shows the cases where (a) the image is rotated, (b) the MF are overlapped at the same carrier frequency, and (c) the case where the MF recording medium is rotated. Only the first scheme (a) was used in this program. The overlapped MF (b,e) are, of course, redundant except when the carrier frequency is different, and this is treated later. In the last case, we are aware of only Almeida (Ref 12) using rotated MF planes. It must be realized, of course, that playback for the c,f techniques generates independent correlation planes.

An interesting variation of noncoherent addition occurs when a coherent array of objects (tanks) is used individually to make a noncoherent array. This is discussed below.

A series of filters was made up to 5x and their effectiveness, as measured by the S/C ratio, determined. In addition, the rotation sensitivity was also determined to ensure an experimental similarity in bandpass characteristics. These filters were constructed in dichromated gelatin. The results are summarized in Table 3-5. Pictures of the 2x and 5x cases in dichromated gelatin are shown in Fig. 3-8, while the impulse response of the latter case is shown in Fig. 3-9a. Clearly, rotation of the image was done with an osculating center. Using the 5x matched filter, the SE Asian scene was played through and the S/C measured to be 8.87 dB. The results of a scan across the tank in this evaluation is shown in Fig. 3-10.

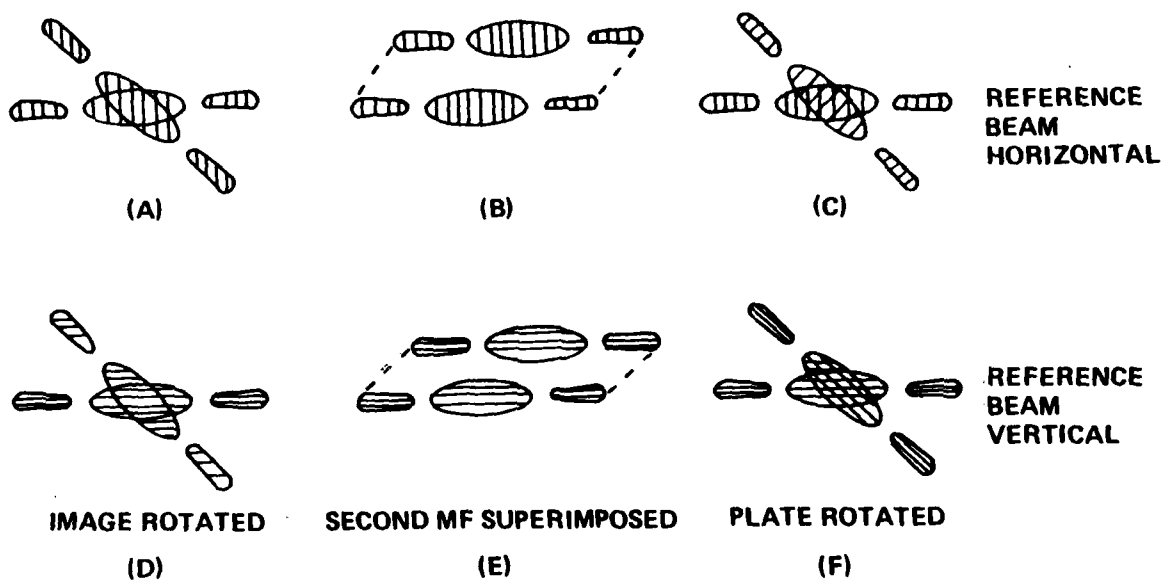
### 3.3.2 Coherent Addition

Coherent addition entails the preparation of an object transparency which consists of an array of targets, or some target with an array of views or orientations. Then, a single matched filter is made of the array. As seen from Eq 3-1, the MF is more complex than the addition of several individual matched filters.

TABLE 3-5 PERFORMANCE OF NONCOHERENTLY ADDED MF IN DICHROMATED GELATIN

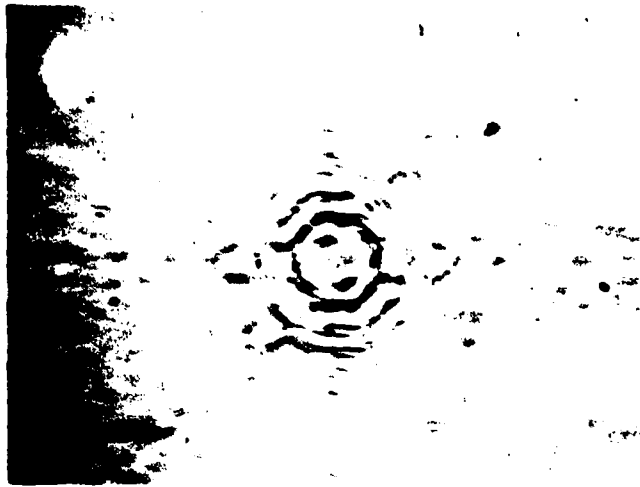
# OF MATCHED FILTERS AT POSITION	THICK			THIN		
	S/C db	C <sub>n</sub> AVE.	Δθ DEGREES	S/C db	C <sub>n</sub> AVE.	Δθ DEGREES
1	6.87	1.00	± 6.75	5.00	1.00	± 7.6
2	8.46	.482	± 6.99	5.60	.33	± 6.6
3	5.67	.678	± 6.70	5.40	.97	± 6.5
4	8.81	.449	± 6.47	6.80	.72	± 6.6
5	6.29	.968	± 5.35	—	—	—

1283-020(a)(T)



1283-81-022(T)

Fig. 3-7 Non-Coherent Addition at Constant Carrier Frequency



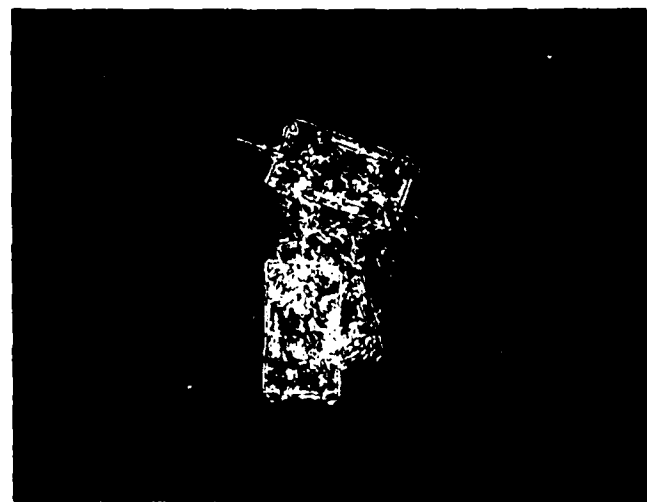
(A) 2 MF



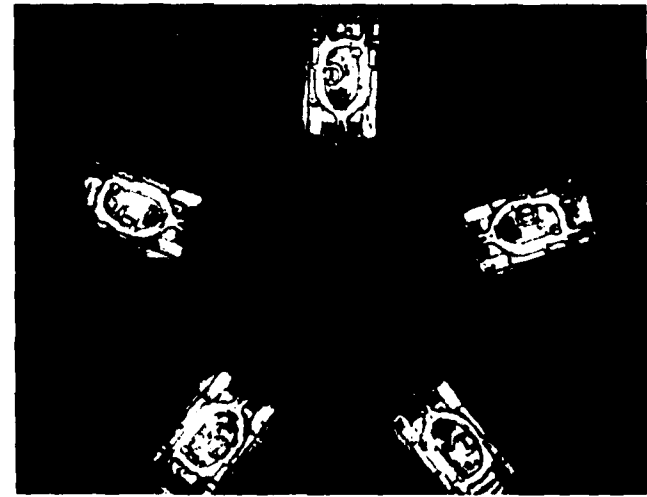
(B) 5 MF

1283-81-023(T)

Fig. 3-8 Non-coherently Added MF in Dichromated Gelatin



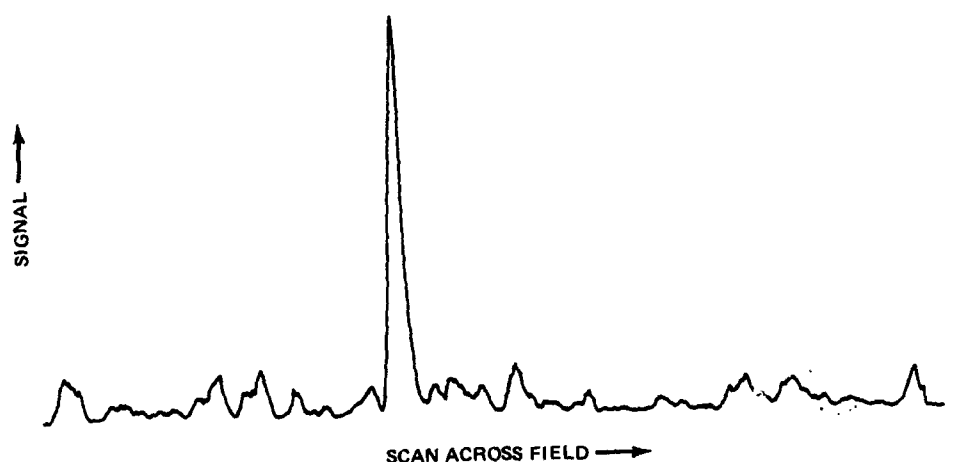
(A) NON-COHERENT



(B) COHERENT

1283-81-024(T)

**Fig. 3-9 Impulse Response of 5x Image Matched Filters in Dichromated Gelatin**



1283-81-025(T)

Fig. 3-10 Scan Across Correlation Plane Using 5x Non-COH Matched Filter (Dichromated Gelatin)

Consider that the targets are arrayed as in Fig. 3-11 with either (a) a regular or (b) random array. Let  $E(x, y)$  be the transmittance of a single target. Then, the effect of rotation and translation on i-targets yields the Fourier transform (Appendix D) of the array:

$$F(2\pi\nu_x, 2\pi\nu_y) = \sum_{i=0}^N e^{-j(\omega_x x_i + \omega_y y_i)} \left[ \iint_{-\infty}^{\infty} E(x', y') e^{-jx'(\omega_x \cos \theta_i + \omega_y \sin \theta_i)} e^{-jy'(-\omega_x \cos \theta_i + \omega_y \sin \theta_i)} \right] \quad (3-3)$$

where the  $x'$ ,  $y'$  are the target coordinates, and the  $\theta_i$  the corresponding angles for i-th target:

$$\begin{aligned} x' &= (x - x_i) \cos \theta_i + (y - y_i) \sin \theta_i \\ y' &= -(x - x_i) \sin \theta_i + (y - y_i) \cos \theta_i \end{aligned} \quad (3-4)$$

The complexity of the spectra of the coherent arrays suggests that some organized method of optimization was needed other than trying to maximize fringe visibility at a particular spatial frequency. While the latter technique works well for the well defined single target case, it does not appear applicable to the multiple case. Rather, the situation was handled by using the 1x target for optimization and then making appropriate adjustments in the beam ratio R for targets of increasing complexity. This proved effective for silver halide and dichromated gelatin and was consistent with the work of Mehta (Ref 13) which called for a modified fringe visibility

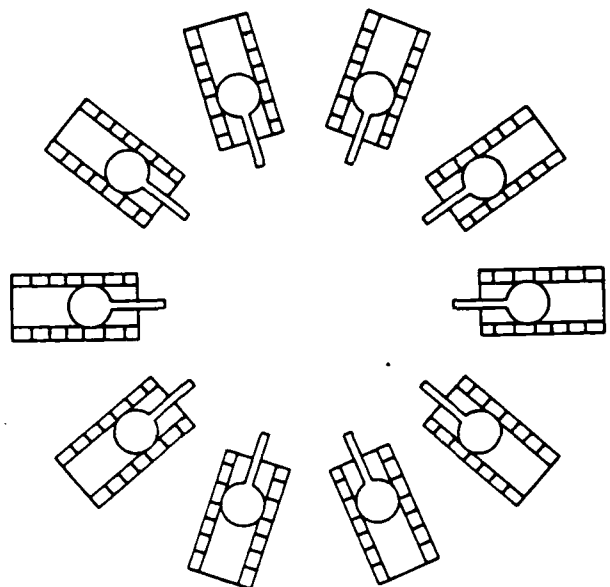
$$V = \frac{2R^{\frac{1}{2}}N}{R + N^2} \quad (3-5)$$

where N is the number of images used.

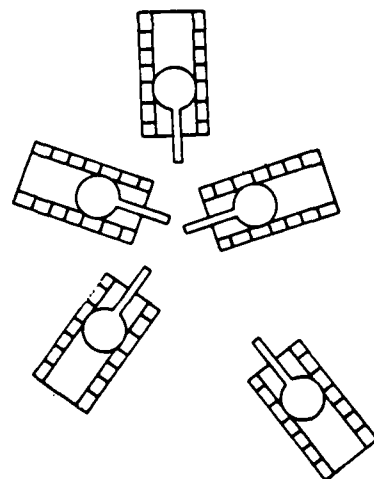
Images from 1x to 10x, in addition to 15x, were laid out and photographed, and the negative used in the subsequent tests. Individual autocorrelations were determined for the 1x-10x set and are shown in Table 3-6. The table brings out a limitation in using analog methods in the preparation of the imagery. Despite the exercise of care, unequal images still result. While the N-averages show a general decline, and while a few of the multiple images show a fair degree of equality, a number are better than 2:1 in high/low ratio.

TABLE 3-6 POSITIONAL DISTRIBUTION OF AUTOCORRELATIONS OF COHERENT MATCHED FILTERS USING THIN SILVER HALIDE

CORRELATION OF COHERENT IMAGERY										
	1X	2X	3X	4X	5X	6X	7X	8X	9X	10X
	1.000	.492	.269	.266	.340	.103	.058	.054	.043	.038
		.442	.222	.160	.270	.015	.043	.047	.029	.024
			.213	.167	.276	.083	.046	.045	.030	.017
				.254	.298	.074	.039	.027	.022	.024
					.271	.071	.049	.032	.025	.023
						.071	.044	.021	.025	.020
							.049	.032	.025	.024
								.047	.030	.035
									.014	.021
										.027
N-AVERAGE	1.000	.467	.235	.212	.291	.070	.048	.038	.028	.025
HIGH/LOW RATIO	1.000	1.113	1.263	1.663	1.259	6.867	1.487	2.571	3.071	2.235
1283-021(a)(T)										



TEN M-60 TANK IMAGE



FIVE M-60 TANK RANDOM ARRAY IMAGE

1283-81-026(T)

Fig. 3-11 Image Arrays

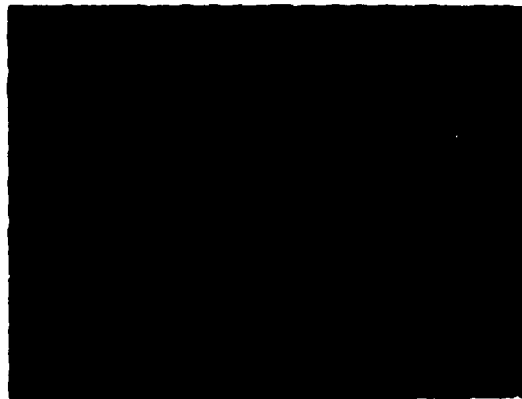
Throughout the program, specific test objectives were met by sets made specifically for it with subsequent differences in correlation values. This procedure was used to isolate a test and account for differences in emulsion batch, environmental factors, and sometimes personnel. The 5X was selected as representative of the group as being the largest size with the most uniformity, and thus, subject to a more comprehensive set of evaluations. The set is often compared to correlation results from a 5X noncoherent addition set.

### 3.3.3 5X COH and Non-COH Comparisons

The coherent and noncoherent 5X matched filter performances were compared on the basis of individual autocorrelation signals, S/C ratio, and angular and translational sensitivity. After the input imagery was set at the proper angle and masked, the autocorrelation signals for each of the five positions was determined. At any one time, some degree of response was obtained at the other four non-aligned positions, although at significantly reduced levels. The views of the correlation plane at two threshold levels are shown in Fig. 3-12, 3-13 for both techniques at comparable 16:1 exposure levels. The same, but otherwise arbitrary, angle was chosen in each case. The numerical results are shown in Table 3-7 for the two silver halide emulsions. Figure 3-14 shows the full 5X MF autocorrelation under the same conditions as those of Fig. 3-12 and 3-13. The element placements should be noted. The impulse response of the 5X COH array was previously shown in Fig. 3-9.

Each of the filters was tested against the SE Asian scene with 5 vehicles, and the S/C ratio determined by scanning through the autocorrelation signal. The clutter obtained is that from the same scan line. These results gave S/C ratios somewhat larger than might be obtained if the whole field were searched for the peak clutter. However, for direct comparisons the "standard" scans were employed. Other tests have shown that an all-plane scan would yield somewhat lower ratios for this terrain scene but not always because of the same terrain feature for the different MF. The results of these scans for each matched filter, and for each of the 72° spaced images, are given in Table 3-8. It can be seen that the S/C ratio for 5X COH and Non-COH matched filters all show better than 4:1 ratio, while the thick MF is about 1.5 dB lower than the thin MF.

Figure 3-15 illustrates the correlation plane for the 5X Non-COH matched filter when the SE Asian scene with 5 vehicles is used. The threshold ratio



(a) AUTOCORRELATION, C



(b) C AT REDUCED THRESHOLD

Fig. 3-12 Autocorrelation of Single M-60 Tank Playing Through 5X Non-Coherent Matched Filter

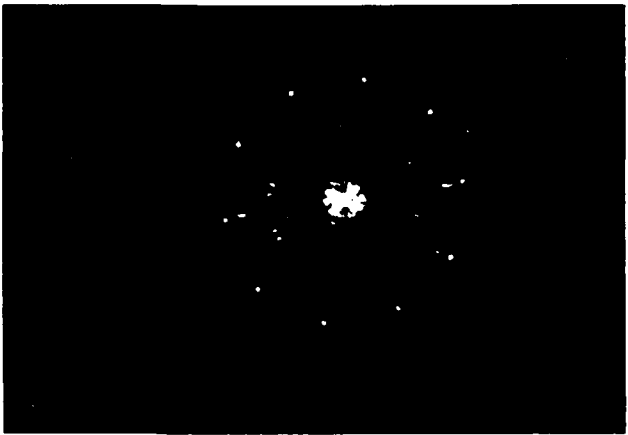


(a) CORRELATION, C

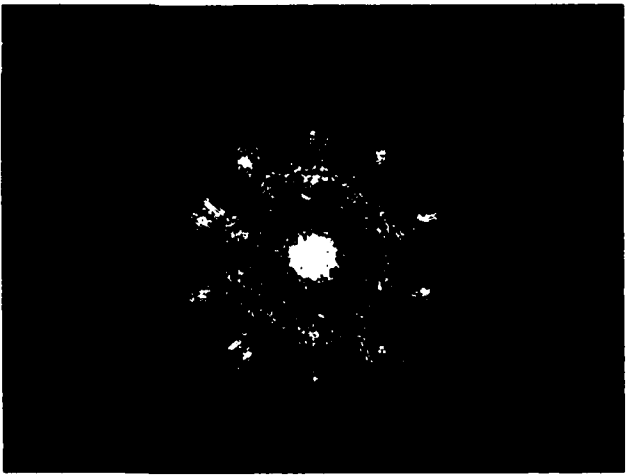


(b) C AT REDUCED THRESHOLD  
1283-81-028(T)

**Fig. 3-13 Autocorrelation of a Single M-60 Tank Playing Through 5X Coherent Matched Filter**



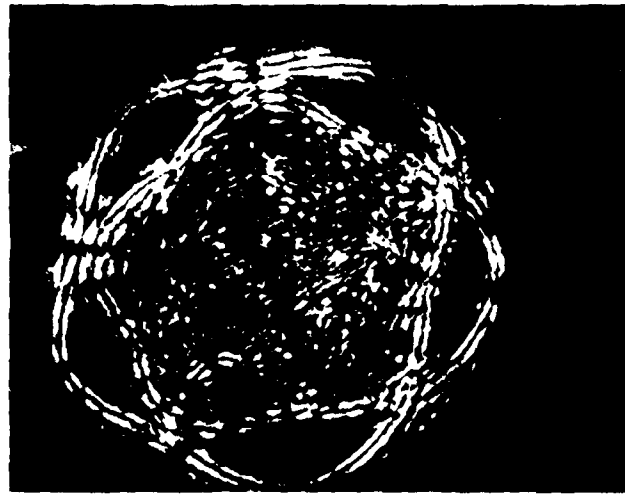
(a) NON-COHERENT ADDITION



(b) COHERENT ADDITION

1283-81-029(T)

**Fig. 3-14 Autocorrelation Planes When Entire 5x Image Plays Through Non-Coherently  
and Coherently Made Matched Filters**



(a) CORRELATION PLANE FOR TERRAIN IMAGE PLAYING  
THROUGH 5X NON-COHERENTLY ADDED MF



(b) AT REDUCTION TO 20% EXPOSURE  
1283-81-030(T)

**Fig. 3-15 Correlation Plane of a 5x Non-Coherently Added Matched Filter  
Using SE Asian Terrain Image Input Upon Playback**

TABLE 3-7 5X COH AND NON-COH MF PERFORMANCE

IMAGE (°)	$\hat{c}_n$ CORRELATION		
	NON-COHERENT	COHERENT	
		THIN	THICK
- 144	0.790	0.793	0.731
- 72	0.816	1.000	1.000
12 O'CLOCK	0.803	0.998	0.809
+ 72	0.943	0.915	0.657
+144	1.000	0.825	0.540

1283-022(a)(T)

TABLE 3-8 S/C RATIO FOR COH AND NON-COH 5X MATCHED FILTERS

IMAGE (DEG)	S/C RATIO (dB)		
	NONCOHERENT		COHERENT
	THIN	THIN	THICK
- 144	8.76	9.42	4.56
- 72	5.26	8.51	8.51
12 O'CLOCK	8.87	8.82	5.28
+ 72	6.86	6.88	5.71
+144	7.57	6.30	6.86
AVERAGE 1283-023(a)(T)	7.45	7.99	6.16

between the two figures is 5/1. Further reductions reveal the solitary prominence of the autocorrelation signal. The pentagonal nature arises from the aperture defining the input field, although full illumination of the 35 mm format leaves the S/C ratio unaltered. Tests with the M-60 near the aperture yield comparable S/C results and only when the tank becomes obscured does the autocorrelation signal decrease.

The translational sensitivity of the autocorrelation signal was determined for the 5x MF and compared to that previously done (Ref 7) for a single tank filter (1x). Single images were played through the three complex matched filters and the matched filters translated in the MF plane. In each case, the filters were tuned for autocorrelation peaks at the outset of each test.

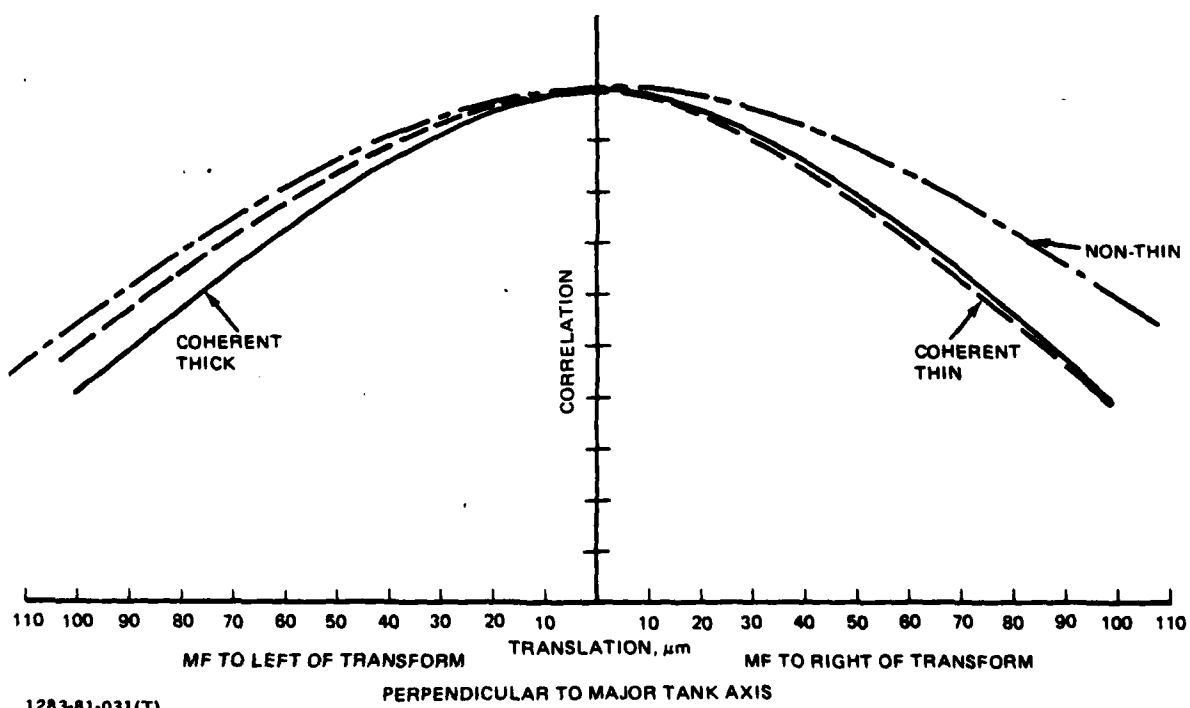
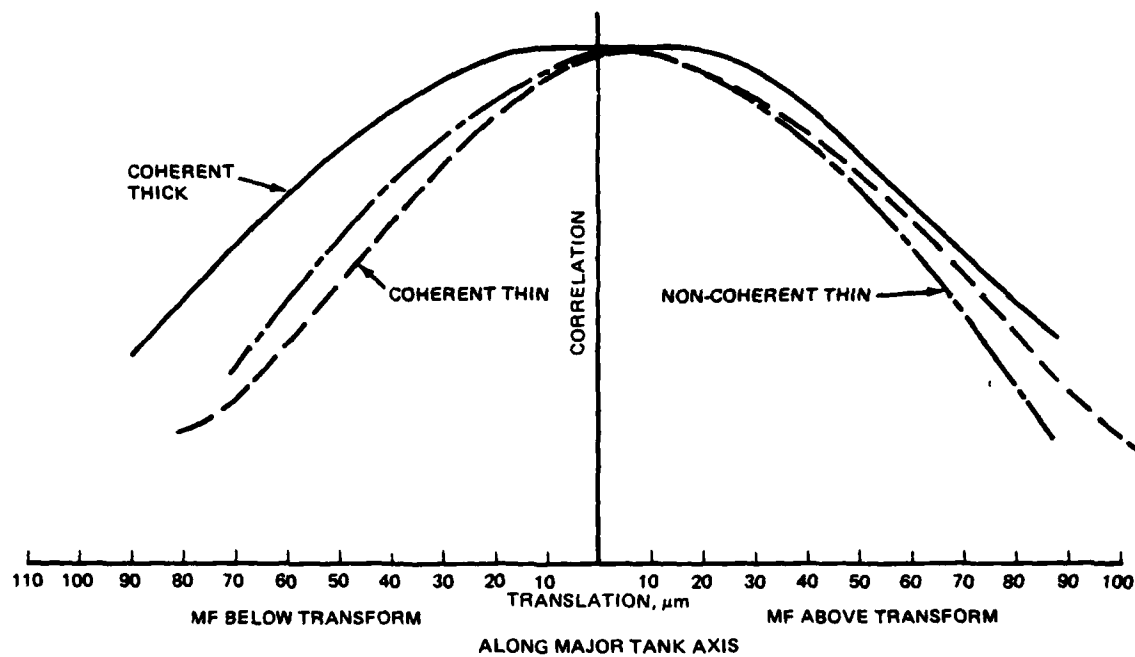
Figure 3-16 shows the autocorrelation signals as a function of translational movement parallel and perpendicular to the major tank axis, respectively.

To a close approximation, a single (1 x 2) mm tank image has a Fourier transform whose zeros are at the zeros of  $F_y = \text{Sin } y/y$  and  $F_x = \text{Sin } x/x$  for the parallel and perpendicular directions respectively. Putting the wavelength, focal length, and image dimensions in expanded forms of these equations yields zero intervals of 114 and 228  $\mu\text{m}$ , respectively. Based upon a simple overlap model, it can be seen that axial translations of 57 and 117  $\mu\text{m}$  should yield 50% frequency domain overlaps, and thus perhaps a -3 dB change in correlation. From the data, we can conclude that multiple image matched filters differ little from the 1x MF in translation sensitivity (Ref 7), or from a simple rectangle model. The orthogonal translations are not the same, but conform to the results of the rectangular model. This is conclusively seen in the results for the 10x coherently added image MF which, in a single test, was directly compared with a 1x MF (Fig. 3-17, 3-18).

Past experience has shown the axial movement determination unnecessary. Consider the depth of focus equation

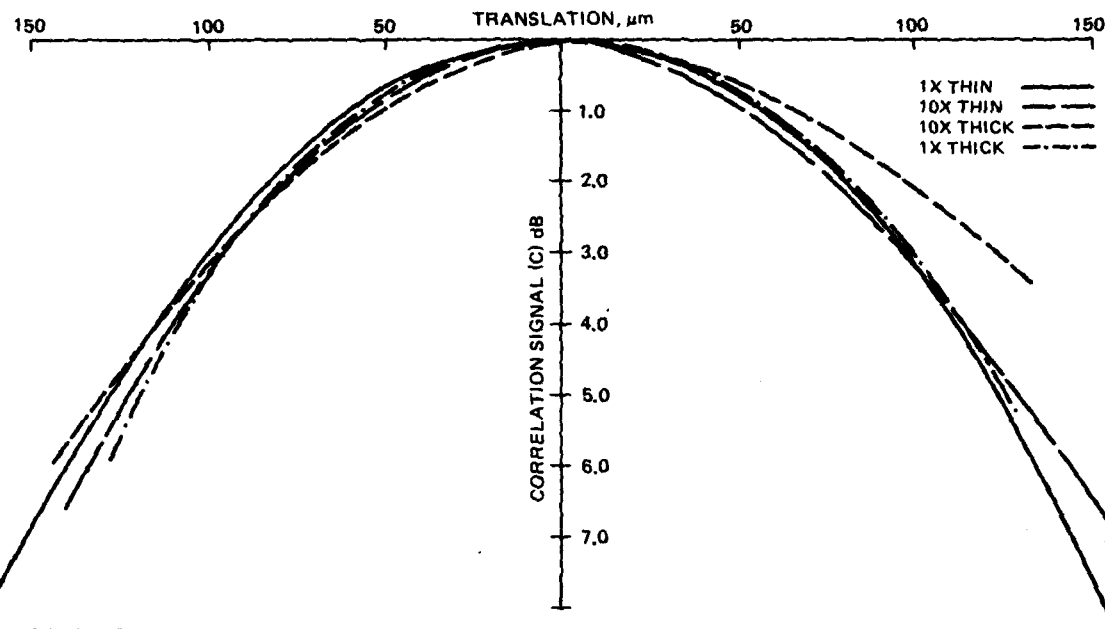
$$\Delta = \frac{2\phi}{1 + \phi} (\rho^2 - 1)^{\frac{1}{2}} \quad (3-6)$$

where  $\phi = F(\pi^{-1}r_0^{-2})$  with  $r_0$  being the input beam radius. For the parameters of our system, and allowing a 10% variation in "focal spot size" (i.e.,  $\rho = 1.10$ ), the depth of focus becomes 9.54 mm, yielding little impact upon the autocorrelation.



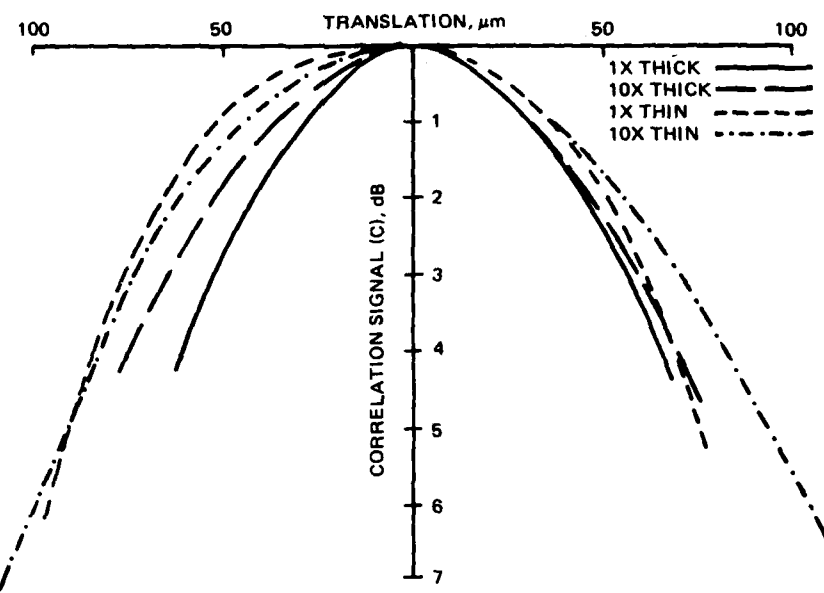
1283-81-031(T)

**Fig. 3-16 5X MF Translational Sensitivity**



1283-81-032(T)

Fig. 3-17 X-Positional Sensitivity of 1X and 10X Matched Filters in Thick and Thin Emulsions



1283-81-033(T)

Fig. 3-18 Y-Positional Sensitivity of 1X and 10X Matched Filters in Thick and Thin Emulsions

Since the size of the matched filter depends upon  $(\lambda F)^{-1}$ , it is expected that, with the simple model cited, translational sensitivity will vary in a similar manner according to the "size sensitivity."

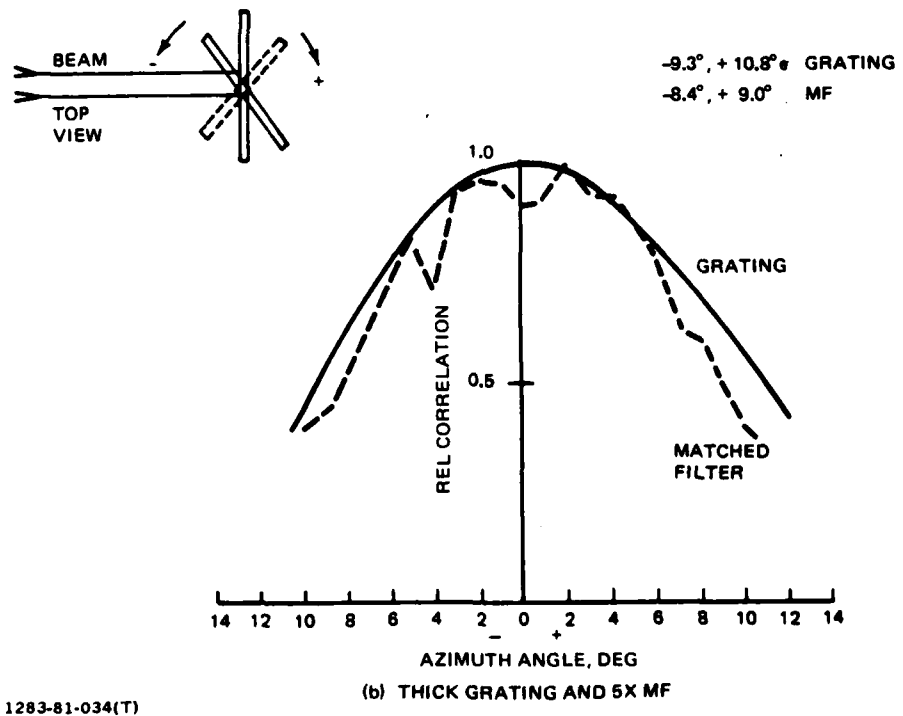
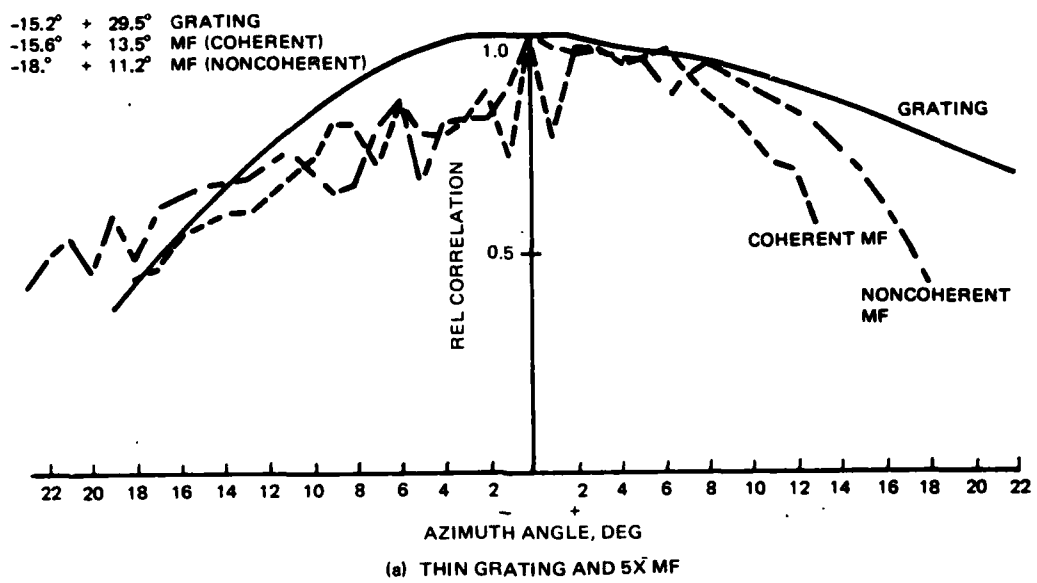
Azimuthal sensitivity is determined by the rotation of the matched filter or gratings about an axis lying in the emulsion-substrate plane and perpendicular to the reference-signal beam plane, and measurement of the first order signal or autocorrelation. It enables one to determine (a) alignment criticality, (b) the potential for carrier frequency modulation as a mode of increasing memory capacity, and (c) diffraction efficiency of the gratings.

In making these assessments, the matched filters were made and the auto-correlation signals measured as the rotation is effected. Then, plane gratings were made at the same carrier frequency and their first order transmission response was also determined as a function of azimuth angle.

Results for the two recording specimens are given in Fig. 3-19 for (a) the 120-02, 6  $\mu\text{m}$  emulsion, and (b) the 649 F, 17  $\mu\text{m}$  emulsion respectively. The figure illustrates the (arbitrary) sign designations. In the sign designation, (+) is in a direction which decreases the reference beam angle. The (-3 dB) maximum, first order efficiencies for the two silver halide emulsions were 4.5 and 5.2% respectively. For these two cases, the angular sensitivities are approximately  $\pm 14.6^\circ$  and  $\pm 8.7^\circ$ , respectively for the thin and thick emulsions. The grating responses were envelopes for the filter responses.

If allowance is made for the experimental variations concomitant with the correlation measurement vs the direct transmission measurement for the gratings, the 5x matched filters are seen to closely follow the grating response. The gratings were established by maximizing the interference fringe visibility and then establishing an exposure bracket. As with the MF, the grating selected was that which gave the maximum signal upon playback.

The Q-value of the two emulsions shows (Section 4) thin and approximately thick properties respectively, for the EK 120-02 and EK-649F photographic emulsions. The former is easily classified as a thin grating but, in the latter case, some properties of thick gratings start to appear. The relatively narrow tuning is evidence of this although unequivocally thick gratings are typically  $1 - 2^\circ$  wide at the -3 dB point. The closeness of the MF response might offer some evidence that



1283-81-034(T)

Fig. 3-19 Azimuth Angular Response of Thin and Thick Emulsions

the visibility of the gratings has also been properly maximized since the selection of the MF on the basis of the maximum autocorrelation signal does not otherwise guarantee this.

Kobuta (Ref 17) has shown that the signal and reference beams are recorded through the emulsion depth in a gradually diminishing way. This, of course, contributes to fringe plane formation in the thick emulsion. In Kobuta's model, the fringe visibility is relatively constant throughout the medium and its average value is a determinant for the measured diffraction efficiency which is a maximum of 3.7%. This value is less than that obtained here indicating that our results do not entirely fit Kobuta's model.

In many applications a full  $360^\circ$  coverage of an object is necessary in the memory to account for any possible object orientation. The angular or orientational sensitivity then dictates the number of views necessary. In the present case, the matched filters already described were used to determine this sensitivity. The object, an isolated single tank, was rotated and the autocorrelation signal measured over an interval to ensure a 3 dB decrease in magnitude. The results of this are shown in Fig. 3-20. Both coherently added image matched filters display a (3 dB) sensitivity of  $\pm 4.2^\circ$  with good symmetry, while the noncoherently added MF shows a sensitivity of  $+6.9^\circ$  slightly less than an isolated single MF at  $\pm 8.0^\circ$ . Based upon these results, 23 whole filters would be required of the single image variety in contrast to either nine or six whole filters needed when the 5x multiple image filters are constructed in either a noncoherent or coherent manner respectively.

Figure 3-21 illustrates the rotational sensitivity of a single tank MF derived from the simulation and should be compared to (a) the sensitivity of the single tank MF from Ref 7, and (b) to the results for the multiple image MF of Fig. 3-20. It can be seen that the results, allowing for slightly different spatial frequency band structures, are quite similar.

Highly sensitive single MF are high spatial frequency filters. Thus, one might also conclude that in spite of fringe visibility and autocorrelation optimizations, multiple image MF inherently tend to be high spatial frequency filters. Table 3-9 summarizes orientational results for coherent addition matched filters. It is clear that they all illustrate high frequency filter characteristics when allowance is made for experimental variability.

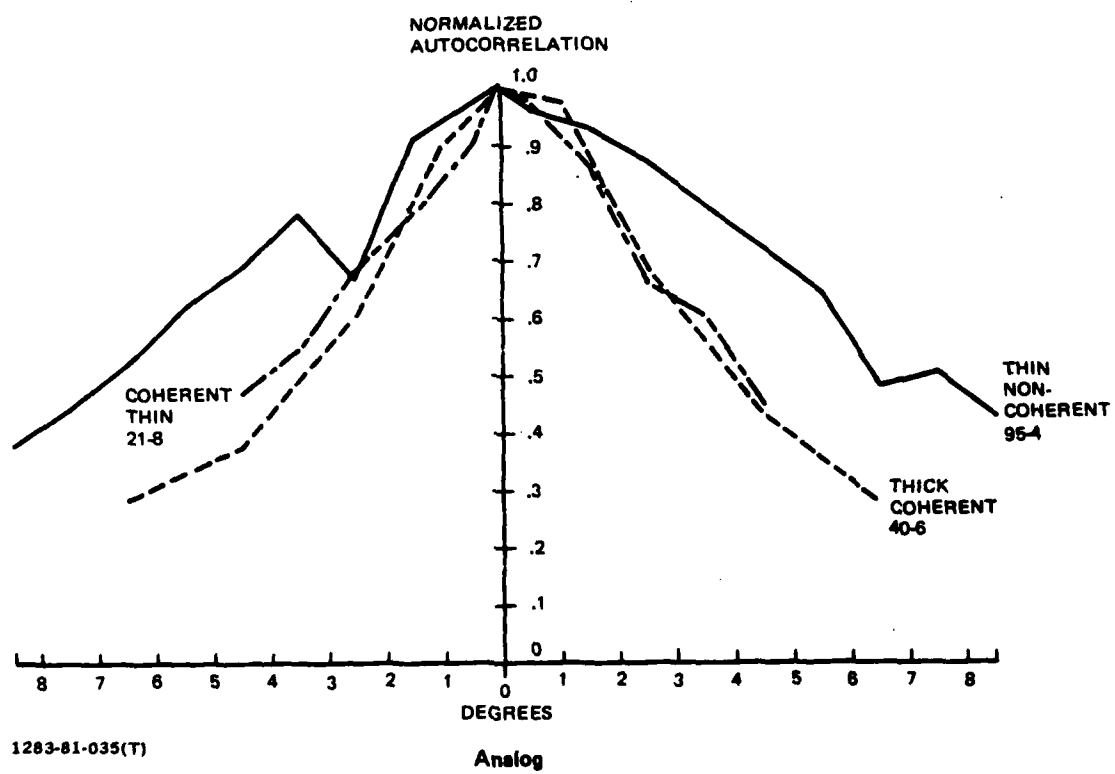
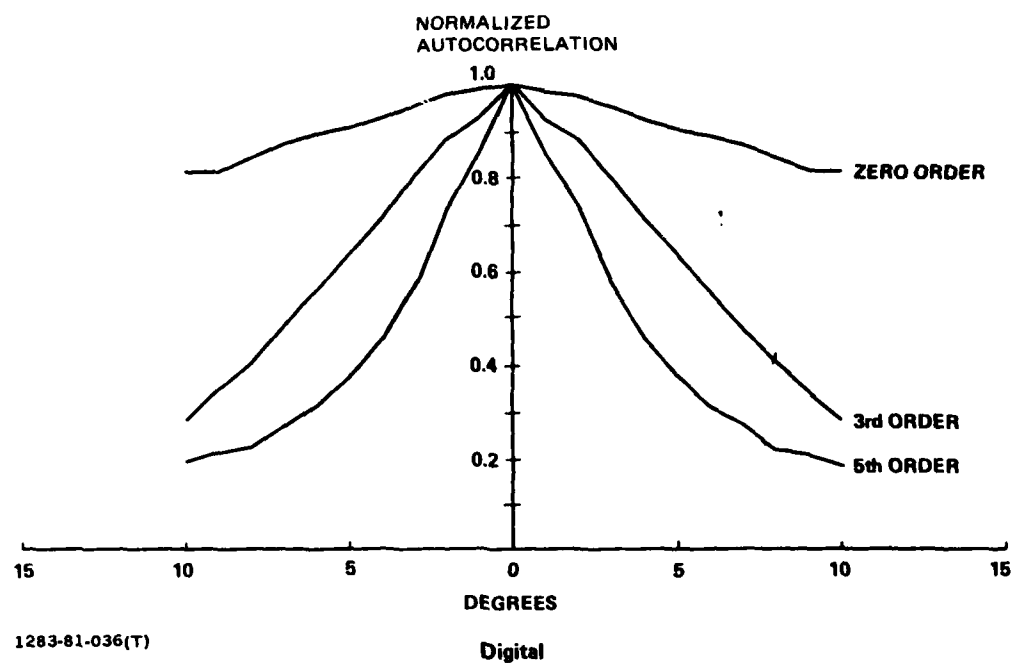
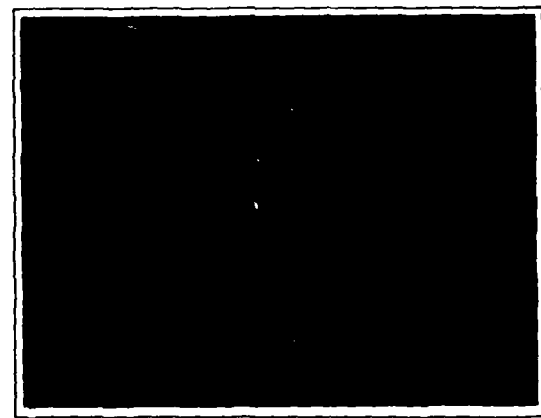


**Fig. 3-20 Rotational Sensitivity of Matched Filter**

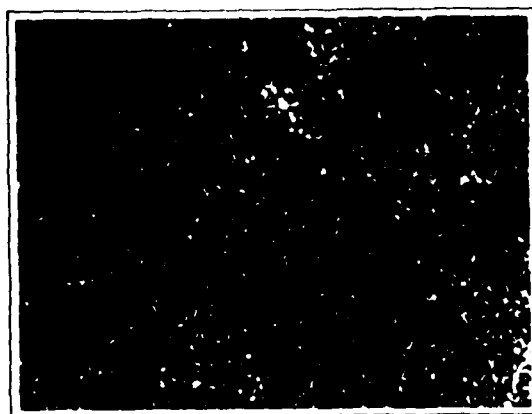


CORRELATION PLANE SIGNAL

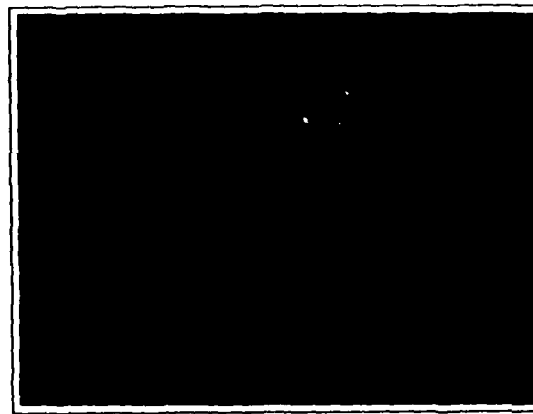


CORRELATION PLANE SIGNAL  
-6 dB

TERRAIN: WOODLAND WITH 1 VEHICLE  
MF: 10X COHERENTLY ADDED



CORRELATION PLANE SIGNAL



CORRELATION PLANE SIGNAL  
-8 dB

TERRAIN: SOUTHEAST ASIA WITH 5 VEHICLES  
MF: 10X COHERENTLY ADDED

1283-016(a)(T)

Fig. 3-21 Correlator Output with Terrain Image Input

**TABLE 3-9 ORIENTATION SENSITIVITY OF COHERENT ADDITION MATCHED FILTERS (THIN SIL HAL)**

SIZE OF COHERENT ADDITION	ORIENTATIONAL SENSITIVITY (DEG.)
1X	±7.76
2X	±6.60
3X	±7.15
4X	±7.63
5X	±4.90
6X	±6.34
7X	±5.9
8X	±7.73
9X	±5.30
10X	±5.46

1283-026(a)(T)

During the course of the program, coherent arrays continuously up to 10x, and at 15x, were used to make matched filters. In one test, the entire spread, 1x - 10x, was used, and the tank angular position of the multiples, which gave the maximum autocorrelation signal,  $\hat{c}$ , was used to orient the SE Asian terrain film upon playback. The results of this test are shown in Table 3-10. The values are clearly higher than an average S/C ratio for the size of the memory. Earlier tests have shown fairly conclusively that the S/C ratio follows the autocorrelation value in the multiple case, so the result is not unexpected. It does show, in conjunction with other results given earlier, that for good imagery, uniform S/C ratios result, and that high ratios are possible from multiple vehicle-terrain input imagery. Figure 3-21 illustrates the correlation plane for 10x image MF when the woodland and the SE Asian scene are played through. The figure shows two threshold levels, clearly illustrating the high S/C ratios present.

Finally, there were a series of tests in which a 15x image matched filter was made and three terrains played through the filter. The same angular position of the MF was used in each case to orient the input image, thus the position was somewhat arbitrary. The scans through the tank correlation are shown in Fig. 3-22. Once again, system acceptable S/C ratios were obtained. The filter used in these tests, shown in Fig. 3-23, was fabricated in dichromated gelatin and can be seen to be a high pass filter in the expanded views.

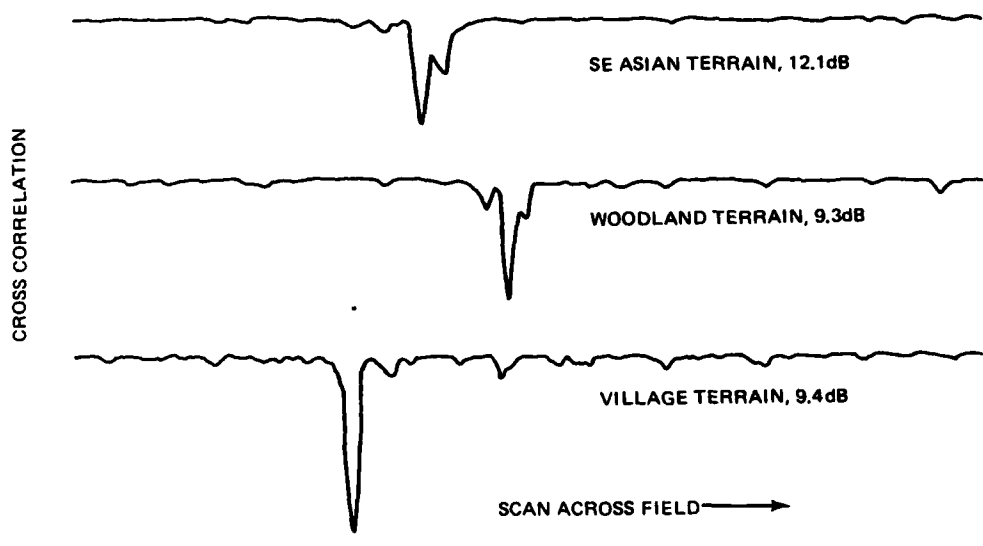
### 3.3.3 Multiplexed Carriers

The sequential storage of holograms with different reference beam angles is referred to as multiplexing carriers and angle codification. Much of the basic understanding of a grating recorded in a thick media traces to Kogelnik's coupled mode analysis (Ref 14), and the sequential recording to Kowarschik (Ref 21). The work was later extended to absorptive media by Kubota (Ref 17).

The region of interference between a signal beam S and a reference beam R is three-dimensional in nature so that when a recording medium is used, a small, though wavelength-appreciable, slice is made of the volume of interference. In the following geometrical model, the interference is exhibited along the line that the recording plane makes with the plane containing the reference and signal beam axes. This plane is the matched filter fabrication plane of symmetry.

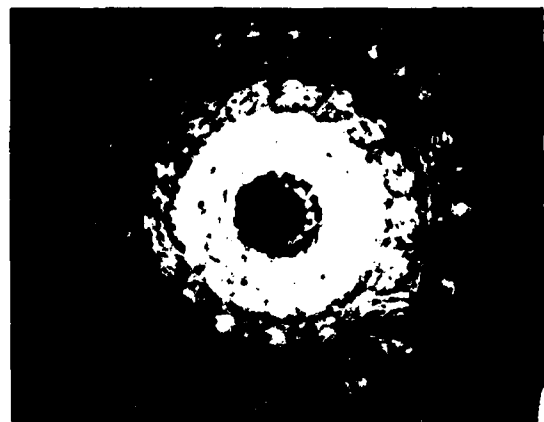
TABLE 3-10 S/C RATIO FOR MULTIPLE COHERENT MF USING  
SE ASIAN TERRAIN IMAGERY

NO. OF IMAGES USED TO MAKE MF	S/C RATIO (dB)
1X	13.66
2X	12.18
3X	10.99
4X	10.69
5X	7.99
6X	11.51
7X	12.88
8X	9.90
9X	7.60
10X	9.47
1283-027(a)(T)	

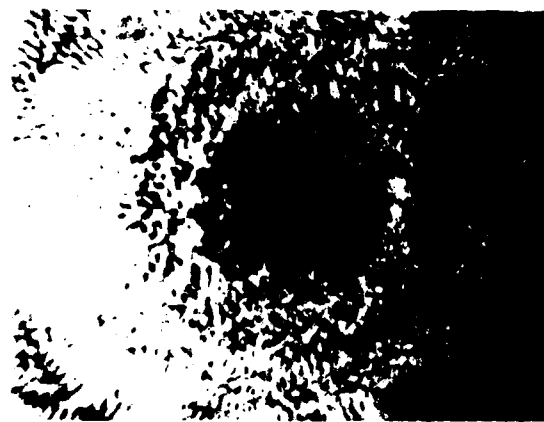


1283-81-037(T)

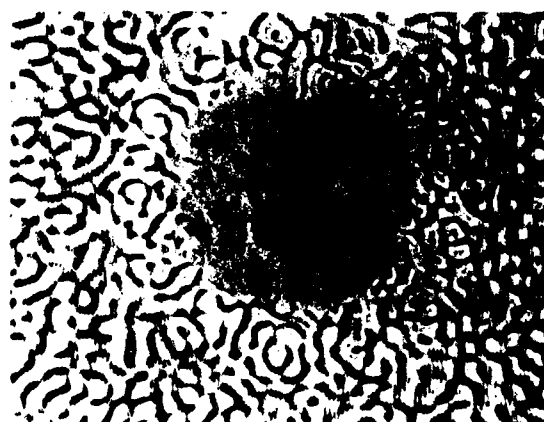
Fig. 3-22 A S/C Ratio of 15X MF in DCG Using 3 Terrains



VIEW OF 15X MF



4X EXPANSION



5X EXPANSION

1283-81-038(T)

Fig. 3-23 15x Matched Filter in Dichromated Gelatin

The geometry of recording is such that the plane of the object image is either on-axis ( $\theta_S = 0$ ,  $\theta_R \neq 0 = \theta$ ) and parallel to the recording plate, or at an angle to the plate normal so that

$$\theta_S = \theta_R = \frac{\theta}{2}$$

i.e., the total angle is the same in both cases.

The fringe angle  $\epsilon$  in the medium is

$$\epsilon = (I_{RE} + I_{SE})/2 \quad (3-7)$$

where  $I_{RE}$ ,  $I_{SE}$  refer to the reference, signal beams in the recording media. From Snell's law this becomes

$$\epsilon = (\sin^{-1}(\sin \theta_R/n) + \sin^{-1}(\sin I_S/n))/2 \quad (3-8)$$

where the incident beam is given as

$$I_S = \tan^{-1}((\sin \theta_S - (H/F) \cos \theta_S + (\xi/F)) / (\cos \theta_S + (H/F) \sin \theta_S)) \quad (3-9)$$

The spacing  $d$  of the fringes (on the surface) was given earlier and is obtained from the basic equation

$$d = \lambda / (\sin \theta_R \pm \sin \theta_S) \quad (3-10)$$

which for any spatial frequency (or physical location  $\xi$ ) requires that  $I_S$  be substituted for  $\theta_S$ .  $\theta_R$  is constant across the matched filter plane.

The results were given in Section 2, Fig. 2-6. A sampling of results for a range of appropriate spatial frequencies between  $\pm 9.5$  c/mm is shown in Table 3-11. These values of spatial frequency represent upper (practical) limits of some target objects used, but, by no means, the observable upper limits in a matched filter.

The equations for the fringe angles have been computed for the two general cases,  $\theta_S = \theta_R$ ;  $\theta_S = 0$ ,  $\theta_R \neq 0$ , and are shown in Fig. 3-24 for the on-axis fringe angle (i.e., at  $c = \xi/F$  or  $v = 0$ ). The limiting values are also shown and represent the upper limits of the extreme (practical) case, i.e., at  $f\# = .6$ ,  $F = 25$  mm and a 35 mm input imagery. In other words, these are the limits which cover the case when the object input film is located anywhere in the field during fabrication for the particular reference beam angle,  $\theta_R$ . The actual range of

**TABLE 3-11 RANGE OF CARRIER FREQUENCIES FOR A SPATIAL FREQUENCY  
SPREAD OF  $\pm 9.5$  c/mm**

$\theta_S + \theta_R$ (DEGREES)	$\Delta u = \pm 9.5$ C/MM AND:	
	$\theta_S = 0$	$\theta_S = \theta_R$
10	284 - 265	284 - 265
20	549 - 532	559 - 541
30	800 - 781	826 - 806
40	1020 - 1010	1086 - 1075
60	1369 - 1351	1587 - 1563

1283-028(a)(T)

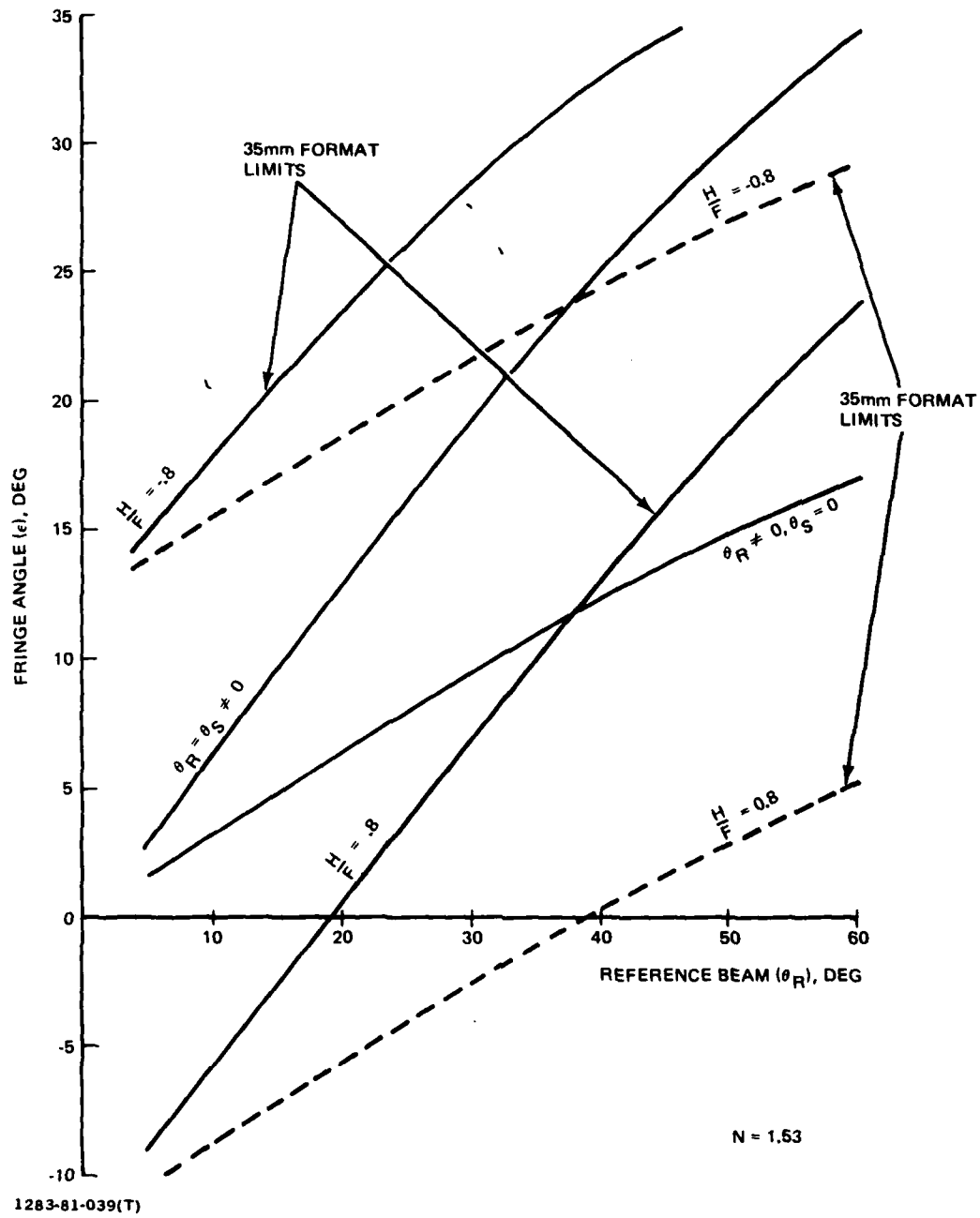


Fig. 3-24 Limits on Fringe Angles in Thick Media,  $N = 1.53$

values for  $c$  for a matched filter would be an increment about any of the (H/F) lines and depend upon the upper spatial frequency band limit established for the filter. The specific increment would be obtained from the equations by inserting  $\pm$  values for  $c = \xi/F$  for a particular  $v = H/F$  value.

From Fig. 3-24 it can be seen that the range of fringe angles is greater for the case  $\theta_S = \theta_R$ , than for  $\theta_S = 0$  even when allowance is made for a total angle comparison. For example, when  $\theta_S = \theta_R = 15^\circ$ ,  $\epsilon = 9.7^\circ$  while when  $\theta_R = 30^\circ$ ,  $\theta_S = 0^\circ$ ,  $\epsilon = 9.5^\circ$ . Thus, the two cases are not strictly identical ones for fringe angle.

Two cases were examined in this program, with  $\theta_S = 0^\circ$ ,  $\theta_R = \pm 10^\circ$ ; and  $\theta_R = +10^\circ$ ,  $+27^\circ$ . These yield, from the above equations,  $d = 2.81$ ,  $2.81 \mu\text{m}$  and  $d = 2.81$ ,  $1.07 \mu\text{m}$  respectively for fringe spacing. Also, we have  $\epsilon = \pm 3.1^\circ$  and  $\epsilon = + 3.1^\circ$ ,  $+ 8.7^\circ$  respectively for the fringe plane angles based upon  $N_g = 1.53$  and  $\lambda = 4880 \text{ \AA}$ . Computing the Bragg angle requirement,

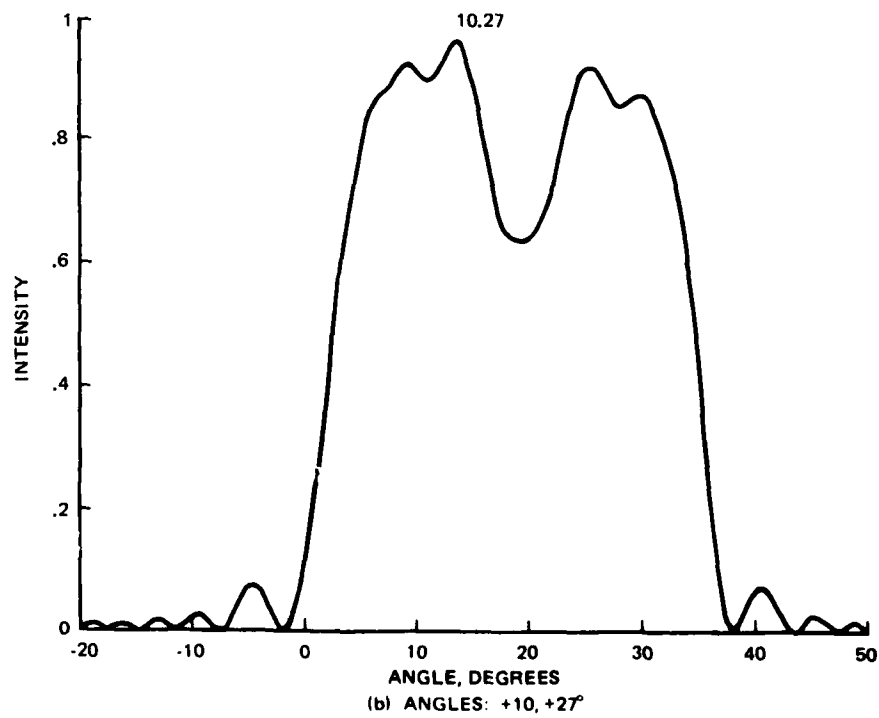
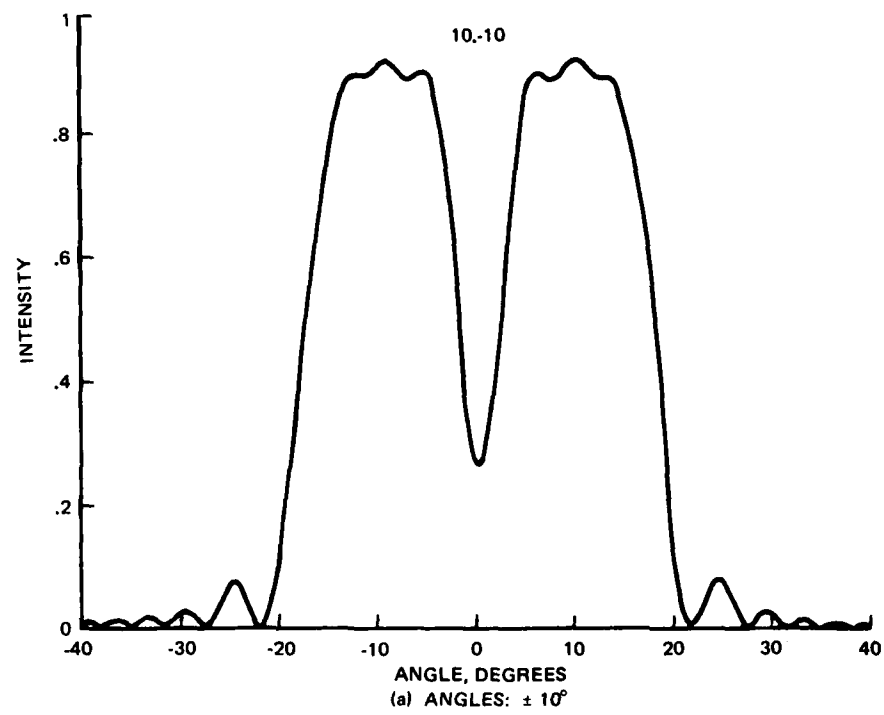
$$\sin \epsilon^+ = \frac{\lambda}{2N_g d} \quad (3-11)$$

we find  $BR = 30^\circ 15'$ , quite close to the actual angle in the symmetrical case considering the index uncertainties.

In treating sequentially (noncoherent) stored gratings in transmission volume holograms, Kowarschik (Ref 21) gives the diffraction efficiency for direct coupling and sinusoidal modulation:

$$\begin{aligned} n &= n_1 + n_2 \\ &= \frac{|D_1|}{|A|} |S_1|^2 + \frac{|D_2|}{|A|} |S_2|^2 \end{aligned} \quad (K19)$$

where the  $S_i$  are the signal waves and the parameters are contained in the  $D_i$ ,  $A$  terms. The applicable equations are given in Appendix C. Using  $\lambda = 4880 \text{ \AA}$ ,  $N = 1.53$ , thickness =  $13 \mu\text{m}$  and a modulation  $n_i = 1.5 \times 10^{-2}$ , the two cases were programmed and computed. The results are shown in Fig. 3-25 and yield HPFW angles of  $\pm 15.5^\circ$ , and  $+ 15.5^\circ$ ,  $+ 16.2^\circ$  respectively for the two cases.



1283-81-040(T)

Fig. 3-25 Kowarschick Formulation Applied to  $O_R = +10^\circ$

Gratings were prepared in dichromated gelatin and their responses measured as the recording plates were rotated. In both cases, the detector is placed along the reference beam axis as the plate is rotated. These results are shown in Fig. 3-26 for the corresponding cases. The angles are +13.1, -12.7 and +13.4, +4.3° respectively. The symmetric case is in close agreement with Kowarschick, but for the asymmetric case there is considerable disagreement. Matched filters were fabricated and the correlations measured under the same conditions. These results are shown in Fig. 3-27 where the HPFW angles are +11.2, +5.7° respectively, in agreement with the grating test results. In carrying out these tests, experimental restrictions required the 27° angle to be fabricated first.

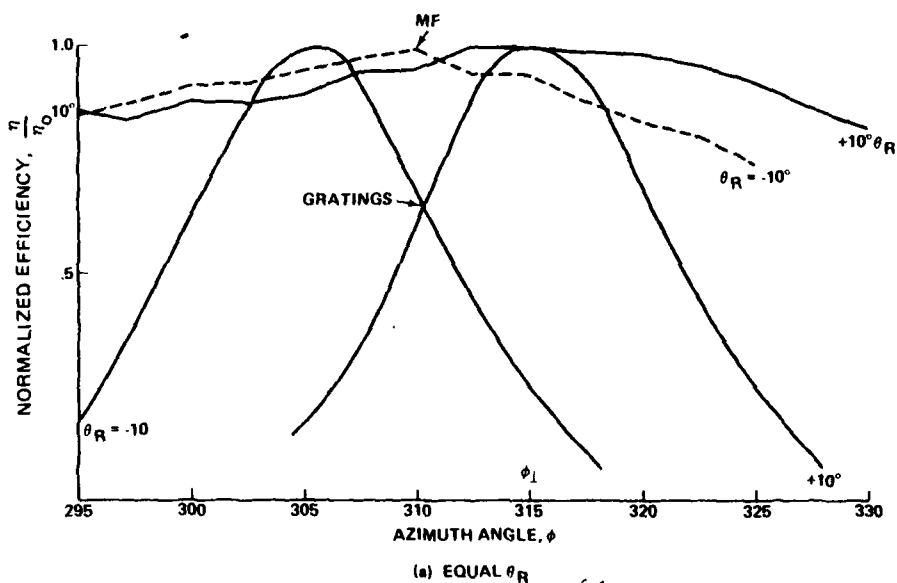
In order to verify earlier thin emulsion results, MF were fabricated at the two angles  $\pm 10^\circ$  and the correlation measured. These results are included in Fig. 3-26(a) and show the expected uniform response.

Figure 3-28 illustrates microscopic views of a 5X image MF in dichromated gelatin with (a) one and (b) two carriers, specifically in this case,  $\pm 10^\circ$ . When the two MF are perfectly registered, or nearly so, there is considerable difficulty in bringing the image in focus. When not registered, one MF and then the other are able to be observed by slight microscopic adjustment.

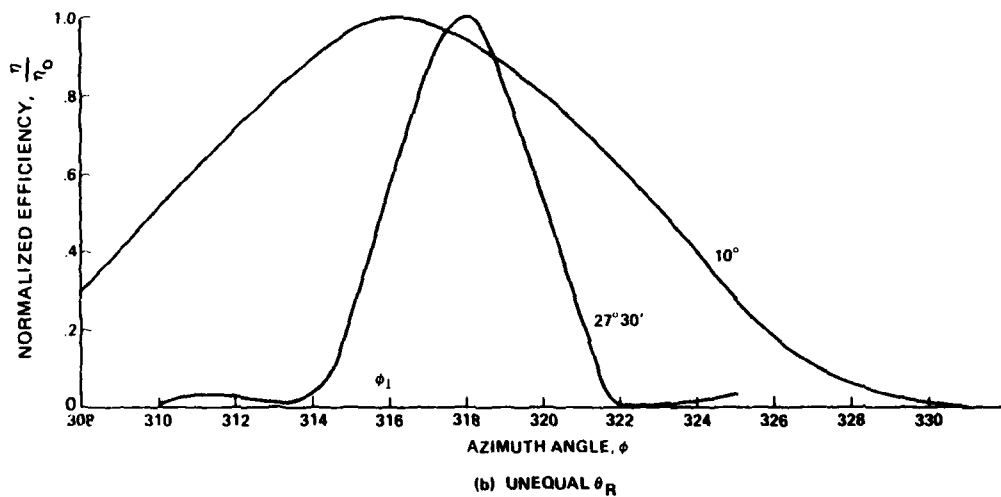
In a final test of the multiplexed carriers, a 15x image MF was constructed and the correlation measured. Then, using the SE Asian scene with 5 vehicles in the field, the S/C ratio was measured. In the first case, the correlation result (using one M-60 tank position to measure the correlation) shows (Fig. 3-29) the same result obtained for the single MF. That is, the 27° angle has a higher response and an angular sensitivity of 5.2° while the 10° response is lower with an estimated 13° angular response.

Secondly, the same 15x matched filter was used for the terrain scene evaluation. The result is shown in Fig. 3-30. There is a decrease in the S/C ratio as well as an expected decrease in overall signal strength.

Based upon the foregoing, one can obtain usable large matched and multiplex two such filters, and obtain acceptable S/C ratios. However, unless the MF are symmetric about the normal signal beam, the angular response of the filters is uneven. Furthermore, the basic response of the filters leads to the necessity of



(a) EQUAL  $\theta_R$



(b) UNEQUAL  $\theta_R$

1283-81-041(T)

Fig. 3-26 Response of Multicarrier Gratings and MF in DCG

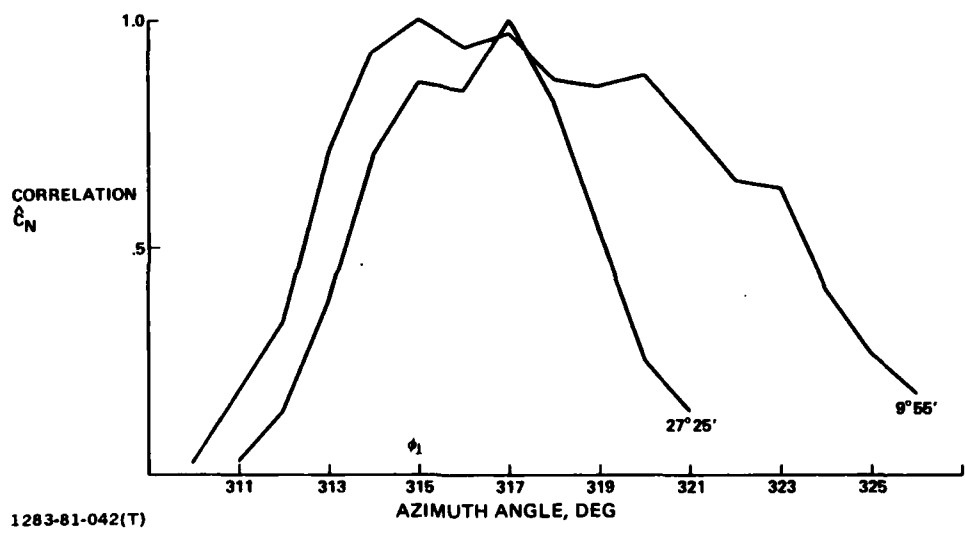


Fig. 3-27 Azimuth Sensitivity of MF With Multiplexed Carriers



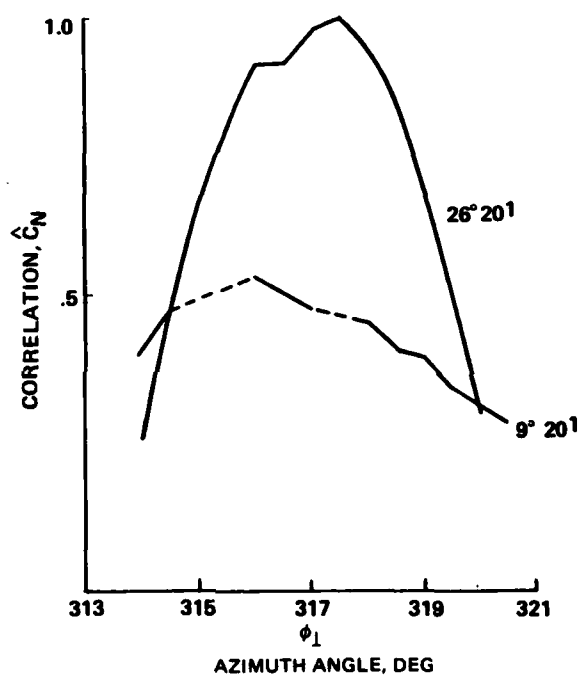
(a) ONE CARRIER



(b) TWO CARRIERS

1283-81-043(T)

Fig. 3-28 5x MF in DCG With One and Two Carriers



1283-81-044(T)  
Fig. 3-29 Response of 15X COH with Two Carrier Frequencies

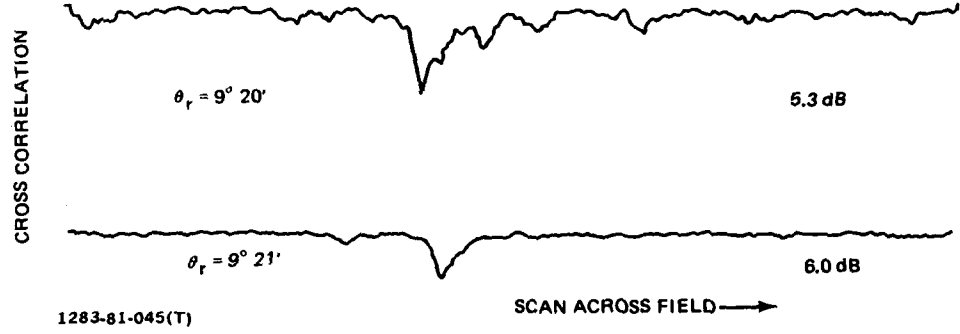


Fig. 3-30 S/C Ratio of a Multiplexed Carrier 15X MF in DCG Using SE Asian Scene

**using two correlation planes. The Bragg angle requirements for maximizing the signals in the two correlation planes can be met simultaneously, a significant alignment.**

#### 4 - MEMORY RECORDING MEDIA

This study included the examination of materials such as dichromated gelatin (DCG), photographic silver halide emulsions (SILHAL), and photopolymers (PP), not as a materials study but as a study of recording since these materials represent individual and different recording mechanisms (Fig. 4-1).

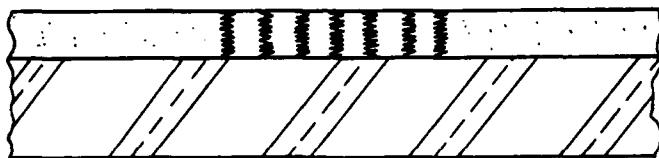
Silver halide photographic emulsions for amplitude holograms are well known and are an inexpensive, readily available, widely used storage medium. They are, therefore, a valuable optical memory resource. Two types of Eastman-Kodak SILHAL plates were used in our program: 120-02 and 649F. The nominal thicknesses were 6 and 17 $\mu\text{m}$ , respectively. Depending upon wavelength and reference beam angle, the latter film thickness can approach and display some characteristics of thick films (e.g., Ref 14), but never quite be classified thick by the widely accepted Q-criterion (Ref 15),

$$Q = (2\pi \lambda t) / n_0 d^2 \quad (4-1)$$

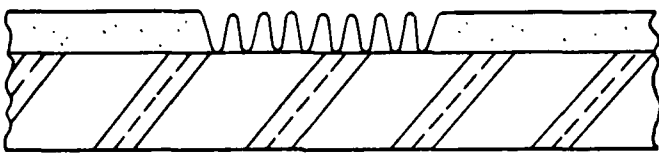
where  $\lambda$ ,  $t$  are the wavelength and emulsion thicknesses respectively for a film having an index of refraction  $n_0$  with fringes recorded at a spacing of  $d$ . The Q-factor is summarized in Fig. 4-2 for the film and fabrication parameters employed in the program. The factor itself has recently been reassessed so that the modulation level  $n_1$  is also included (Ref 16).

The SILHAL films used in the program have sufficient dynamic range and resolution to record wide band matched filters. Figure 4-3 illustrates a scan with a microdensitometer of the eighth to fifteenth order of a MF showing that wide band spatial frequency matched filters can be recorded, although, as shown in Section 1, the memory element as defined has about one half of the spatial frequency content illustrated in Fig. 4-3.

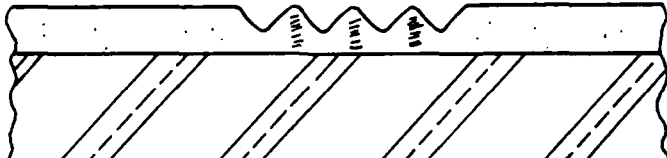
Some differences were noted between the thin and thick silver halide emulsions. As recording media, each type must be optimized for the specific set of conditions on an individual basis. For example, there are measurable differences between exposure time and smaller differences for beam ratio adjustment between thick and thin SILHAL. Table 4-1 illustrates these differences for 1x,



(a) PHOTOGRAPHIC EMULSIONS



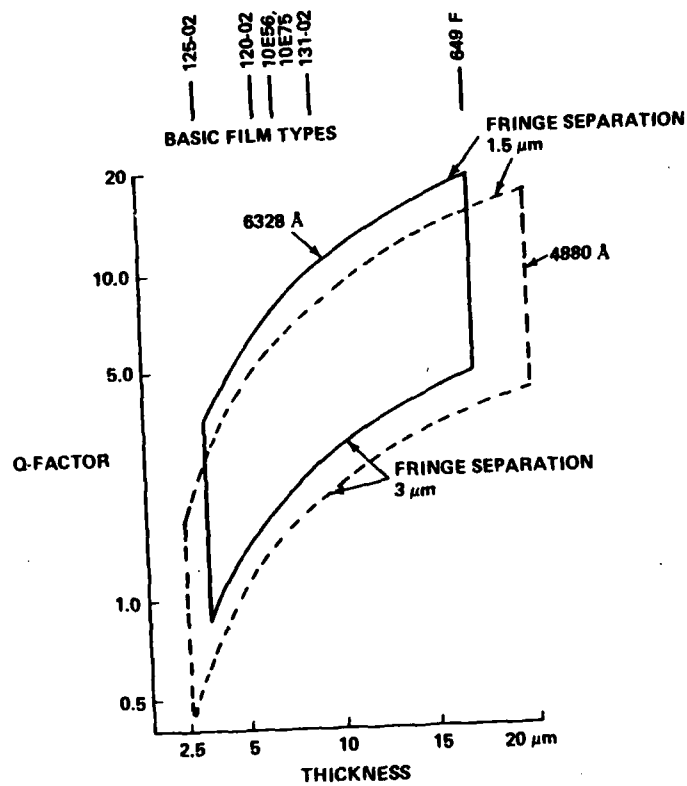
(b) DICROMATED GELATIN



(c) PHOTOPOLYMER

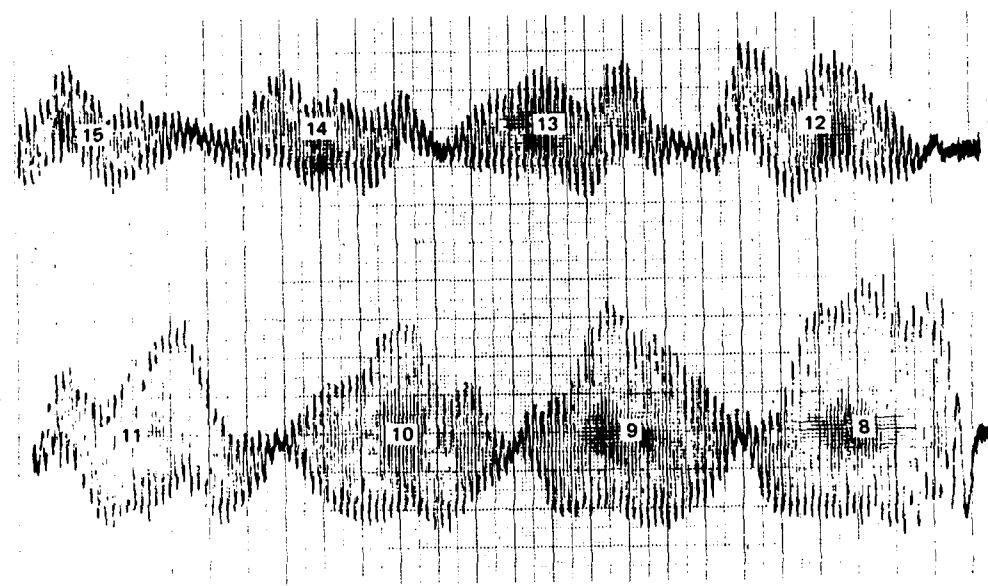
1283-81-046(T)

Fig. 4-1 Memory Recording Mechanisms for Media



1283-81-047(T)

Fig. 4-2 Thickness Criteria



1283-81-048(T)

**Fig. 4-3 Scan with Microdensitometer of Higher Orders of Matched Filter**

TABLE 4-1 POSITIONAL DISTRIBUTION OF AUTOCORRELATIONS OF COHERENT MATCHED FILTERS USING THICK AND THIN EMULSIONS

N	ORIENTATION ANGLE (360) DEG. N	CORRELATION OF COHERENT IMAGERY					
		1X		5X		10X	
		THICK	THIN	THICK	THIN	THICK	THIN
1		1.000	1.000	.334	.340	.030	.038
2				.270	.270	.024	.024
3				.219	.276	.018	.017
4				.181	.298	.021	.024
5				.244	.271	.016	.023
6						.012	.020
7						.012	.024
8						.021	.035
9						.013	.021
10						.027	.027
N-AVERAGE 1283-029(a)(T)		1.000	1.000	.250	.291	.019	.025

5x, and 10x matched filters. In addition to the variations between each element of a particular coherent image array (Table 3-6), it can be seen that there is some improvement when the thinner emulsion is used. However, it has also been observed that when constant conditions are used and optimized for the thick SILHAL emulsion, there is a significant increase in the efficiency of the thick emulsion over the thin due to the Bragg-like improvement.

Figure 4-4 shows a 200X scanning electron microscope (SEM) picture of a 5x coherently added image matched filter with a blowup of one section. The details of the surface relief in the DCG should be noted and compared with the microscope picture of the 5X in the previous section.

Matched filters were selected which were of comparable quality but fabricated in silver halide and dichromated gelatin. They were then compared in a common test for their angular response and signal-to-clutter ratio. The results are shown in Table 4-2.

Basically, their performance is comparable in terms of response quality. In a separate test, the efficiency of DCG vs SILHAL was determined and it was found that DCG was 10x more efficient than a comparable filter in thin silver halide.

DCG is most interesting because the molecular nature of the medium has the potential of high efficiency without (silver) grain scattering. This, in turn, should lead to memories with the maximum extractable capacity. The mechanism of recording is primarily one of producing a variation of the surface contour. We have drawn upon contemporary AFOSR sponsored programs (Ref 18 - 20) during these efforts in addition to extending some of the technology. A detailed review of our experiences in establishing appropriate procedures is contained in Appendix A.

Initially it was intended that, in addition to the two materials cited, some form of photopolymer be included in order to extend the work to media in the thickness range  $20 \leq t \leq 100$  micrometers. A search was conducted to determine likely candidate materials, the most promising of which were:

- Urethane aligomers (Thiokol)
- Acrylic allylic (R and H)
- Methacrylic allylic (R and H)
- Methyl Cyanoacrylates (Loctite) (Ref 27)
- Unspecified monomer-initiator system (duPont)
- Acrylate-organic acid initiators (NRC)

AD-A108 555

GRUMMAN AEROSPACE CORP BETHPAGE NY RESEARCH DEPT

F/6 9/2

INVESTIGATION OF LARGE CAPACITY OPTICAL MEMORIES FOR CORRELATOR--ETC(U)

OCT 81

K G LEIB, J MENDELSONN

F49620-78-C-0051

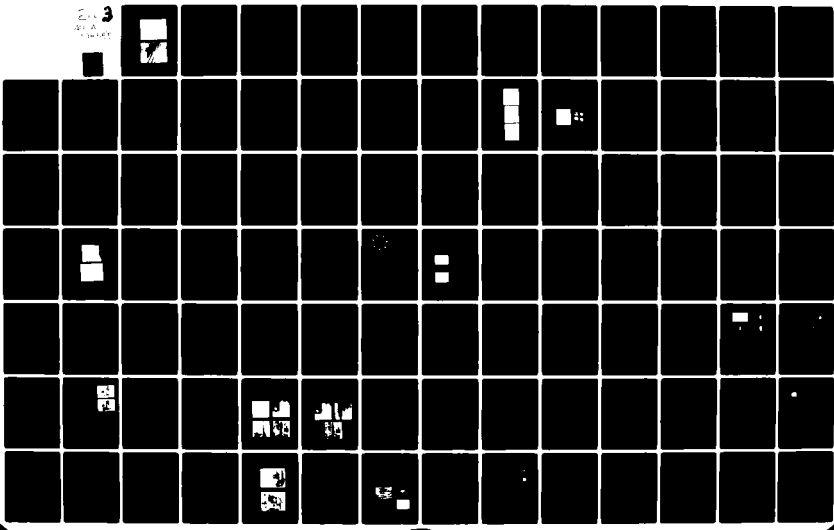
UNCLASSIFIED

RE-634

AFOSR-TR-81-0802

NL

3  
A-A  
VIA



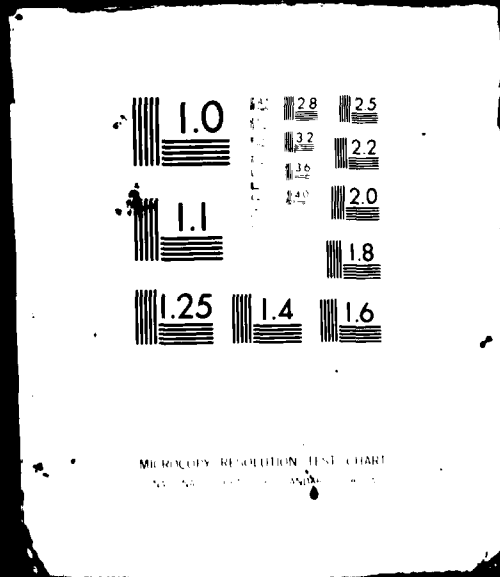
19

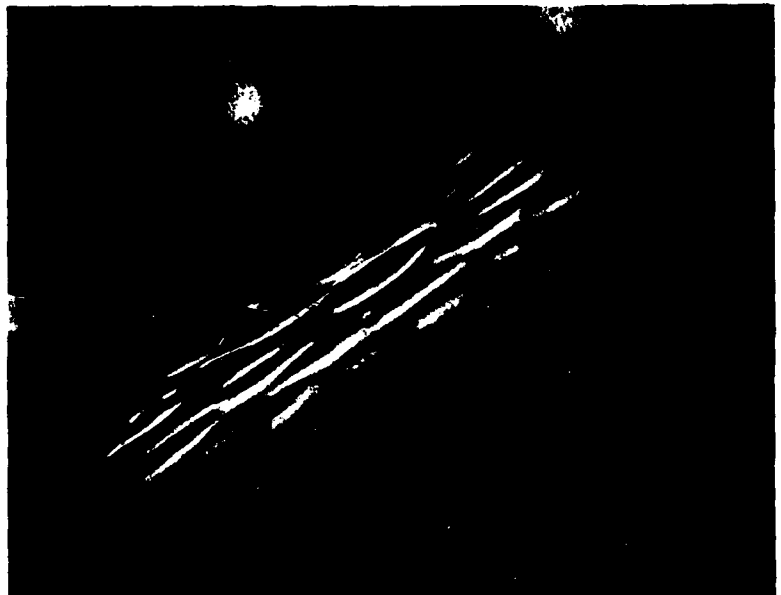
100

100

100

2 OF  
AD-A  
108555





(a) 200X



(b) BLOWUP OF AREA NEAR BURN

1283-81-049(T)

Fig. 4-4 200x SEM of 5x COH MF in Dichromated Gelatin

TABLE 4-2 MATCHED FILTER MEDIA COMPARISON

MF GROUP	# IMAGES	COH/NON	THICK/THIN	DCG/SILHAL	S/C (dB)	ANGULAR RESPONSE
A	1X	—	THIN	DCG	10.6	N/A
	1X*	—	THIN	SILHAL	11.2	±8.0°
B	5X	COH	THIN	DCG	7.2	±6.3°
	5X	COH	THIN	SILHAL	7.0	±6.2°
C	1X	—	THICK	DCG	6.1	±9.1°
	1X	—	THICK	SILHAL	6.5	±7.8°
1283-030(a)(T)						

Several practical factors dictated preferences in choosing materials. When such factors as activation wavelength, fabrication, and availability were considered, only the last two offered any reasonable promise within the program objectives. Use of the discontinued duPont material (Ref 26) further limited the list when the only material available was found to be several years old and unreactive. Thus, the best choice was the last material (Ref 28).

A number of plates were prepared in the usual way with 25  $\mu\text{m}$  and 50  $\mu\text{m}$  thicknesses, both of grating and matched filter holograms.

Serious problems were encountered while working with the acrylate-organic acid initiators. In all cases, the recordings were extremely noisy, inadequately defined holographically, and were not able to be made permanent in their recorded state. A number of experimental procedures and techniques were devised to improve performance. After an extended investigation of this material, it became clear that the prospect of obtaining memory elements in the best choice of photopolymers with acceptable quality was not possible within the scope of the program, and the effort was discontinued.

Our experience with photopolymers is not surprising. Interest, as evidenced by a paucity of technical papers, reports, and a very limited commercial availability, infer poor performance of these materials at the present time. Future developments, or a dedicated, in-depth study of available materials may someday result in acceptable MF.

Based upon the parameters used in the program, or those postulated as limit conditions, the efficiency of the thick medium was examined with the results of Kogelnick (Ref 14) as a starting point. Alferness (Ref 23) and others (Ref 24, 25) have examined the angular sensitivity of gratings in thick media in order to establish intervals between angles to provide angular separability, or isolation.

The efficiency is given by

$$\eta = [\sin(\nu^2 + \xi^2)^{\frac{1}{2}}]^2 / (1 + \xi^2/\nu^2) \quad (4-2)$$

where it can be shown that

$$\xi = \frac{[\cos(\phi - \theta) - (\lambda/\Lambda)(1/2N)2\pi d]}{[\Lambda \cos \theta - (\lambda/N) \cos \phi]} \quad (4-3)$$

and

$$v = (\pi n, d/\lambda) [\cos \theta (\cos \theta - (\lambda/\Lambda))(\cos \phi/N)]^{-1} \quad (4-4)$$

A number of parameters have been previously defined but, for convenience, all are given in Table 4-3 with typical values used in the computations.

In carrying out the computations we are again concerned with the two cases,  $\theta_S = 0$ ,  $\theta_R$ , and  $\theta_S = \theta_R \neq 0$ .

First, the efficiency was determined as a function of reference beam angle with thickness and modulation taken as constants. One value for the latter (i.e., .01) was taken close to the modulation value of Kowarschik as used in the previous section. The results for  $\theta_S = 0$  and  $\theta_S = \theta_R$  are shown in Fig. 4-5 and 4-6 respectively.

In the first case, the influence of modulation for a given thickness as discussed by Moharam (Ref 16) is apparent. In each instance the thicker medium yields the larger efficiency with the  $P = 20$ ,  $N = .01$  combination almost constant for any reference beam angle of interest. The lower modulation yields the higher efficiency in each of the two groups.

The second case (Fig. 4-6) was the usual  $\theta_S = \theta_R$  where the total angles would be the same as the  $\theta_S = 0$  case above. The abscissa is expanded to reflect this quality. It is apparent that care must be exercised with the symmetrical configuration in selecting an appropriate reference beam if a low pass MF is desired (i.e., where  $v = 0$ , or near it).

Due to the uncertainties in DCG index, the efficiency of the MF for variations in index of refraction,  $N$ , was also examined at a constant modulation  $N = .04$ . It was found that, while the efficiency varied with reference beam, it was fairly constant with index. Thus, an average value was taken and is summarized in Table 4-3. It can be seen that, like the results of Fig. 4-5, 4-6, there is a significant difference in efficiency between the 10 and 20  $\mu m$  cases, as well as between the asymmetrical ( $S = 0$ ) and symmetrical ( $S = R$ ) cases.

Finally, in the same group of computations, the variation across a matched filter ( $\xi/F$ ) was examined for fixed index and modulation. These results are shown in Tables 4-4 and 4-5 and reveal a significant change across a filter for the large reference beam angles, and a larger variation for the symmetrical case,  $S = R$ .

TABLE 4-3 PARAMETERS FOR EQUATIONS 4-2, -3, -4

$\phi$	IS THE ANGLE OF THE GRATING VECTOR K BUT ALSO, $(\pi/2-\epsilon)$ WHERE $\epsilon$ IS THE FRINGE PLANE ANGLE GIVEN EARLIER
$\theta$	ANGLE OF INCIDENCE IN THE MEDIUM;
$\theta_0$	BRAGG ANGLE MEASURED FROM FRINGE PLANE, $\sin\theta_{BR} = \lambda/2NT$
$\Delta\theta$	DEVIATION FROM BRAGG ANGLE, OR DIFFERENCE BETWEEN REQUIRED BRAGG ANGLE AND INCIDENT ANGLE IN MEDIUM,
$N$	REFRACTIVE INDEX (1.56);
$N_1$	MODULATION (0.01 - 0.04);
$P$	MEDIA THICKNESS (10 - 20 $\mu m$ );
$\lambda$	FABRICATION OR PLAYBACK WAVELENGTH AS REQUIRED;
$c$	SLANT FACTOR, THE RATIO OF THE OBLIQUITY FACTORS = $C_R/C_S$
$C_R$	$\cos\theta$
$C_S$	$\cos\theta - \frac{K \cos \phi}{\beta}$
	$= \cos\theta - \lambda/DN \sin\epsilon$
$D$	FRINGE SPACING
$K$	$2\pi/\lambda$
$\beta$	$2\pi N/\lambda$
1283-031(a)(T)	

TABLE 4-4 AVERAGE EFFICIENCY (%) FOR  $n_1 = .04$  INDEX INTERVAL,  
 $1.52 - 1.56$

$\theta_R$	P ( $\mu\text{m}$ )	
	10	20
10	27.66	80.04
30	19.13	61.86
60	1.44	5.67

(a) FOR S = 0

$\theta_R$	P ( $\mu\text{m}$ )	
	10	20
5	19.80	62.62
10	12.29	24.55
30	9.30	0

(b) FOR S = R

1283-032(a)(T)

TABLE 4-5 AVERAGE EFFICIENCY (%) FOR  $n_1 = .04$  AT  $N = 1.55$   
FOR VARIOUS  $\nu$

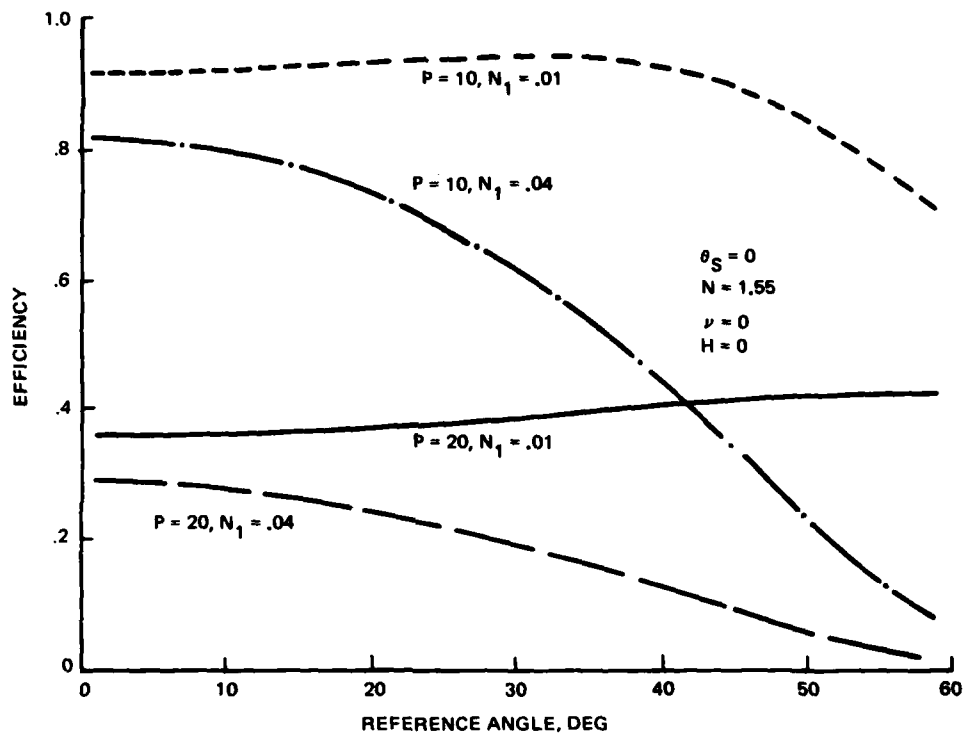
$\nu$ OR NORMALIZED DISTANCE, $\xi/F$			
$\theta_R$	0.0158	0	-0.0175
10	78.99	80.02	79.88
30	55.20	61.82	61.05
60	0.50	5.68	12.42

(a) FOR  $S = 0$

$\nu$ OR NORMALIZED DISTANCE, $\xi/F$			
$\theta_R$	0.0175	0	-0.0175
5	51.94	62.26	71.36
15	15.21	24.72	15.67
30	0	0	1.06

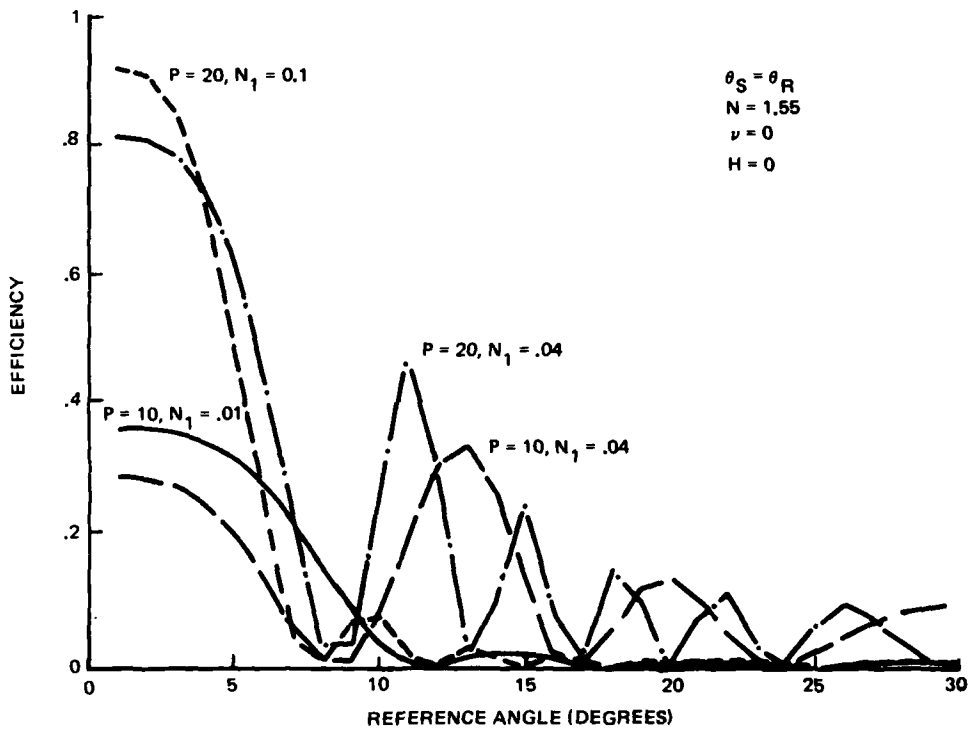
(b) FOR  $S = R$

283-033(A)(T)



1283-81-050(T)

Fig. 4-5 Efficiency of Recording Medium,  $\theta_S = 0$



1283-81-051(T)

Fig. 4-6 Efficiency of Recording Medium,  $\theta_S = \theta_R$

The net experience then is that either thin or thick silver halide, or dichromated gelatin can be satisfactorily used to record correlator memory elements. The trade-offs between them are not to be based upon the performances as used in the program, but upon other factors such as cost, speed, etc. Given sufficient resources, the dichromated gelatin is to be preferred for large memories.

## 5 - OPTICAL MEMORY CAPACITY

### 5.1 CAPACITY BASED UPON FREQUENCY CONTENT OF MF

In addition to specific techniques for storing matched filters as described in detail earlier, one is also interested in the number of such techniques which might concurrently be used on the optical memory capacity.

Figure 1-2 illustrated the basic storage element. The region defined by the element is circular with a radius equal to N times the optimizing spatial frequency,  $v_o$ , which, for the M-60 tank, was 3.33 cycles/mm. It is believed that each vehicle would be somewhat different. In the case of the M-60,  $N = 2.5$  to  $3$ , a spatial frequency cut-off in which the autocorrelation signal is reduced to 0.27 dB of its "infinite bandwidth" level.

In a regular array then, the cross talk does not exceed 6%. One matched filter requires  $(N v_o / S) \text{ mm}^2$  area where  $S = (\lambda F)^{-1}$  is the "system constant." As before,  $\lambda$  = wavelength of the Fourier transformation and  $F$  the focal length. If we include  $G$  = the geometrical packing factor,  $S$  = the split spectrum factor, and  $P$  = the overlap or multiplicity factor, then the capacity for matched filters of a single species of target becomes:

$$C_A = (25sPG)/(Nv_o\lambda F)^2 \text{ matched filters/cm}^2 \quad (5-1)$$

where  $v_o$ ,  $\lambda$ , and  $F$  are given in cycles/mm, mm, and mm respectively. Using the realistic values:  $S = 1$ ,  $P = 5$ ,  $G = 1.16$ ,  $N = 3.0$ ,  $\lambda = 0.488 \text{ m}$ , and  $F = 25 \text{ mm}$ , then, for example,

$$C_A = 2670 \text{ (matched filters/cm}^2\text{).}$$

Table 5-1 illustrates some values of unit capacity for some practical system cases. Any value can be appropriately modified by multiplying the capacity given by an overlap or multiplicity factor, packing density, and so forth.

It is apparent that a large number of matched filters can be packed in a small area. It is also apparent that when one considers large memories, fabrication goes beyond the realm of manual processes and computer controlled or computer generated memories are a necessity.

TABLE 5-1 UNIT CAPACITY FOR SOME PRACTICAL CASES

FOCAL LENGTH F (mm)	WAVELENGTH (ANGSTROMS)	CAPACITY
		$C_A$ (MF/cm <sup>2</sup> )
25	4880	1683
	6328	1001
200	4880	26
	6328	16
360	4880	8.1
	6328	4.8
720	4880	2.0
	6328	1.2
1000	4880	1.05
	6328	0.63

1283-034(a)(T)

Secondly, there is a power division with increasing size requiring large laser power. Earlier (Ref 7), it was shown that the power level employed at that time was  $10^{-4}$  what might be used before emulsion damage occurred for the media employed (silver halide, bleached silver halide). In the current program, the limits on dichromated gelatin damage threshold were not established. However, it was determined that, as expected, it is well above that of silver halide.

Thus, it is clear that there are some choices available when a specific memory is designed, size requirements developed, the optics established, and a wavelength chosen.

The formula above can, incidentally, be applied to bit-by-bit memories and, with acceptable state-of-the-art values, yields  $10^6$  bits/cm<sup>2</sup>, a value often quoted in the literature.

The overlay or multiplicity factor referred to above does not take multiplexed carriers into consideration. A factor accounting for the impact of this has not been incorporated because of the need to have additional correlation planes. Yet, the ability to use multiplexed carriers to increase the memory density is real.

Based upon Eq 3-11, one can at least determine the limits on multiplexing as they affect the capacity. Figure 5-1 illustrates the range of fringe angle planes for the practical situation of processing a 35 mm format with transform lens focal lengths of 25 to 1000 mm for reference beam angles of 5° and 45°. The curves for both are similar, as are the limit curves for any reference beam except, of course, for the asymptotic limits. Also, negative reference beam angles are symmetric. The angles previously computed for the multiplexed symmetrical case can be seen to lie within the ± 10° reference beam curves.

## 5.2 CAPACITY BASED UPON FILM LIMITS

The use of silver halide as the recording medium raises the question of capacity limits restrained by finite resolution of the medium.

An upper limit to the number of storage addresses in a holographic optical memory due to the finite resolution capability of the recording medium used to store the holograms may be established. Assume that the recording medium response to the source of illumination used in the holographic fabrication process is:

$$R(x,y) = E_0 + \Delta E(x,y)*m(x,y) \quad (5-2)$$

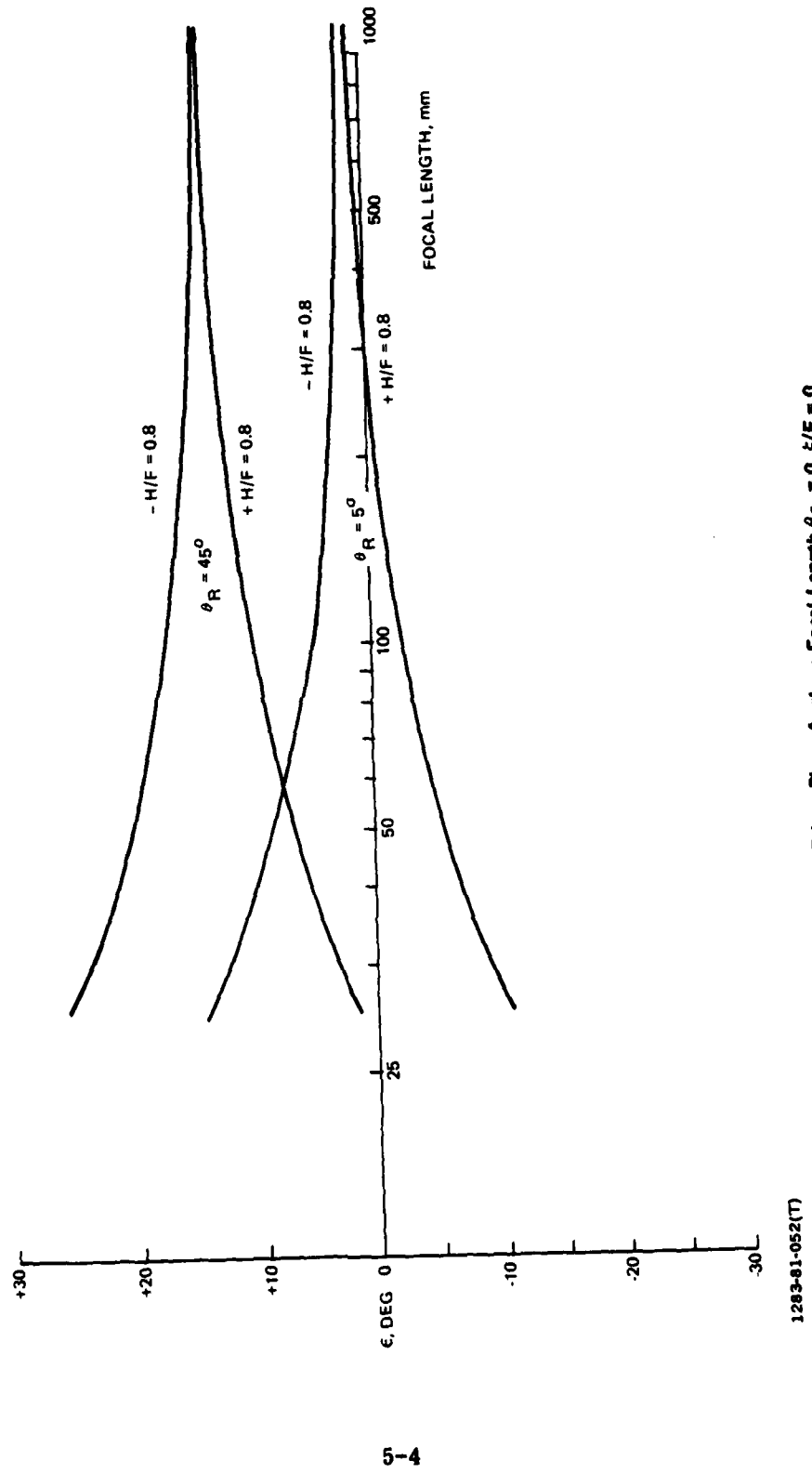


Fig. 5-1 Fringe Plane Angle vs Focal Length  $\theta_S_r = 0, \xi/F = 0$

1283-81-052(T)

where  $R(x, y)$  denotes the spatial variation of the response,  $E_0$  is the average illumination,  $E(x, y)$  is the information-carrying portion of the illumination (assumed to be a small deviation about the average illumination), and  $E^*m(x, y)$  indicates a linear relationship with a fixed point spread function  $m(x, y)$  whose Fourier transform  $M(f_x, f_y)$  represents an equivalent MTF of the recording process. If the storage medium yields an amplitude hologram it will be assumed that the transmission through the hologram is proportional to the exposure during fabrication, i.e.,  $tR(x, y)$ . If the media yield a phase hologram it is assumed that the transmission is given as

$$t = ke^{jkR(x, y)} \approx K(1 + jkR(x, y)) \quad (5-3)$$

which is based on a simple paraxial treatment of a thin phase hologram with small phase deviation justifying the resulting approximation to the exponential. In either case (amplitude or phase), the information-carrying term in the resulting transmission function for the hologram is proportional to the medium's response  $R(x, y)$ .

If a standard Vander Lugt approach is used to fabricate a hologram for the Fourier transform of the matched filter function  $h(x, y)$ , then one can express the transmission of the hologram by the following (a modified version of the typical expression due to the presence of finite resolution of the medium (Ref 29)):

$$t(\hat{x}, \hat{y}) = r_o^{-2} + \frac{|H|^2}{\lambda^2 F^2} + \frac{r_o}{\lambda F} (He^{j2\pi\alpha\hat{y}})^* m + \frac{r_o}{\lambda F} (He^{-2\pi\alpha\hat{y}})^* m \quad (5-4)$$

where  $H(x, y)$  is the Fourier transform of  $h$  obtained at a wavelength with a lens of focal length  $f$ ,  $\alpha = \sin \theta / \lambda$  with  $\theta$  the offset angle between the reference and image beams used in the recording process, and  $\hat{x} = f_x \lambda f$ ,  $\hat{y} = f_y \lambda f$  are the physical spatial variables expressed in terms of the Fourier transform frequencies  $f_x$  and  $f_y$ . If the hologram is played back with a beam that is modulated by the image  $y(x, y)$ , then the portions of the inverse transformed output that corresponds to the correlations between  $g$  and  $h$  are given by

$$\begin{aligned} & F^{-1}\{G(\hat{x}, \hat{y})[\bar{H}(\hat{x}, \hat{y})e^{-j2\pi\alpha\hat{y}} * m(\hat{x}, \hat{y})]\} \\ &= F^{-1}\{e^{-j2\pi\alpha\hat{y}} G(x, y)[\bar{H}^*(e^{j2\pi\alpha\hat{y}} m)]\} \\ &= g(x, y) * [h(-x, -y)M(x, y + \alpha\lambda f)] \end{aligned} \quad (5-5)$$

where  $x, y$  are the spatial coordinates in the output correlation plane with origin taken at 0 and  $\alpha \lambda f$  relative to the optic axis of the inverse transform lens.

In order to achieve the desired matched filter operation, the output should be  $g^*h(-x, -y)$ , but, due to the finite resolution capability of the recording medium, it is modified by the presence of the MTF function ( $M$ ). If we assume that  $M$  is in the form of a low-pass filter with nominal bandwidth  $B_m$ , then, in order to avoid excessive alterations of the matched filter weighting function, it is necessary that  $\alpha < B_m$ , as is clear from Fig. 5-2 where we assume that the spatial extent of the matched filter  $h$  is small compared to the recording process bandwidth.

It has been tacitly assumed that the reconstruction of the correlation plane is achieved without distortion, and the well-known constraint on the reference beam angle  $\theta_R$  necessary to avoid overlap with the dc spot requires that

$$\alpha \lambda F > [3 W_h + 2 W_g] \quad (\text{Ref 29})$$

where  $W_h$  and  $W_g$  are the spatial width of the matched filter image  $h$ , and the input image  $g$ . Combining this restriction with the previous one (that avoids distortion due to medium resolution) leads to the inequality  $B_m \lambda f > \alpha \lambda f > 3/2 W_h + W_g$ .

Now the spatial width of  $h$  is inversely proportional to the nominal bandwidth of the matched filter, i.e.,  $W_h = 1/B_n$  where  $B_n$  is the matched filter bandwidth. In the optical system, the matched filter bandwidth  $B_h$  corresponds to a physical dimension  $d = B_h \lambda f = \lambda f / W_h$ . In general, only a portion of the entire spectrum of the matched filter is recorded in the holographic system. If it is assumed that it is necessary to record a total matched filter spectrum that is  $K$  times its nominal bandwidth, then this would require a linear dimension in the hologram transform plane given by  $2kd = 2k \lambda f / W_h$ , which implies that the number of matched filters that could be stored per unit area (without multiple overlapping techniques) is given by  $(1/2kd)^2 = (W_h/2k \lambda f)^2$ . The effect of the recording media now becomes apparent since the previously derived inequality implies that

$$\frac{W_h}{2\lambda f} < \frac{B_m}{3 + 2 W_g/W_h}$$

and when combined with the expression for the number of filters per unit area this leads to

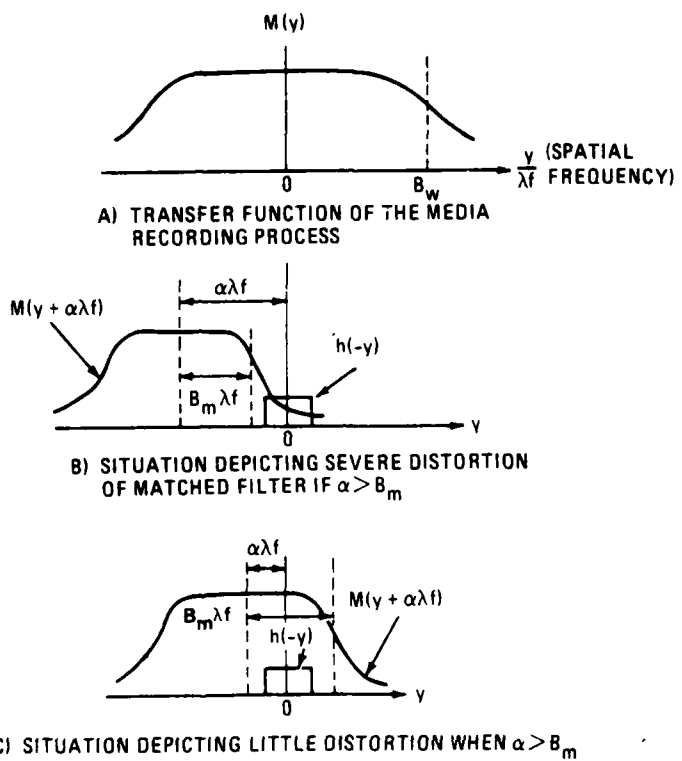


Fig. 5-2 Effect of Finite Resolution of Media on Matched Filter Weighting Function  $h$

1283-81-053(T)

$$\text{Number of matched filters per unit area} < \left[ \frac{B_m}{K(3+2W_g/W_h)} \right]^2$$

where  $B_m$  is the bandwidth of the recording medium, and  $K$  is the number of "matched filter bandwidths" that are to be stored in the memory plane.  $W_g$  is the spatial length of the input image (or aperture size) and  $W_h$  is the length of the matched filter image. As an example we take  $B_m = 1000$  cycles/mm and  $K = 4$  to yield the number of matched filters per unit area  $< \frac{10^4}{\frac{mm}{2}}^2$  equal  $10^6$  MF/cm<sup>2</sup> when  $W_g/W_h << \frac{3}{2}$  or  $10^4$  MF/cm<sup>2</sup> if  $W_g = 10W_h$  (MF image size 1/10 of the size of the aperture).

## 6 - SUMMARY

It has been demonstrated that large optical memories for correlator applications can be achieved using various techniques for storing the spectral signature, such as geometrical packing, split spectrum, coherent and noncoherent addition, and multiplexed carriers. Furthermore, in one memory position, sufficient memory elements can be stored to cover all orientation angles of the representative M-60 tank target for one to two range bins. Acceptable S/C ratios,  $\gtrsim 5$  dB, have been experienced under these conditions. Using realistic values for focal length and wavelength, 166 matched filters could be stored on a single filter basis. The use of any of the efficient storage techniques should increase this number by a factor between 1.16 and 30. However, as the number of memory elements increases, the laser energy output per element decreases for a fixed input power level.

To increase the efficiency of recording and the possibility of large memories, silver halide, dichromated gelatin and photo polymers were investigated.

Silver halide was an extensively used and well-known quantity in the program, and often compared with dichromated gelatin.

DCG proved to be a highly efficient, 68.9%, low-noise medium for recording matched filters. When tested with terrain scenes, S/C ratios ranged from 5 to 12 dB depending upon the particular terrain scene used and the size of the memory element. DCG is susceptible to relative humidity ( $>50\%$ ) and must be otherwise preserved, usually by sealing a cover plate on it. This technique was used.

Photo polymers recording is noisy and inefficient, and requires additional advances in technology before the matched filter performance is acceptable. Therefore, DCG as a medium for optical correlator memories is recommended.

The multiplexed carrier technique has been successfully used with the semi-thick ( $\sim 15\mu\text{m}$ ) dichromated gelatin recording medium. Thirty memory elements were stored in one position with a 5.3 and 6.0 dB S/C ratio for each of the carriers.

The matched filter can be viewed as a "chirp" grating whose performance is dependent upon the size of the memory element. As the number of coherently added images to make a matched filter increases, the low frequency region of the filter is saturated. The MF acts as a high pass filter. This feature probably accounts for the favorable discriminating nature of large coherent arrays. By contrast, noncoherently added MF have a frequency response of a single image MF.

Noncoherent additions up to five and coherent additions up to 15 have been successfully demonstrated but are not the upper limits of each technique. Rather, program and time constraints limited explorations beyond these values. There are indications however, that the limits are not much higher.

The translational sensitivity of large memory elements (e.g., 5x, 10x) is comparable to that of a single MF. Thus, for system considerations, no greater locational tolerance needs other than usual are introduced. Target azimuthal response shows that the thin MF media ( $\sim 6 \mu\text{m}$ ) have broad correlation responses and lower efficiencies than the more sharply tuned semithick media ( $\sim 15 \mu\text{m}$ ). Further analyses show that, when thicker media ( $\sim 25 \mu\text{m}$ ) are used, greater efficiencies should result.

Successful use of a computer model has been accomplished in the program. This has enabled a number of extended analyses to be performed in a more timely, practical manner. For example, multiple target-in-terrain situations can be readily simulated and analyzed in this manner. Also, some detailed examinations of matched filter geometries can be performed in a consistent, repeatable manner. Figure 6-1 illustrates a digital version of a multiple image coherent array MF in which the low frequency cutoff has been accurately established. The impulse response of the filter is also shown.

A significant advantage of an optical processor over alternate means is size. To illustrate compactness, a demonstration system was put together with existing correlator elements from bench components. This consolidated "system" was assembled and tested. A  $2 \times 2$  multiple holographic lens was used to fabricate the corresponding  $2 \times 2$  array of matched filters, which were two 5x and two 1x MF. The correlation plane and the MF array are shown in Fig. 6-2. The southeast Asian scene (Fig. 1-3a) was the object input film. A S/C ratio of 7 dB was obtained from the unit.

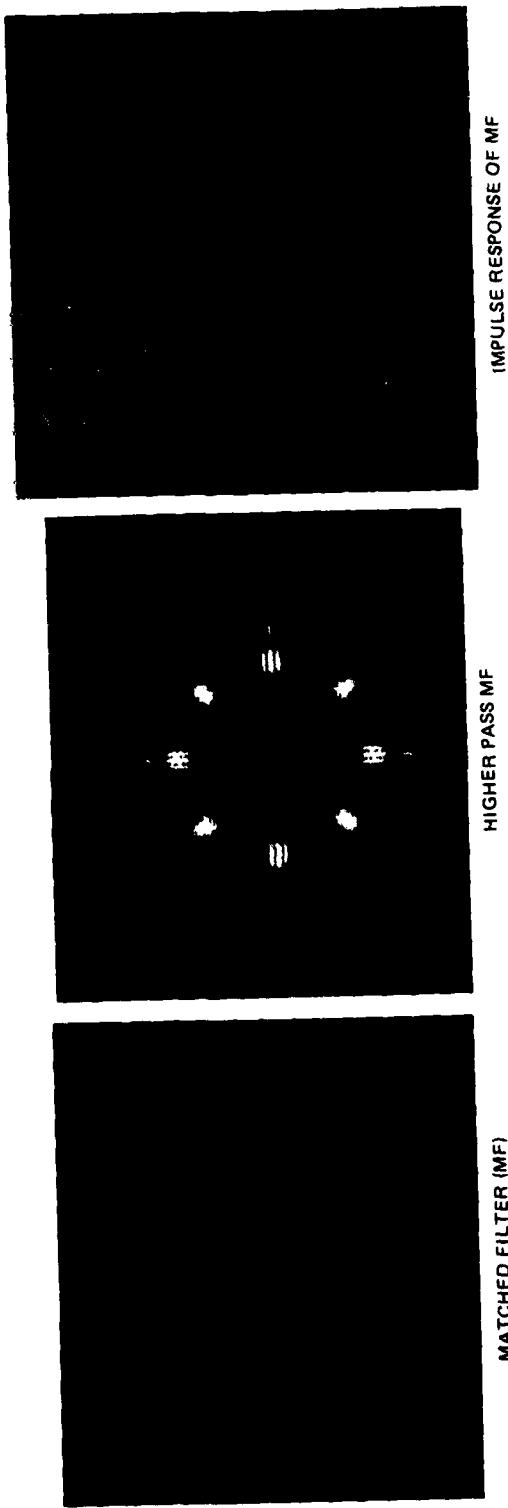
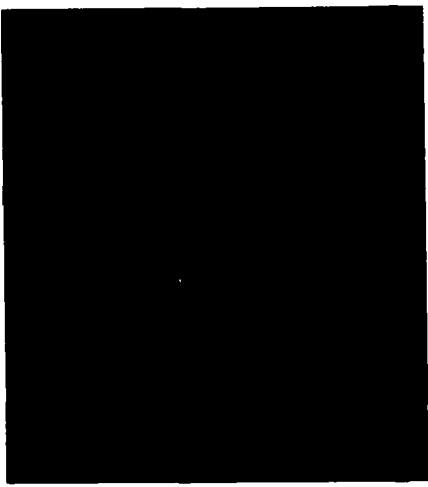


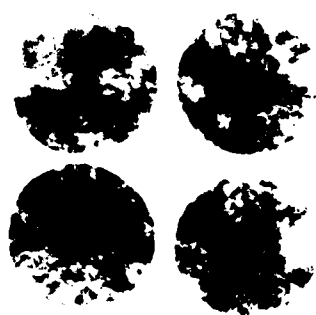
Fig. 6-1 Digital Version of Multiple Array Matched Filter (MFM)

1283-81-054(T)



(a) AT REDUCED THRESHOLD

1283-81-055(T)



(b) PHOTO OF 2x2 MF ARRAY

**Fig. 6-2 2x2 Array & Correlation Results**

Finally, in Fig. 6-3 we have tabulated various factors that can influence optical memory systems for correlator applications. The list is general in nature. Its purpose is to summarize our experience and design considerations throughout the course of this program.

I GENERAL	II CONSTRUCTIONAL
<ul style="list-style-type: none"> <li>• MODE: WRITE</li> <li>    WRITE, READ</li> <li>    WRITE, READ, ERASE</li> </ul>	<ul style="list-style-type: none"> <li>• RECORDING SPEED</li> <li>• DYNAMIC RANGE</li> <li>• DAMAGE THRESHOLD</li> <li>• SIZE</li> <li>• POTENTIAL FOR REPLICATION</li> <li>• WRITING ENERGY</li> <li>• POSITIONAL ACCURACY</li> <li>• ABILITY TO RECYCLE</li> <li>• ABILITY TO ADD-ON</li> <li>• DEFECT-FREE</li> </ul>
• CAPACITY	
• PACKING DENSITY	
• COST	
• PROCESSING NEEDS	
III ENVIRONMENTAL	IV OPERATIONAL & PERFORMANCE
<ul style="list-style-type: none"> <li>• SHELF LIFE</li> <li>• STABILITY</li> <li>• INTEGRITY</li> <li>• ARCHIVAL LIFETIME</li> <li>• TEMPERATURE RANGE OF OPERATION/STORAGE</li> <li>• SHOCK, VIBRATIONAL SURVIVABILITY</li> </ul>	<ul style="list-style-type: none"> <li>• ACCESS TIME</li> <li>• RESOLUTION</li> <li>• SENSITIVITY</li> <li>• LINEARITY ACROSS FIELD</li> <li>• DIFFRACTION EFFICIENCY</li> <li>• S/C OR S/N RATIO</li> <li>• SPATIAL FREQUENCY BANDWIDTH</li> </ul>
1283-81-056(T)	

Fig. 6-3 Optical Memory Requirements

## 7 - REFERENCES

1. K. G. Leib, et al., "Investigation of Large Capacity Optical Memories for Correlator Applications," Int Rep Contract F 49620-78-C-0051, USAF-OSR, May 1979.
2. Kenneth G. Leib, et al., "Aerial Reconnaissance Film Screening Using Optical Matched-Filter Image-Correlator Technology," App Opt, 17, 15 Sept 1978, p 2892.
3. U.S. Patent 3 779 492 Grumman Aerospace Corporation.
4. C. Warde and A. D. Fisher, "Microchannel Optical Light Modulator as a Storage Medium," Proc SPIE, 177, "Optical Information Storage," Washington, DC, April 1979.
5. P. O. Braatz, et al., "Advanced Light Modulator," Final Report Contract F33615-79-C-1748, AFWAL-TR-80-1214, Feb 1981.
6. T. Saito, et al., "Microscopic Response in Thermoplastic-Photoconductor Media (Edge Effect)," J Optics, (Paris) 9, 73 - 78, 1978.
7. K. G. Leib, et al., "Optical Matched Filtering Techniques for Automatic Interrogation of Aerial Reconnaissance Film," FR Contract DAAG 53-75-C-0199, USA-NVL, Sept 1976.
8. K. G. Leib, et al., "Baseline Test of a Matched Filter Correlator for Screening Aerial Reconnaissance Film," Grumman Research Report RE-540, May 1977.
9. D. A. Ansley, et al., "Analysis of the Effect of Nonlinear Amplitude Response of the Matched Filter on the Magnitude and Shape of the Correlation," AGARD Conference Proceedings No. 50, Oct 1969.
10. A. C. Livanos, et al., "Fabrication of Grating Structures with Variable Period." Opt Comm, Vol 20, No. 1, pp 179 - 182, Jan 1977.
11. G. Goldman, "Spatial Frequency Multiplexing for High Density Holographic Data Storage," Optik, I:45, pp 473 - 488, II:46, pp 1 - 17, 1976.

12. S. P. Almeida and J. K-T. E, "Water Pollution Monitoring Using Matched Spatial Filters," App Opt, 15, No. 2, Feb 1976.
13. P. C. Mehta, "On the Recording of Single Exposure Multiplexed Hologram," Nouv Rev Opt, 7, No. 2, pp 101 - 104, 1976.
14. H. Kogelnik, "Coupled Wave Theory for Thick Hologram Gratings," BSTJ 48, pp 2909 - 2947, Nov 1969.
15. W. R. Klein, "Theoretical Efficiency of Bragg Devices," Proc IEEE, Vol 27, p 467, May 1966.
16. M. G. Moharam, et al., "Criteria for Bragg Regime Diffraction by Phase Gratings," Opt Comm, 32, pp 14 - 18, Jan 1980.
17. T. Kubota, "Characteristics of Thick Hologram Grating Recorded in Absorptive Media," Optica Acta, 25, pp 1035 - 1053, 1978.
18. B. J. Chang and C. D. Leonard, "Dichromated Gelatin for the Fabrication of Holographic Optical Elements," Appl Opt, 15 July 1979.
19. A. Graube, "Holographic Optical Element Materials Research," Final Report Contract F44620-76-C-0064, Nov 1978.
20. B. J. Chang, "Dichromated Gelatin as a Holographic Storage Medium," Proc SPIE, 177, Optical Information Storage, Washington, DC, April 1979.
21. R. Kowarschik, "Diffraction Efficiency of Sequentially Stored Gratings in Transmission Volume Holograms," Optica Acta, 25, 67 - 81, 1978.
22. M. Lang, et al., "A Contribution to the Comparison of Single Exposure and Multiple Exposure Storage Holograms," Appl Opt 10, pp 168 - 173, Jan 1971.
23. R. Alferness and S. K. Case, "Coupling in Doubly Exposed, Thick Holographic Gratings," J Opt Soc Am., 65, No. 6, pp 730 - 739, June 1975.
24. G. Hesse, et al., "Volume Holograms as Frequency-Selective Elements," Opt and QE, 11, pp 87 - 96, 1979.
25. R. Magnussen and T. K. Gaylord, "Analysis of Multiwave Diffraction of Thick Gratings," J Opt Soc Am., 67, No. 9, pp 1165 - 1170, Sept 1977.
26. B. L. Booth, "Photopolymer Material for Holography," Appl Opt, 14, pp 593 - 601, March 1975.

27. A. A. Friesem, "Photodielectric Polymer for Holographic Recording," Appl Opt, 16, pp 427 - 432, Feb 1977.
28. "Sensitized Material for Realtime Holographic Recording," NRC Data Sheet, July 1974.
29. J. W. Goodman, Introduction to Fourier Optics, McGraw-Hill, New York, 173, (1968).
30. K. G. Leib and J. Mendelsohn, "Validation of a Digital Simulation of an Optical Matched Filter Correlator Applied to Aerial Reconnaissance," S.P.I.E. 25th Annual Symposium, San Diego, CA, August 1981.

## 8 - PROFESSIONAL ACTIVITIES

During the program, the participants were involved in the following activities and/or publication efforts as a result of this AFOSR sponsored program.

### 8.1 PUBLICATIONS AND PRESENTATIONS

1. "Validation of a Digital Simulation of an Optical Matched Filter Correlator Applied to Aerial Reconnaissance," K.G. Leib and J. Mendelsohn, SPIE 25th Annual International Technical Symposium and Exhibit, San Diego, CA August 1981.
2. "Investigation of Large Capacity Optical Memories for Correlator Applications," K.G. Leib and J. Mendelsohn, invited paper CLEO, June 1981.
3. "Multichannel Holographic Lenses for Correlator Use," R. Bondurant, Electro-Optics Laser '80, Boston, MA November 1980.
4. "Large Optical Memories," K.G. Leib, Physics Department Seminar, Adelphi University, October 1980.
5. "Optical MF Correlator Memory Techniques and Storage Capacity," K.G. Leib and R. Bondurant, Optical Engineering, May-June 1980.
6. "Construction of Multi-Capacity Matched Filters Using Birefringent Object Film," R. Bondurant and K.G. Leib, Applied Optics, 15 April 1980.
7. "Digital Method in the Design of Optical Matched Filters," J. Mendelsohn and M.R. Wohlers, SPIE Conference on Devices and Systems for Optical Signal Processing, Los Angeles, CA, February 1980.
8. "Target Detection Using Hybrid Digital-Analog Correlation Techniques," presented at the US Army Missile R&D Command Workshop on "Imaging Trackers and Autonomous Acquisition Applications for Missile Guidance," M.R. Wohlers and Jay Mendelsohn, November 1979.

9. "Digital Analysis of the Effects of Terrain Clutter on the Performance of Matched Filters for Target Identification and Location," J. Mendelsohn, M.R. Wohlers and K.G. Leib, SPIE Conference of Digital Processing of Aerial Image, May 1979, Huntsville, AL.
10. "Optical Information Storage," seminar initiated by Principal Investigator who is also Chairman, Technical Committee, SPIE Conference, Washington, D.C., April 1979.
11. "Optical Matched Filter Correlator Memory Techniques and Storage Capacity," SPIE Conference '79 East, Washington, D.C., April 1979.
12. "Analysis of an Optical Matched Filter Guidance System for Tactical Homing Applications," AIAA/NASA Conference on "Smart Sensors" NASA Langley Research Center, 14-16 November 1979.

#### 8.2 ACTIVITIES

1. Minicourse "Micro-optics," CLEO Washington D.C., June 1981 (K.G. Leib and B.J. Pernick).
2. Minicourse "Optical Processing," SPIE San Diego, CA, July 1980 K.G. Leib.
3. Committee Participant, SPIE Technical Symposium, "Image Processing for Missile Guidance," San Diego, CA, July 1980 (K.G. Leib).
4. Session Chairman, SPIE Technical Symposium '79 East, Washington, D.C., April 1979 (M.R. Wohlers).
5. Minicourse, "Optical Information Storage," SPIE, April 1979 (K.G. Leib and B.J. Pernick).
6. Chairman, Technical Committee, "Optical Information Storage," SPIE, Washington, D.C., April 1979 (K.G. Leib).

#### 8.3 RELATED CONSULTATIVE EFFORTS

1. "Optical Correlator Memory for a Terminal Homing Missile Scenario Against a Complex Target," Grumman Research Department Memorandum RM-660, August 1978. (This was not conducted under OSR sponsorship but was a consultant effort to a related DoD ARPA contract).

2. "Digital Methods in the Design of Optical MF for Target Recognition," J. Mendelsohn and M.R. Wohlers, USA-MICOM Workshop on Imaging Trackers and Autonomous Acquisition Application for Missile Guidance, Huntsville, AL, November 1979 (consultation on a DoD-ARPA contract).
3. "High Accuracy Cruise Missile Terminal Guidance System," G. Calderone, et al., FR Contract DAAK-40-77-C-0089, Mod P00004, December 1979 (Portions of this report were based on the OSR contract under DoD-ARPA contract).

#### **8.4 PATENT DISCLOSURE**

1. "Optical Memory Production Control System," Patent disclosure filed with Grumman Legal Department, K.G. Leib, 12 September 1978.

## **9 - PERSONNEL**

The program was conducted under the direction of Kenneth G. Leib, Staff Scientist, who was responsible for the scientific and fiscal success of the investigation. He was assisted principally by Jay Mendelsohn, Senior Staff Scientist.

This program, like most, depended upon the contributions of others for its success. The authors wish to thank M. Ronald Wohlers for his many discussions and technical assistance during the program. We also acknowledge the contributions of:

**Robert Bondurant  
Dr. Richard E. Kopp  
Suey Jue  
Dr. Benjamin J. Pernick**

## APPENDIX A

### USE OF DICHROMATED GELATIN FOR MATCHED FILTERS

The use of dichromates as light sensitive activators of organic matters dates back to about 1830 (Ref 1, 2). Although old, it has in the last 10 years been suggested and examined as a holographic medium (Ref 3, 4) and applied to such applications as heads-up displays (Ref 5). Interest in this medium for large capacity optical memory stems from its potential advantages in recording efficient matched filters. It has large modulation capability, essential when overlapped filters are required. Since the mechanism is molecular in nature, it is not bound by the spatial frequency limiting aspects of silver halide grain size, and thus, as a medium it may enable the limits on some parameters to be utilized. The molecular nature of the dichromated gelatin also suggests low scattering and thus, the potential for phase type matched filters is there without the inherent reduction in S/C ratio when photographic emulsions are bleached.

Although there are many advantages, the dichromated gelatin recording medium suffers two drawbacks, neither insurmountable. First, the material has about 1/10 the sensitivity of slow photographic emulsions and requires a blue excitation (unless otherwise dyed and hardened as described in Ref 6, 7). Secondly, the material like bromine bleached photographic emulsions is susceptible to degradation due to high relative humidity. This is surmountable by environmental control or the use of an optical quality cover plate.

The hardening process is a complex chemical reaction which after many years is still not entirely understood\*, a situation not surprising when one considers the organic and variable origins of the gelatin. In the current program it is not essential that the process be understood or further unraveled but rather that a consistency be maintained so that at least the process can be duplicated in terms of holographic formation. Our other objective in examining this medium is to determine whether the phenomenology of surface relief inherent to the medium does in anyway, advance the capability for large capacity memories.

-----

\*An excellent recent study (Ref 8) has been conducted in which through parametric control, the mechanisms arising in the dichromated gelatin process are explored in depth.

The undoped dichromated gelatins have high absorptivity to blue and  $\mu$ v radiation and negligible absorption to the red. This prescribes argon or helium-cadmium lasers for fabrication although playback can be at any wavelength with appropriate compensations. The indices of refraction as given by Shankoff (Ref 4) are as follows

Basic Gelatin	$N = 1.5426 \pm 0.0001$
Gel + A Dich	$N = 1.5486$
Gel + A Dich + Exp.	$N = 1.5572$
Gel + A Dich + Exp.	$N = 1.5515$
+ Dev.	
Gel + A Dich + Unexp	$N = 1.5488$
+ Dev.	

From these, we can see that when properly processed holograms should have a differential in index

$$N \sim 1.5515 - 1.5150$$

$$= 0.037 \pm 0.005$$

with the uncertainty arising from the tolerance in the glass index.

In carrying out the empirical aspects of the program dealing with the phenomenology of materials, it was decided that with regard to dichromated gelatin, commercial sources would be employed. It was believed that the consistency of base materials would be superior to that which could be otherwise immediately achieved.

A large number of base gelatins are available but those generally of interest to other aspects of the program are the Eastman-Kodak 649F and 120-02. Discussions with E-K\* indicated that the emulsions have various initial degrees of hardness when made available as silver halide emulsions. In decreasing states of hardness they are 120-02 and 649F with thickness typically 6 and 17  $\mu$ m, respectively. After fixing however, there is a significant reduction in thickness which depends upon the silver halide "doping" that is typically 25%. Thus, for the same state of humidity, one might expect final thicknesses to be 4.5 and 13.5  $\mu$ m, respectively.

-----  
\*Eastman-Kodak, R. Anwyl, Sales Representative

## PROCESSING

There are many processing combinations both for preparation and development (e.g., Ref 9-12, 5) which appear to work. For the present program, the primary concern is not a general formulation but one which specifically influences the creation of an optical matched filter memory. On this basis, only a few steps were examined which might prove vital to matched filter (MF) performance. The first of these steps is the pre-doping fix where the use of Eastman Kodak standard mixtures were used on one of the plate types previously cited. In one set of plates, the hardener was omitted; in the other it was included. The prepared plates were used to fabricate MF's which were single and then 5x noncoherent overlays. Upon playback the results clearly show that 649F emulsion film ought not be pre-hardened. This can be seen in Table A-1 where in both types of MF's, the autocorrelation signal is decisively less in the prehardened case. Based upon these results, plate preparation processing thereafter eliminated prehardening so that the procedure consistently used throughout the program was that given in Table A-2.

In studying references concerned with processing, it was decided that at least some examination of the developing procedures was also in order if for no other reason than that a standard be followed. Development was narrowed down to a choice between the more simple approach of Chang (Ref 13 and 14) and others, or the more recent but more involved technique of Graube (Ref 8). The procedure adapted to local conditions is given in Table A-3.

Since it was indicated in the literature that the time history of the dichromated gelatin was an important influence on the generated gelatin quality, two tests were established to determine the influence upon matched filters. In one, the time history after removal from the alcohol wash was determined and in the second, the efficiency of gratings made at various times after emulsion doping, were made. Exposures in the latter followed the Fibonacci series, 1, 1, 2, 3, 5, 8, 13, 21, 34, ...., after the first one. These exposures were arrived at after a study of earlier efficiency results where in neither binary nor linear distributions in exposure time seemed adequate.

The results of the first test are shown in Fig. A-1 and show the time history starting with the removal of the dichromated gelatin plate from the final (100%) alcohol wash. In another case a plate was washed twice as long as that plate whose results are shown in Fig. A-1. This concern arose because of the need to delay final alcohol dry on the one plate until the test on the other was complete. The results show that the two plates, otherwise similarly processed, are the same. Degradation of a filter was also

**TABLE A-1 EFFECT OF PREHARDENING UPON C<sub>N</sub> IN 649F-BASED  
AMMONIUM DICHROMATED GELATIN FILM**

STATE	0°	ORIENTATION				INCOHERENT OVERLAY
		18°	36°	54°	72°	
UNHDN	1.00					1X
UNHDN	0.816	0.785	0.140	0.433	1.204	5X
HDN	0.335					1X
HDN	0.224	0.032	0.029	0.252	0.064	5X
1283-009(a)(T)						

**TABLE A-2 PREPARATION OF DICHROMATED GELATIN EMULSIONS  
FROM E-K 120-02 AND 649F-BASED FILMS**

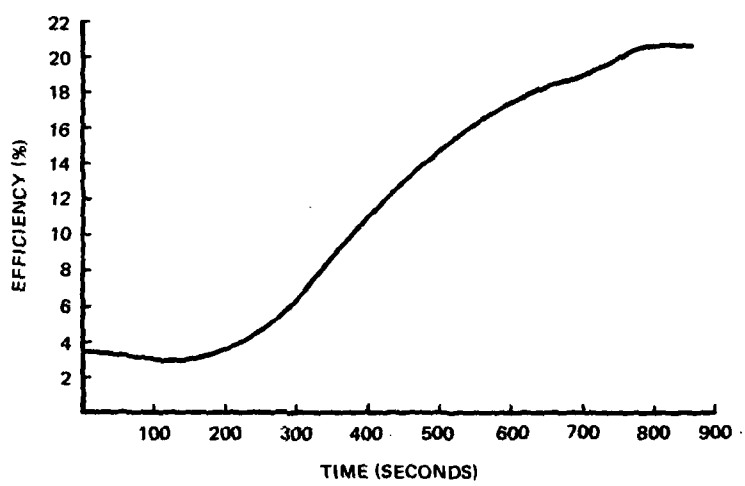
- 1. GENERAL**
  - A) USE CHEMICALS WHICH HAVE BEEN AT T = 20-21°C FOR 24 HOURS
  - B) DISPOSE OF ALL CHEMICALS IN ACCORDANCE WITH ESTABLISHED ENVIRONMENTAL CONTROL PROCEDURES
  - C) PLATE EXPOSURE SHOULD BE AT RH < 50%
- 2. FIX WITHOUT HARDENER**
  - A) STANDARD EASTMAN-KODAK MIX
  - B) FOR 10 MINUTES IN THE DARK
  - C) AGITATE FOR 10 SECONDS ONCE PER MINUTE
- 3. WASH IN RUNNING DEIONIZED WATER**
  - A) FOR 10 MINUTES
- 4. FLUSH WITH PHOTO-FLO**
  - A) FOR 30 SECONDS
- 5. DRY IN DUST FREE ENVIRONMENT**
  - A) FOR ABOUT 15 HOURS AT ROOM TEMPERATURE (~ 20° C)
  - B) IN RH 20% - 30% (E.G., DRIED COMPRESSED AIR ATMOSPHERE)
- 6. IDENTIFY GELATIN SIDE BY NUMBERING PLATES IN CORNER**
- 7. SOAK IN 5% AMMONIUM DICHROMATE SOLUTION**
  - A) FOR 10 MINUTES IN THE DARK
  - B) AGITATE 10 SECONDS ONCE PER MINUTE
- 8. USE LENS TISSUE TO WIPE NON-EMULSION SIDE CLEAR OF EXCESS DICHROMATE. WIPE DRY**
- 9. DRY AS IN STEP 5**
  - A) VERTICALLY ORIENTED
  - B) KEEP IN DARK UNTIL DEVELOPED
  - C) USE WITHIN 5 DAYS

1283-010(a)(T)

**TABLE A-3 DEVELOPMENT OF DICHROMATED GELATIN PLATES**

1. ESTABLISH SYSTEM CONDITIONS FOR FRINGE VISIBILITY, ORIENTATION, ETC.
  - A) EXPOSE
  - B) KEEP IN DARK AFTER EXPOSURE
2. DEVELOPMENT
  - A) IN 0.5% AMMONIUM DICHROMATE SOLUTION
  - B) FOR 5 MINUTES IN RED LIGHT OR DARK
  - C) AGITATE FOR 10 SECONDS EVERY MINUTE
3. FIX
  - A) IN STANDARD EASTMAN-KODAK FIXER WITH HARDENER
  - B) IN RED LIGHT FOR 5 MINUTES
4. WASH
  - A) IN RUNNING DEIONIZED WATER
  - B) FOR 10 MINUTES (CAN BE IN ROOM LIGHTING IF OTHER CONDITIONS PERMIT)
5. WASH
  - A) IN PHOTO-FLO FOR 30 SECONDS
6. WASH
  - A) IN DEIONIZED WATER FOR 2 MINUTES
7. DEHYDRATE
  - A) FOR 3 MINUTES IN 50/50 ISOPROPANOL/WATER MIX
8. DEHYDRATE
  - A) FOR 3 MINUTES IN 100% ISOPROPANOL
9. DRY
  - A) FOR 15 HOURS AT ROOM TEMPERATURE (20°C)
  - B) IN DUST FREE AREA AT RH 20% - 30%

1283-014(a)(T)



1283-001(a)(T)

Fig. A-1 Efficiency of Grating in DCG as a Function of Time After Final Alcohol Wash

considered. We established an acceptable performance in efficiency for a plane grating and then retained that grating in a humid atmosphere during its test life. The RH was  $67\% \pm 3\%$ . Efficiency was periodically measured until the efficiency remained constant. The results are shown in Fig. A-2. It should be pointed out that the test on the grating was initiated immediately after the grating was removed from a 20% RH storage area.

Individual gratings were made at various times after the plates were doped, and the efficiency measured at the indicated times. The start times followed the Fibonacci sequence given above. It appears that within reasonable variation the efficiency remains relatively constant at the value it initially had after processing. In order to sort out the vertical distribution better, the best plate of the two plates at each initial start time was used, and efficiency plotted as a function of Time after Doping. The basis for this choice was that the "best of the two plates" would be closer to the maximum capability at the given "age." With this rational we have the results of Fig. A-3. It would appear that there are some times that are more optimum than others with one clear choice - immediate exposure.

The qualification on the thickness of the medium as it influences efficiency and the readout from storage is discussed earlier. In that section and its references it has been shown that thickness is a significant factor which influences efficiency. One direct empirical way to determine the influence of thickness is through an efficiency measurement as the grating in question is azimuthally rotated.

This was done with the two plane gratings whose results are shown in Fig. A-4 for thick and thin representatives, respectively. As a reminder, these were fabricated from 120-02 and 649F based plates. In conducting this assessment, the two wavelengths 6328 and 4880 were used. Also, the efficiency was determined by scanning from 15 degrees on one side of the beam - plate normal condition to an equal angle on the other side with an additional precision used near plate normality.

At the fabrication wavelength ( $4880\text{\AA}$ ) the azimuthal sensitivity is  $\pm 4.5$  degrees (and  $\pm 4.8^\circ$  for  $\lambda = 6328\text{\AA}$ ) for the thick plate and essentially independent of rotation in the thin case. Part of the "skirt" drop off can be attributed to the beginning of vignetting by the test beam.

Figure A-5a shows a phase contrast photograph of a 5x non-coherently added MF illustrating the surface relief while Fig. A-5b illustrates the quality of a  $2.81 \mu\text{m}$  grating in the thick (649F based) DCG.

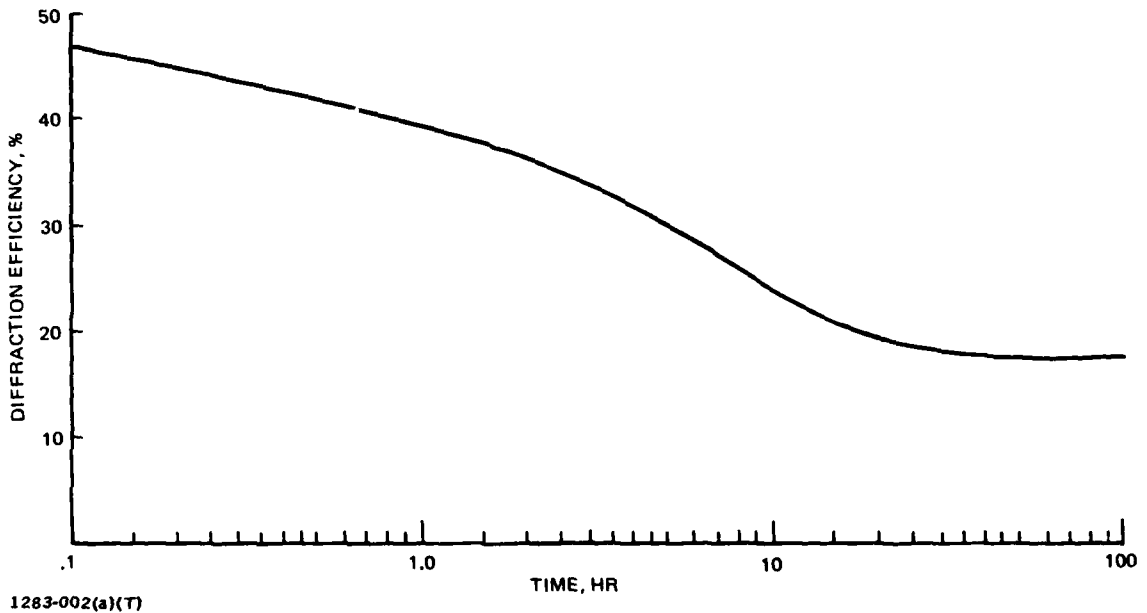
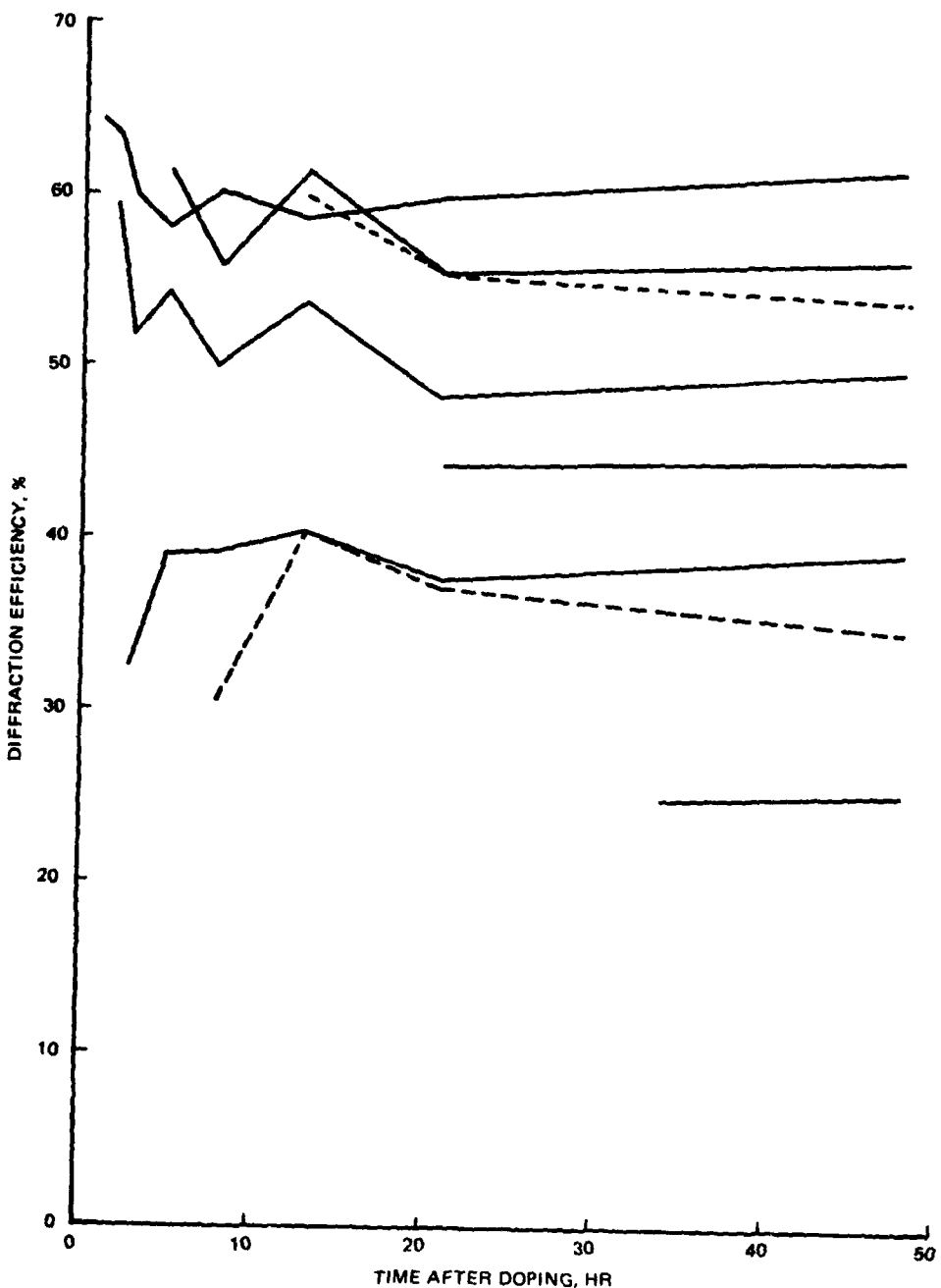


Fig. A-2 Degradation of a Dichromated Gelatin Grating in High RH Atmosphere



1283-003(a)(7)

**Fig. A-3 Efficiency of Grating ( $\nu = 356 \text{ mm}^{-1}$ ) in Dichromated Gelatin as Function of Time of Generation After Doping**

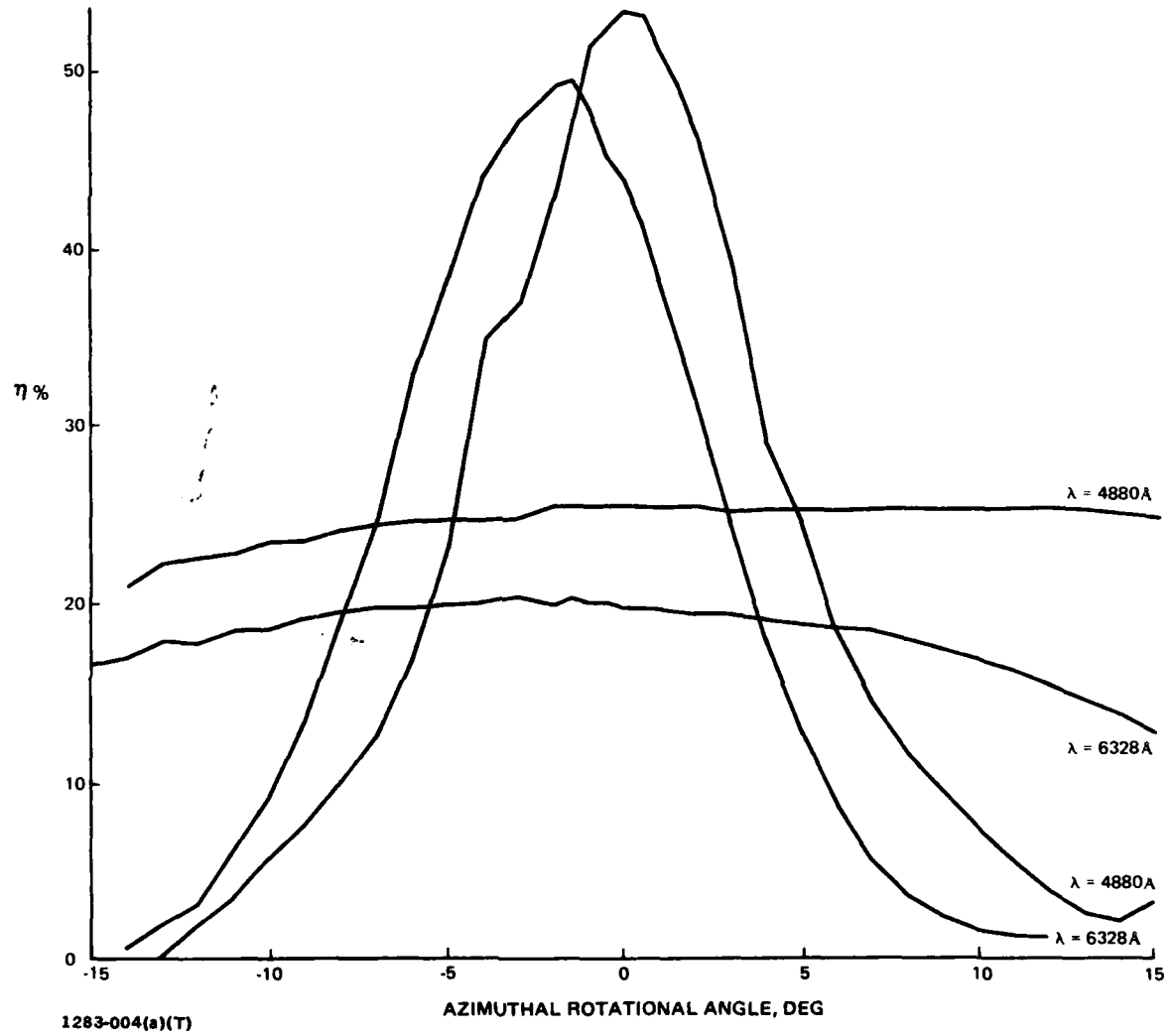
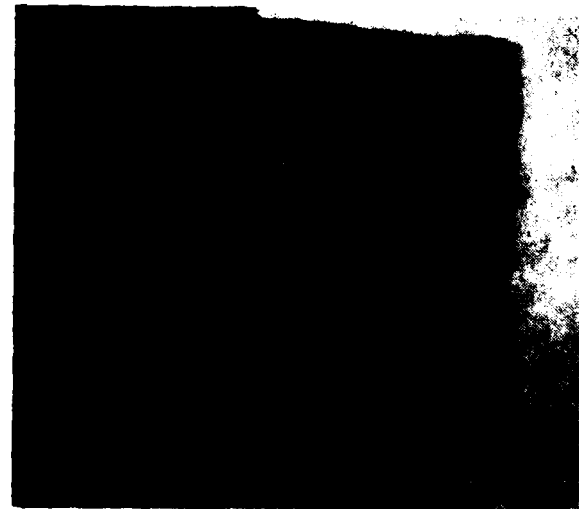


Fig. A-4 Response of Thin/Thick DCG Gratings to Azimuthal Rotation



(a) 5X NON-COH MF



(b) PLANE GRATING

1283-005(a)(T)

**Fig. A-5 Phase Relief Photograph of (a) 5X Non-Coherently added MF and (b) Plane Grating**

## REFERENCES FOR APPENDIX A

1. Kosar, J., Light Sensitive Systems, J. Wiley and Company, New York, (1965) Chapter 2.
2. Mees, C. E. and James, T. H., The Theory of the Photographic Process, MacMillan, New York (1966) Chapter 3.
3. Shankoff, T. A. and Curran R. K., "Efficient High Resolution Phase Diffraction Gratings," Appl. Phys. Let., 13, p. 239 (1968).
4. Shankoff, T. A., "Phase Holograms in Dichromated Gelatin," Appl. Opt., 7, p. 2101 (1968).
5. Colburn, W. and Chang, B., "Holographic Combiner for Heads Up Display," USAF-AFAL-TR 77-110, October 1977.
6. Graube, A., "Holograms Recorded with Red Light in Dye Sensitized Dichromated Gelatin," Opt. Comm., 8, July 1973, p. 251.
7. T. Kubota, et al., "Hologram Formation with Red Light in Methylene Blue Sensitized Dichromated Gelatin," Appl. Opt., 15, pp. 556-558, February 1976.
8. Graube, A., "Holographic Optical Element Materials Research," FR Contract F44620-76-C-0064, November 1978.
9. Meyerhofer, D., "Phase Holograms in Dichromated Gelatin," RCA Rev., 33, pp. 110-132 (1972).
10. Marcroft, D. A., "The Production of Dichromated Gelatin Emulsions for Recording Phase Holograms," Master's Thesis USAF Institute of Technology Dec. 1975, AD-A019320.
11. McCauley, D. G., et al., "Holographic Optical Element for Visual Display Applications," Appl. Opt., 12, pp. 232-242, Feb. 1973.
12. Basola, C. P. and F. Esposto, "Materiale Fotosensibile Ad Alta Efficienza Di Difrazione Per Registrazioni Olografiche," CSELT Rapporti Tecnici, Vol. V, Dicembre 1977, pp. 341-348.

13. Chang, M., "Dichromated Gelatin of Improved Optical Quality," *Appl. Opt.*, 10, p 2550-1 (1971).
14. Chang, B. J., "Post-processing of Developed Dichromated Gelatin Holograms," *Opt. Comm.*, 17, No. 3, (1976).

## APPENDIX B

### CONSTRUCTION OF MULTICAPACITY MATCHED FILTERS USING BIREFRINGENT OBJECT FILM

Fabrication of matched filters for a large capacity memory for correlator applications requires the use of an object film. The growing tendency in the field is toward polyester based film which is significantly more birefringent than the older acetate type. Thus, care must be exercised in using such film in the formation of matched filters, particularly when the same object is used and rotated in order to have 360° object coverage.

The paper in this appendix addresses this problem.

## Construction of multicapacity matched filters using birefringent object film

Robert A. Bondurant and Kenneth G. Leib

Target objects used to construct matched filters for correlator applications are generally recorded on photographic film. Most commercial emulsions of interest are coated on birefringent substrate. The authors address the effects of this birefringence upon the interference pattern recorded as a matched filter in coherent optical correlators. Results are then expanded to include several types of multiple matched filters. Finally, techniques are discussed that reduce the deleterious effects of input film birefringence.

In coherent optical correlators, a collimated laser beam illuminates a frame, or portion of an input film, which is the subject of the optical analysis. This film is usually located one focal length in front of a Fourier transforming lens, which performs the transform operation and superimposes the transform upon a stored Vander Lugt type of matched filter located in the back focal plane of the transform lens.<sup>1</sup> The signal emerging from the filter is the product of the incident and stored transfer functions.

Behind the matched filter, a second lens takes the inverse transform of the filter output and displays the squared modulus of this as the peak correlation signal if the film contains a target corresponding to the one stored. Otherwise, a general clutter signal is obtained.

Thus, the correlator has two basic operations: matched filter fabrication and correlation measurement. A matched filter is the product of signal and reference beam interference, thereby requiring similarly polarized waves.

Demonstration systems such as the Grumman-developed OMFIC<sup>2</sup> incorporate some means of increasing the system storage capacity to handle input scene variables.<sup>3</sup> In addition to the multiple channels of the multiple holographic lens-matched filter combination in the OMFIC, the capacity of a correlator can be increased by storing multiple image matched filters at each address. Such complex matched filters in which

images are added at various orientations in a coherent and noncoherent fashion are being investigated.<sup>4</sup> Coherent addition involves a multiple-target input image and one exposure to construct the matched filter, while noncoherent addition involves multiple exposures of one target at a time to construct the matched filter. Generally orientation is the parameter, and a single input image is rotated in an iso-optical gate between successive exposures for noncoherent addition. An example of multiple target imagery used for preparing coherent addition matched filters is shown in Fig. 1.

Photographic emulsions of input imagery for matched filter memories are generally prepared with polyester (polyethylene terephthalate) substrates as these are commonly used by the aerial reconnaissance community due to the high film footage per pound and dimensional stability possible. Molecular orientation in the polyester sheet gives rise to birefringence,<sup>5</sup> which affects the polarization of the signal beam in the correlator. This effect does not occur when cellulose acetate film base is used. However, acetate is used with decreasing frequency. Figure 2 shows the birefringence of several photographic films of interest as the signal (through an analyzer) vs film angle. The analyzer was rotated for minimum output with a vertically polarized laser input, and then the test film was inserted in front of the analyzer and rotated (0°: film is vertical).

From the experimental data in Fig. 2, the polyester based films have a fast axis advance  $\omega$  of 89.2–89.4° as

$$\omega = \tan^{-1} \frac{(\text{peak})}{(\text{null})}. \quad (1)$$

Calculated values of  $\omega$  were obtained from

$$\omega = [(2\pi)/\lambda](n_x - n_y)t \quad (2)$$

Thickness  $t$  is 0.103 mm for the polyester based films, and reported indices<sup>5</sup> are  $n_x = 1.66$  and  $n_y = 1.64$ . The

The authors are with Grumman Aerospace Corporation, Bethpage, New York 11714.

Received 22 October 1979.

0003-6935/80/081380-03\$00.50/0.

© 1980 Optical Society of America.

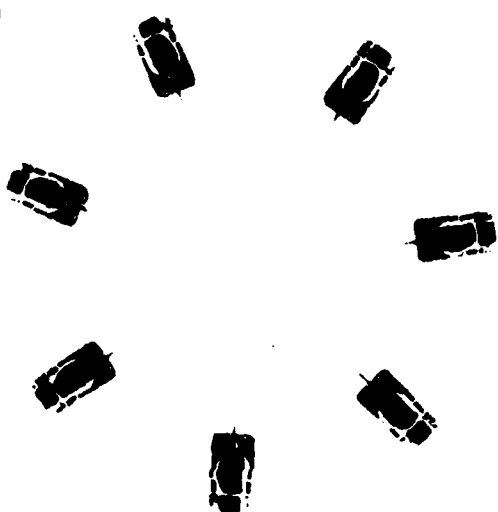


Fig. 1. Seven-target input image for coherent addition.

EASTMAN KODAK FILMS  
 A. 649F, polyester base  
 B. 50173, polyester base  
 C. 649F, acetate base  
 D. High contrast copy, acetate base

- Zero at bottom except "C" where it was shifted to separate curve from "D"
- Transmission difference account for peak height differences between A & B

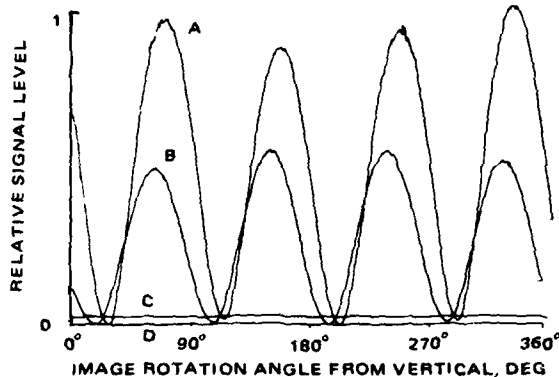


Fig. 2. Birefringence effects in commercial (Eastman Kodak) emulsions.

result is  $\omega = 91.9^\circ$  at 633 nm, and thus the experimental and calculated values for  $\omega$  are in close agreement.

Transmission differences at 633 nm between 649F and S0-173 films due to sensitizing dye differences account for the disparity between the two relative peak signals with polyester substrates shown in Fig. 2.

The impact of birefringence of the input emulsion on correlator performance is not significant in the playback mode,<sup>6</sup> and, with thin emulsion matched filters, all input films may be used unless polarization sensitive detection

equipment is used. Some effects may be noticed with thick emulsion matched filters due to grating sensitivity.

However, in fabricating matched filters, the phase information contained in the interferometric fringes comes from the reference and signal beam interference optimized for either contrast or fringe visibility. This optimization is done at the optical spatial frequency of interest, where the beams are set typically for a beam ratio of  $R = 1$ , where

$$R = \frac{\text{reference beam intensity}}{\text{signal beam intensity}}. \quad (3)$$

It is apparent that the spectra of targets of interest are highly variable in amplitude so that fringe visibility is usually optimized at a specified spatial frequency along one of the two orthogonal axes defining the optical spectrum.<sup>3</sup> The measure of the optimization of the similarly polarized interference of the signal beam  $I_S$  and reference beam  $I_R$  is the visibility function  $v$ , which for coherent beams becomes

$$v = (I_{\max} - I_{\min})/(I_{\max} + I_{\min}) \\ = 2(I_R I_S)^{1/2}/(I_R + I_S) = 2R^{1/2}/(1 + R). \quad (4)$$

The effect of the input film on the linearly polarized beam in the signal channel is dependent on the amount of retardation and orientation of the fast axis. The intensity of the beam emerging from the film plane that results from variations in the parameters can be derived. The result is that the signal intensity varies as

$$I_{\text{sig}} = (I_0/2) \left( \frac{1}{2} - \frac{1}{2} \cos 2\omega \cos 2\alpha \right), \quad (5)$$

where  $\omega$  is as before, and  $\alpha$  is the offset angle of the fast axis. When  $\omega = 0$  (linear polarization and  $\alpha = \pi/2$ ), the beams are coplanar and equal. The variations also become

$$I_{\text{sig}} = (I_0/2) \left( \frac{1}{2} - \frac{1}{2} \cos 2\alpha \right) = I_0 \sin^2 \alpha / 2, \quad (6)$$

which we can use to determine the visibility of fringes when one of two linearly polarized beams is rotated around the propagation axis. From Eqs. (3) and (4)

$$v_{21P} = \frac{2[(I_0/2)/(I_0 \sin^2 \alpha / 2)]^{1/2}}{1 + (I_0/2)/(I_0 \sin^2 \alpha / 2)} \\ = 2 \sin \alpha / (1 + \sin^2 \alpha). \quad (7)$$

In general, the visibility becomes

$$V = \frac{2 \left( \frac{1}{2} - \frac{1}{2} \cos 2\alpha \cos 2\omega \right)^{1/2}}{1 + \left( \frac{1}{2} - \frac{1}{2} \cos 2\alpha \cos 2\omega \right)}, \quad (8)$$

so that Eq. (7) is an upper bound on the fringe visibility for small values of  $\alpha$  only. Many combinations of  $\alpha$  and  $\omega$  are possible.

Not only is the fringe visibility affected by the rotation of one linearly polarized beam with respect to another, but the noninterfering part of the rotated signal beam becomes a biasing term on the photographic plate

used to record the matched filter. Thus for  $\omega = 0$  and any angle between the beams, the bias intensity is

$$I_{bias} = (I_0/2) \sin^2(90^\circ - \alpha) \quad (9)$$

for a total signal beam intensity of  $I_0/2$ .

The net result of the change in fringe visibility and increase in prebias on the matched filter is a reduction in the optimization of the matched filter. Both correlation signal and signal-to-clutter ratio are reduced. The multiple exposure (noncoherent) addition technique is particularly affected as the input image is rotated for each exposure, changing fringe visibility. Also the prebias terms add with each successive exposure. Figure 3 shows a comparison between noncoherently added matched filters with good fringe visibility and birefringence-reduced fringe visibility when tested by playing a known reconnaissance scene containing the recorded target (M-60 tank) in a terrain background

with false targets (other vehicles). The signal-to-clutter ratio is quite poor in (a), which was made with birefringent input imagery, while the target correlation stands out well in (b), which was made with good fringe visibility.

Techniques must be employed to minimize the problems caused when working with birefringent images. Copying the input film onto acetate based materials overcomes the problem, but it is not necessarily a desirable technique. A blank piece of processed film may be cut from the same birefringent stock as the input image, placed in an iso-optical gate in the reference beam, and rotated as necessary with the input (signal) image to yield best fringe visibility.<sup>6</sup> Recently, multiple target imagery such as that shown in Fig. 1 has been used to produce effective noncoherently added image matched filters. The image is first rotated to align one strand axis (fast or slow) with the beam polarization to maximize fringe visibility with the fixed reference beam. Then a mask is used to uncover one target at a time for each successive exposure of the matched filter. The final result is a multiple overlay matched filter, noncoherently added with no input image rotation required. Four-element matched filters of this type have been successfully recorded in silver halide using this technique. Naturally, the properly aligned multiple target image may be used for preparation of high-quality coherently added matched filters as well.

As suggested by several reviewers, the degree of birefringence varies to a certain extent over the area of each sample film due to nonuniform stretching during manufacture. Such variations make the previously suggested corrections only first-order approximations, which do not totally solve the problems introduced by the birefringence. However, the suggested techniques have resulted in significant improvements in the performance of matched filters recorded from birefringent imagery.

The research was sponsored in part by the Air Force Office of Scientific Research (AFSC), U. S. Air Force, under contract F49620-78-C-0051.



(a) With Birefringence-Reduced Carrier Fringe Visibility



(b) With Good Carrier Fringe Visibility

Fig. 3. Comparison of correlation planes using noncoherently added matched filters without (a) and with (b) optimum fringe formation due to birefringent input film.

#### References

1. A. B. Vander Lugt, IEEE Trans. Inf. Theory IT-10, No. 2, 139 (Apr. 1964).
2. Optical Matched Filter Image Correlator, U.S. Patent 3,779,492.
3. K. B. Leib, R. A. Bondurant, S. Hsiao, M. R. Wohlers, and R. Herold, Appl. Opt. 17, 2892 (1978).
4. K. G. Leib, R. A. Bondurant, and M. R. Wohlers, "Optical Matched Filter Correlator Memory Techniques and Storage Capacity," at SPIE East Conference, Washington, D. C. (April 1979) SPIE 177, Optical Information Storage (1979).
5. Eastman Kodak Co., *Physical and Chemical Behavior of Kodak Aerial Films*, Publication M-63 (Apr. 1973), p. 26.
6. R. A. Bondurant and K. G. Leib, Opt. Laser Technol. 9, No. 3, 124 (June 1977).

## APPENDIX C

### KOWARSCHIK'S EQUATIONS FOR SEQUENTIALLY STORED GRATINGS

1. From "Diffraction Efficiency of Sequentially Stored Gratings in Transmission Volume Holograms," Optica Acta, 25, 67-81, 1978

$$\left. \begin{array}{l} A = -2j \rho_z \\ B = \beta^2 - \rho^2 \\ C_i = 2 \kappa_i \beta \\ D_i = -2j \delta_{iz} \\ E = \beta^2 - \delta_i^2 \end{array} \right\} \quad (6)$$

$$\left. \begin{array}{l} \text{where } \kappa_i = \pi n_i / \lambda \\ \beta = 2\pi n / \lambda \end{array} \right\} \quad (7)$$

and  $n$  = refractive index (mean value) of recording medium

$n_i$  = amplitude of spatial modulation of  $i$ -th grating

$\lambda$  = vacuum wavelength

$\bar{\rho}$  = reference beam wave vector

$\bar{\delta}$  = signal beam wave vector

$\hat{z}$  = surface normal

2. The diffraction efficiency ( $\eta$ ) is given by:

$$\left. \begin{array}{l} \eta = n_1 + n_2 \\ = \frac{|D_1|}{|A|} |S_1|^2 + \frac{|D_2|}{|A|} |S_2|^2 \end{array} \right\} \quad (19)$$

where the abbreviated terms are as follows:

$$\left. \begin{aligned} \xi_1 &= -\frac{1}{2}(u + v), \\ \xi_2 &= \frac{\sqrt{3}}{2}(u - v), \\ \hat{v} &= -\frac{3}{2}j(u + v) + j\frac{\omega_1}{3}, \\ F_i &= \frac{C_i}{D_i} \left( \frac{E_i}{D_i} - u - v \right), \\ G_i &= \frac{C_i}{D_i} \left( -\hat{v} \frac{E_i}{D_i} + \hat{p}_1^2 + \xi_1^2 + \xi_2^2 \right), \\ H_1 &= \frac{1}{A} \left( \frac{C_1^2}{D_1} + \frac{C_2^2}{D_2} \right) + \xi_1^2 + \xi_2^2, \\ H_2 &= \frac{1}{A} \left( \frac{C_1^2}{D_1} + \frac{C_2^2}{D_2} \right) \hat{v} + j\hat{p}_1 (\xi_2^2 - j\xi_1 \hat{v}), \\ H_3 &= \frac{1}{A} \left( \frac{C_1^2}{D_1} + \frac{C_2^2}{D_2} \right) + \hat{p}_1 (-\hat{p}_1 + 2\xi_1), \end{aligned} \right\} (18)$$

and

$$\left. \begin{aligned} \omega_1 &= \frac{E_1}{D_1} + \frac{E_2}{D_2} + \frac{B}{A}, \\ \omega_2 &= \frac{1}{AD_1 D_2} (E_1 BD_2 - C_1^2 D_2 + AE_1 E_2 + BD_1 E_2 - C_2^2 D_1), \\ \omega_3 &= \frac{1}{AD_1 D_2} (C_1^2 E_2 + C_2^2 E_1 - BE_1 E_2). \end{aligned} \right\} (10)$$

$$\left. \begin{aligned} \hat{p}_1 &= u + v - \frac{\omega_1}{3}, \\ \hat{p}_2 &= -\frac{1}{2}(u + v) + j\frac{\sqrt{3}}{2}(u - v) - \frac{\omega_1}{3}, \\ \hat{p}_3 &= -\frac{1}{2}(u + v) - j\frac{\sqrt{3}}{2}(u - v) - \frac{\omega_1}{3}. \end{aligned} \right\} (11)$$

$$\left. \begin{array}{l} u = \sqrt[3]{[-q + \sqrt{(q^2 + p^3)}], \\ v = \sqrt[3]{[-q - \sqrt{(q^2 + p^3)}], } \end{array} \right\} \quad (12)$$

$$\left. \begin{array}{l} p = \frac{\omega_2}{3} - \frac{\omega_1^2}{9}, \\ q = \left(\frac{\omega_1}{3}\right)^3 - \frac{\omega_1\omega_2}{6} + \frac{\omega_3}{2}. \end{array} \right\}$$

3. The signal terms  $S_i$  are given by:

$$\left. \begin{array}{l} |S_i(z)|^2 = (\xi_2^2(\xi_2^2 - \hat{v}^2)^2)^{-1} \{ F_i^2 \xi_2^2 (\cos [\hat{v}z] \\ - \cos [\xi_2 z])^2 + (\xi_2 F_i \sin [\hat{v}z] + G_i \sin [\xi_2 z])^2 \}, \end{array} \right\} \quad (16)$$

## APPENDIX D

### THE FOURIER TRANSFORM OF COHERENTLY ADDED IMAGES

#### RECTANGULAR COORDINATE SYSTEM

This appendix deals with the Fourier transform properties of an N-element input array which constitutes the input image for the coherent addition of images to form a single, complex matched filter. The array is formed by considering the basic image pattern (e.g., an M-60 tank) as being translated and/or rotated in a plane.

Let  $E(x, y)$  represent the amplitude transmittance of the single pattern. The shaded area in Fig. D-1 represents schematically this 2-D transmittance pattern. In this experimental program, the origin is chosen as the center of the regularly placed images of constant radii. Random arrays are random in radii only. (See Fig. 3-12). The Fourier transform distribution for this single input is labeled  $F(\omega_x, \omega_y)$ , in terms of the spatial frequency variables  $\omega_x, \omega_y$ .

Let  $S_T(x, y)$  be the amplitude transmittance of a translated pattern, as illustrated in Fig. D-1. If  $x_T, y_T$  are the coordinate distances through which the pattern has been translated (without rotation), then  $S_T$  can be expressed as

$$S_T(x, y) = E((x-x_T), (y-y_T)) \quad (D-1)$$

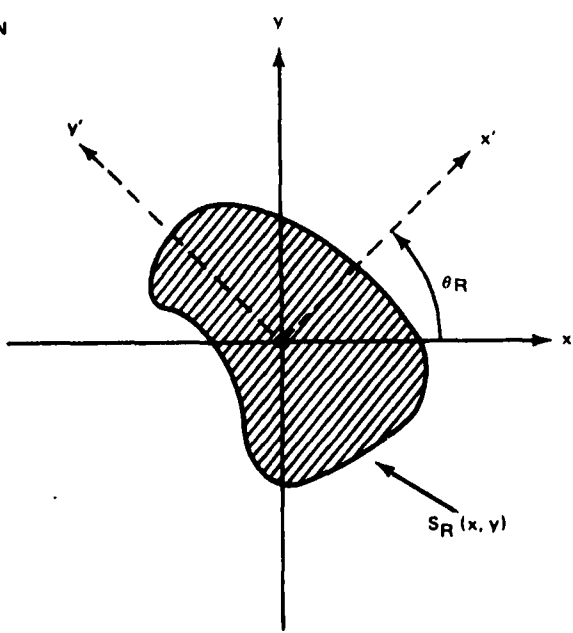
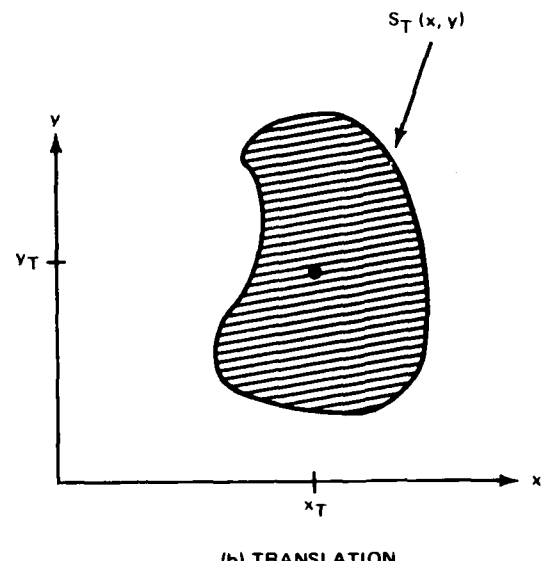
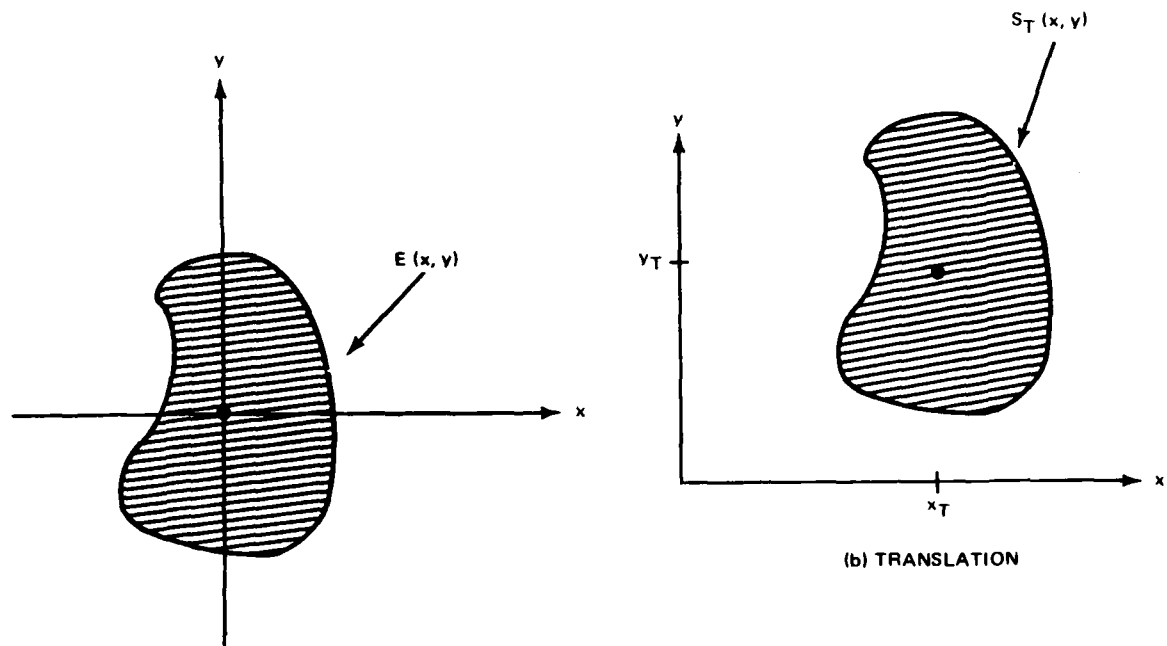
In Fig. D-1, the input pattern has been rotated (without translation) through an angle  $\Theta_R$ . The amplitude transmittance  $S_R(x, y)$  is given by

$$S_R(x, y) = E(x', y') \quad (D-2a)$$

where

$$x' = x \cos \theta_R + y \sin \theta_R$$

$$y' = -x \sin \theta_R + y \cos \theta_R$$



1283-006(a)(T)

Fig. D-1 Transmittance of Single Pattern Under Translation and Rotation

Or equivalently

$$x = x' \cos \theta_R - y' \sin \theta_R$$

$$y = x' \sin \theta_R + y' \cos \theta_R$$

(D-2b)

An expression for the amplitude transmittance  $S_{TR}(x, y)$  for an input pattern with combined translation and rotation as in Fig. D-2 is now sought. First, accounting for translation, one has

$$S_{TR}(x, y) = S_R((x - x_T), (y - y_T)).$$

From Eq. (2), one finds that

$$S_{TR}(x, y) = E(\bar{x}, \bar{y}) \quad (D-3a)$$

where

$$x = x_T + \bar{x} \cos \theta_R - \bar{y} \sin \theta_R \quad (D-3b)$$

$$y = y_T + \bar{x} \sin \theta_R + \bar{y} \cos \theta_R$$

Now consider the amplitude transmittance  $T(x, y)$  for a collection of  $N$ -elements which are translated and rotated replications of the particular input pattern. Let  $S_i(x, y)$  be the transmittance pattern of the  $i$ -th element; i.e.,

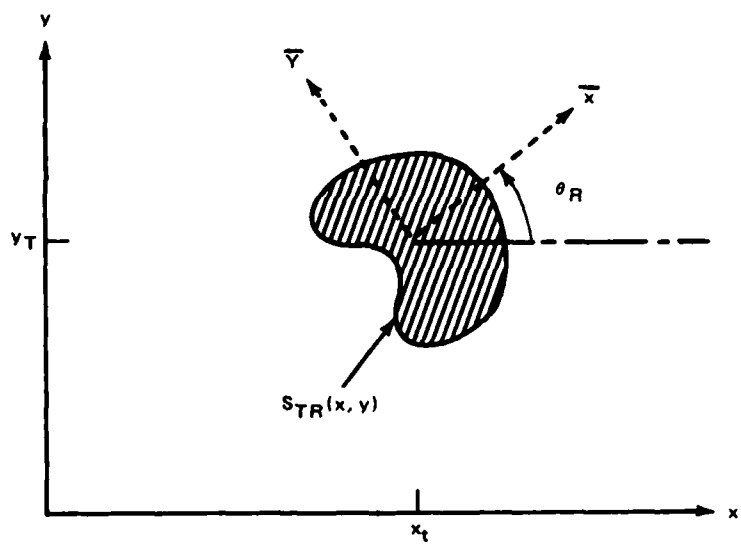
$$S_i(x, y) = (S_{TR}(x, y))_i$$

Thus

$$T(x, y) = \sum_{i=1}^N S_i(x, y) \quad (D-4)$$

The Fourier transform of this sum is

$$F(\omega_x, \omega_y) = \sum_{i=1}^N \iint_{-\infty}^{\infty} S_i(x, y) e^{-j(\omega_x x + \omega_y y)} dx dy \quad (D-5)$$



1283-007(a)(T)

Fig. D-2 Transmittance of Pattern with Combined Translation and Rotation

Using Eq. D-3, this reduces to

$$\begin{aligned}
 F(\omega_x, \omega_y) = \sum_{i=1}^N e^{-j\omega_x X_i} e^{-j\omega_y Y_i} \iint_{-\infty}^{\infty} E(\bar{X}_i, \bar{Y}_i) \\
 e^{-j\bar{X}_i(\omega_x \cos \theta_i + \omega_y \sin \theta_i)} \\
 e^{-j\bar{Y}_i(-\omega_x \sin \theta_i + \omega_y \cos \theta_i)} \\
 d\bar{X}_i d\bar{Y}_i
 \end{aligned} \tag{D-6}$$

where

$$x_i = (x_T)_i, y_i = (y_T)_i, \theta_i = (\theta_R)_i.$$

To simplify the notation set

$$\begin{aligned}
 \alpha_i &= \omega_x \cos \theta_i + \omega_y \sin \theta_i \\
 \beta_i &= -\omega_x \sin \theta_i + \omega_y \cos \theta_i
 \end{aligned} \tag{D-7}$$

Finally, one has

$$F(\omega_x, \omega_y) = \sum_{i=1}^N e^{-j(\omega_x X_i + \omega_y Y_i)} F(\alpha_i, \beta_i) \tag{D-8}$$

relating the Fourier transform of the array to that for a single input pattern. (Note that at  $\omega_x = 0 = \omega_y$ )

$$F(0,0) = \sum_{i=1}^N F(0,0) = N \cdot F(0,0)$$

Hence, the corresponding DC light intensity or exposure is proportional to  $F^*(0,0) = N^2 FF^*(0,0)$ , where  $F^*$  is the complex conjugate of  $F$ . If the  $N$ -input images in the array are processed in sequence rather than simultaneously, the resulting DC light exposure is the sum

$$F^*(0,0) = \sum_{i=1}^N FF^*(0,0) = N \cdot FF^*(0,0). )$$

Symmetries in the input transmittance pattern carry over to the Fourier transform function. For symmetry about the  $y$ -axis, one has  $E(-x,y) = E(x,y)$  and consequently

$$F(-\omega_x, \omega_y) = F(\omega_x, \omega_y)$$

Similarly, for a pattern that is symmetric about the  $x$ -axis one has  $E(x,-y) = E(x,y)$ , and then

$$F(\omega_x, -\omega_y) = F(\omega_x, \omega_y)$$

Finally, for symmetry with respect to both axes, (i.e., with respect to the origin), one has  $E(-x,-y) = E(x,y)$  and

$$F(-\omega_x, -\omega_y) = F(\omega_x, \omega_y)$$

Tables D-1 to D-3 illustrate the specific parametric values and the transform for  $N = 2, 4, 8$  in rectangular coordinates. The transform expressions are omitted for  $N = 10$  in Table D-3 for simplicity.

#### POLAR COORDINATE SYSTEM

For input functions that possess radial symmetry,  $E(x,y) = E(\rho)$ , where  $\rho$  is the radial polar coordinate. In this case, one is only concerned with translational effects since the transmittance function is insensitive to rotation; i.e.,  $S_R(x,y) = E(\rho)$  as well. From Eq. (D-1)

$$S_T(x,y) = E(\bar{\rho}) \quad (D-9a)$$

TABLE D-1 EXAMPLES OF SYMMETRICALLY ORIENTED PATTERNS WITH  
RECTANGULAR SYMMETRY

N	X <sub>i</sub>	Y <sub>i</sub>	O <sub>i</sub>	$\alpha_i$	$\beta_i$	$F(\omega_x, \omega_y)$
2	0	-d	0°	$\omega_x$	$\omega_y$	$\text{EXP}(j\omega_y d) \cdot F(\omega_x, \omega_y) +$
	0	d	180	$-\omega_x$	$-\omega_y$	$\text{EXP}(-j\omega_y d) \cdot F(-\omega_x, -\omega_y)$
3	0	-d	0	$\omega_x$	$\omega_y$	$\text{EXP}(j\omega_y d) \cdot F(\omega_x, \omega_y) +$
	$\sqrt{3}d/2$	$d/2$	30	$(\sqrt{3}\omega_x + \omega_y)/2$	$(-\omega_x + \sqrt{3}\omega_y)/2$	$\text{EXP}(-jd(\sqrt{3}\omega_x + \omega_y)/2) \cdot$
	$-\sqrt{3}d/2$	$d/2$	120	$(-\sqrt{3}\omega_x + \omega_y)/2$	$(-\omega_x - \sqrt{3}\omega_y)/2$	$F([\sqrt{3}\omega_x + \omega_y]/2, [-\omega_x + \sqrt{3}\omega_y]/2) +$
						$\text{EXP}(-jd(-\sqrt{3}\omega_x + \omega_y)/2) \cdot$
						$F([-\sqrt{3}\omega_x + \omega_y]/2, [-\omega_x + \sqrt{3}\omega_y]/2)$
4	0	-d	0	$\omega_x$	$\omega_y$	$\text{EXP}(j\omega_y d) F(\omega_x, \omega_y) +$
	d	0	90	$\omega_y$	$-\omega_x$	$\text{EXP}(-j\omega_x d) F(\omega_y, -\omega_x) +$
	0	d	180	$-\omega_x$	$-\omega_y$	$\text{EXP}(-j\omega_y d) F(-\omega_x, -\omega_y) +$
	-d	0	270	$-\omega_y$	$\omega_x$	$\text{EXP}(j\omega_x d) F(-\omega_y, \omega_x)$
8	0	-d	0°	$\omega_x$	$\omega_y$	$\text{EXP}(j\omega_y d) F(\omega_x, \omega_y) +$
	$d/\sqrt{2}$	$-d/\sqrt{2}$	45	$(\omega_x + \omega_y)/\sqrt{2}$	$(-\omega_x + \omega_y)/\sqrt{2}$	$\text{EXP}(-j\omega_x d) \frac{\text{EXP}(j\omega_y d)}{\sqrt{2}} F(\omega_x + \omega_y, -\omega_x + \omega_y) \frac{\sqrt{2}}{\sqrt{2}}$
	d	0	90	$\omega_y$	$-\omega_x$	$+ \text{EXP}(-j\omega_x d) F(\omega_y, -\omega_x) +$
	$d/\sqrt{2}$	$d/\sqrt{2}$	135	$(-\omega_x + \omega_y)/\sqrt{2}$	$(-\omega_x + \omega_y)/\sqrt{2}$	$\text{EXP}(-j\omega_x d) \frac{\text{EXP}(-j\omega_y d)}{\sqrt{2}} F(-\omega_x + \omega_y, -(\omega_x + \omega_y)) \frac{\sqrt{2}}{\sqrt{2}}$
	0	d	180	$-\omega_x$	$-\omega_y$	$+ \text{EXP}(-j\omega_y d) F(-\omega_x, -\omega_y) +$
	$-d/\sqrt{2}$	$d/\sqrt{2}$	225	$-(\omega_x + \omega_y)/\sqrt{2}$	$(\omega_x - \omega_y)/\sqrt{2}$	$\text{EXP}(-j\omega_x d) \frac{\text{EXP}(+j\omega_y d)}{\sqrt{2}} F(-\omega_x + \omega_y, \omega_x - \omega_y) \frac{\sqrt{2}}{\sqrt{2}}$
	-d	0	270	$-\omega_y$	$\omega_x$	$+ \text{EXP}(-j\omega_y d) F(-\omega_x, \omega_y) +$
	$-d/2$	$-d/\sqrt{2}$	315	$(\omega_x - \omega_y)/\sqrt{2}$	$(\omega_x + \omega_y)/\sqrt{2}$	$\text{EXP}(-j\omega_x d) \frac{\text{EXP}(j\omega_y d)}{\sqrt{2}} F((\omega_x - \omega_y), \omega_x + \omega_y) \frac{\sqrt{2}}{\sqrt{2}}$

1283-011(a)(T)

TABLE D-2 EXAMPLES OF SYMMETRICALLY ORIENTED PATTERNS WITH  
RECTANGULAR SYMMETRY FOR N = 10

N	$x_i$	$y_i$	$\theta_i$	$\alpha_i$	$\beta_i$
10	0	-d	0°	$\omega_x$	$\omega_y$
	0.5878d	-0.8090d	36°	$0.8090 \omega_x + 0.5878 \omega_y$	$-0.5878 \omega_x + 0.8090 \omega_y$
	0.9511d	-0.3090d	72	$0.3090 \omega_x + 0.9511 \omega_y$	$-0.9511 \omega_x + 0.3090 \omega_y$
	0.9511d	0.3090d	108	$-0.3090 \omega_x + 0.9511 \omega_y$	$-0.9511 \omega_x - 0.3090 \omega_y$
	0.5878d	0.8090d	144	$-0.8090 \omega_x + 0.5878 \omega_y$	$-0.5878 \omega_x - 0.8090 \omega_y$
	0	d	180	$-\omega_x$	$-\omega_y$
	-0.5878d	0.8090d	216	$-0.8090 \omega_x - 0.5878 \omega_y$	$0.5878 \omega_x - 0.8090 \omega_y$
	-0.9511d	0.3090d	252	$-0.3090 \omega_x - 0.9511 \omega_y$	$0.9511 \omega_x - 0.3090 \omega_y$
	-0.9511d	-0.3090d	288	$0.3090 \omega_x - 0.9511 \omega_y$	$0.9511 \omega_x + 0.3090 \omega_y$
	-0.5878d	-0.8090d	324	$0.8090 \omega_x - 0.5878 \omega_y$	$0.5878 \omega_x + 0.8090 \omega_y$

1283-012(a)(T)

TABLE D-3 EXAMPLES OF SYMMETRICALLY ORIENTED PATTERNS  
WITH RADIAL SYMMETRY

N	$\rho T_i$	$\psi T_i$	$F(\omega, \xi)/F(\omega)$
2	d	0°	
	d	180°	$2 \cos(\omega d \cos \xi)$
3	d	0	
	d	120	$\exp(-j\omega d \cos \xi) + \exp\left(j\frac{\omega d \cos \xi}{2}\right) \cdot \cos\left(\frac{\omega d \sqrt{3} \sin \xi}{2}\right)$
	d	240	
4	d	0	
	d	90	$2 \cos(\omega d \cos \xi) + 2 \cos(\omega d \sin \xi)$
	d	180	
	d	270	
8	d	0	
	d	45	$2 \cos(\omega d \cos \xi) + 2 \cos(\omega d \sin \xi)$
	.	90	$+ 4 \cos(\omega d \cos \xi / \sqrt{2}) \cdot \cos(\omega d \sin \xi / \sqrt{2})$
	.	135	
	.		
	d	315	
1283-013(a)(T)			

where  $\bar{\rho}$ ,  $\bar{\psi}$  are polar coordinates centered about the point  $(x_T, y_T)$ , and

$$\begin{aligned} x - x_T &= \bar{\rho} \cos \bar{\psi} \\ y - y_T &= \bar{\rho} \sin \bar{\psi} \\ x_T &= \rho_T \cos \psi_T, \quad y = \rho_T \sin \psi_T \end{aligned} \quad (D-9b)$$

Figure D-3 shows these coordinate variables.

The amplitude transmittance for a collection of N-elements is given by Eq. (D-4). The corresponding Fourier transform of this sum for N-radially symmetric inputs is

$$\begin{aligned} F(\omega_x, \omega_y) &= \sum_{i=1}^N \iint_{-\infty}^{\infty} E(x-x_i, y-y_i) e^{-j(\omega_x X + \omega_y Y)} dx dy \\ &= \sum_{i=1}^N e^{-j(\omega_x X_i + \omega_y Y_i)} \iint_{-\infty}^{\infty} E(\bar{\rho}_i) \bar{\rho}_i d\bar{\rho}_i d\bar{\psi}_i \\ &\quad e^{-j\bar{\rho}_i (\omega_x \cos \psi_i + \omega_y \sin \psi_i)} \end{aligned} \quad (D-10)$$

using the i-subscript notation. With the substitutions for spatial frequency variables in polar form

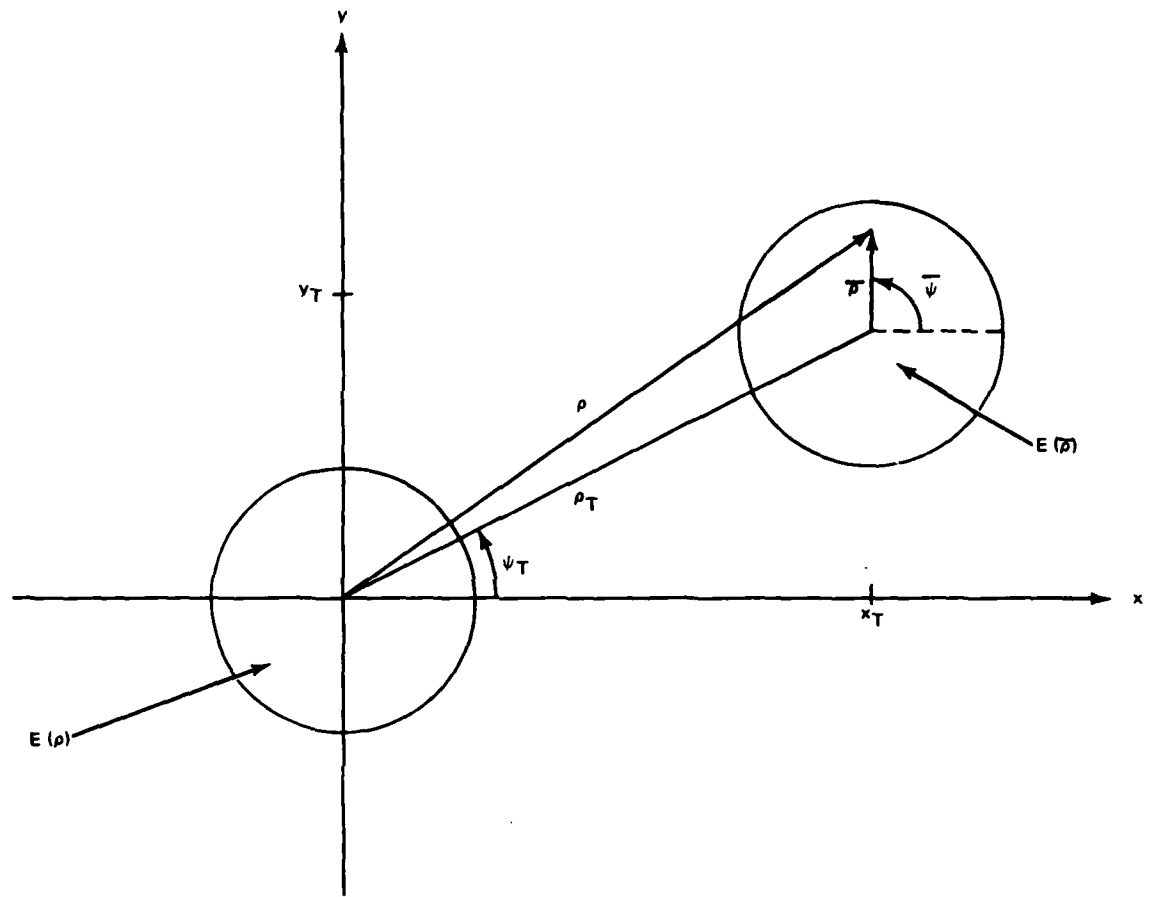
$$\omega_x = \omega \cos \xi, \quad \omega_y = \omega \sin \xi,$$

the last exponential term in Eq. (D-10) becomes

$$\exp(-j\bar{\rho}_i \omega \cos(\bar{\psi}_i - \xi)).$$

The integral over the  $\psi$ -variable is a Bessel function identity

$$J_0(\bar{\rho}_i \omega) = \int_0^{2\pi} e^{-j\bar{\rho}_i \omega \cos(\bar{\psi}_i - \xi)} d\bar{\psi} \quad (D-11)$$



1283-008(a)(T)

**Fig. D-3 Polar Coordinates for a Translated, Radially Symmetric Input Pattern**

Thus, Eq. (D-10) becomes

$$F(\omega_x, \omega_y) = \sum_{i=1}^N e^{-j(\omega_x X_i + \omega_y Y_i)} \int E(\bar{\rho}_i) \bar{\rho}_i J_0(\rho_i \omega) d\bar{\rho}_i$$

Because of radial symmetry, the integral is identical for all values of  $i$ ; thus

$$F(\omega, \xi) = F(\omega) \sum_{i=1}^N e^{-j\omega \rho_{Ti}} (\cos \xi \cos \psi_{Ti} + \sin \xi \sin \psi_{Ti})$$

or finally

$$F(\omega, \xi) = F(\omega) \sum_{i=1}^N e^{-j\omega \rho_{Ti}} \cos(\xi - \psi_{Ti}) \quad (D-12)$$

Table D-4 illustrates the specific parametric values and the transform for  $N = 2-4, 8$  with polar symmetry.

## APPENDIX E

### ADDITIONAL SIMULATIONS

During the course of this contract we developed a digital simulation of many aspects of the OMFIC device. This digital simulation allowed parametric studies to be carried out rapidly and with repeatability and control not achievable in the laboratory. This appendix contains two papers which describe in detail two such studies. The first paper is concerned with the sensitivity of matched filters to different but typical terrains. It shows the possibility of quantifying the motion of clutter using cross-correlation as a measure of clutter. In the second paper a study of some digital preprocess techniques is carried out. Also the rotational sensitivity of the matched filter combined with various preprocessing methods is examined.

**Digital analysis of the effects of terrain clutter on the performance of matched filters for target identification and location\***

J. Mendelsohn, M. Wöhlers, and K. Leib  
Research Department  
Gruuman Aerospace Corporation  
Bethpage, New York 11714

**Abstract**

A digital analysis of the effect of terrain-target interactions on the signal-to-clutter (S/C) ratio of the output of a matched filter is made. Three terrain types (woodland, village, and roadside) were included in the investigation. A photographic image of an M-60 tank used as the target was digitized (512 x 512 pixels) and a matched filter constructed digitally, using a two-dimensional FFT algorithm. The matched filter was then used to obtain the correlation between the target and the various terrain types to obtain the signal-to-clutter ratio.

Various high frequency versions of the matched filter were systematically investigated for possible optimization in the S/C ratio in an attempt to optimize the design which was eventually realized in analog optical form. The computational aspects of the problem, from the point of view of doing digital image analysis on a minicomputer with limited memory, is also discussed.

**Introduction**

Optical matched filtering techniques have been under investigation for a number of years as a means for detecting known targets in various terrain backgrounds. The feasibility of this approach rests in part on the ability to store many different targets (and different views of the same target) in a holographic memory and, equally important, on the ability to search this memory rapidly. The system depicted in Figure 1 and patented by A. Grumet (1) allows for both the storage of a large number of matched filters and the

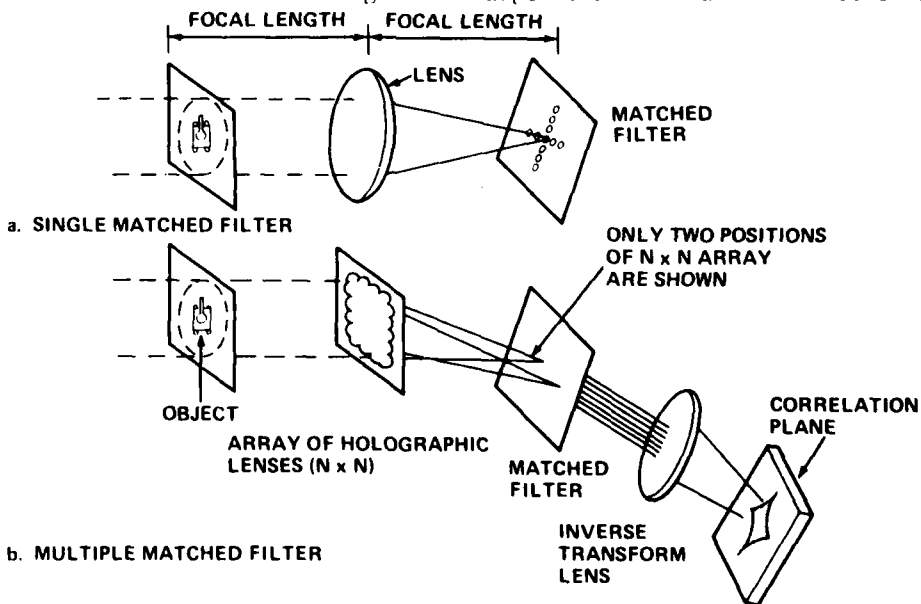


Fig. 1 Achievement of Large Arrays of Identical Transforms Through Use of Multiple Holographic Lenses

simultaneous interrogation of all the matched filters. This is accomplished by means of an array of holographic lenses which take its Fourier transform, replicate it for identification

\* This work was partially supported by the Air Force Office of Scientific Research under Contract F49620-78-C-0051

DIGITAL ANALYSIS OF THE EFFECTS OF TERRAIN CLUTTER ON THE PERFORMANCE OF  
MATCHED FILTERS FOR TARGET IDENTIFICATION AND LOCATION

and position the replicated transforms at corresponding positions in the matched filter or memory plane. The correlation between the object and the images stored in the memory is then obtained from the inverse Fourier transform lens. The question of the capacity of this type of system becomes a question of the physical dimensions, in the holographic memory, that the matched filter occupies, which depends upon the wavelength of the optical system, the focal length of the system, and the spatial frequency bandwidth of the matched filter. Techniques that would increase the number of matched filters that could be stored in any fixed sized holographic memory were previously discussed.<sup>(2)</sup>

The purpose of this paper is to present the results of an investigation that was directed toward the question of how much space must be allocated to each single matched filter. The study was conducted using a digital simulation of the analog optical holographic system and expresses the "size" of the matched filter in terms of the spatial bandwidth of the filter needed to achieve a given level of target detectability in the presence of the clutter signals that are generated through the matched filter by the background terrain. Thus the results presented will be phrased in terms of the S/C ratio of the peak values in the output correlation plane of the system, and the interest is in utilizing the smallest matched filter bandwidth to achieve a given S/C ratio.

Description of the Digital Simulations Utilized in the Study

The holographic technique used for the storage of the matched filters is the usual Vander Lugt one,<sup>(3)</sup> where the intensity of the exposure of the hologram is assumed to be given by

$$I_E = |(F + Re^{j2\pi x/\lambda})|^2$$

with R the amplitude of the reference beam,  $\alpha = \sin(\theta/\lambda)$  with  $\theta$  the offset angle between the reference and signal beam,  $\lambda$  the wavelength,  $x$  the physical coordinate variable in the transform plane, and F the spatial Fourier transform of the stored image (i.e., the matched filter). The medium used to store the hologram is then modeled by assuming that its optical transmission, t, is a linear function of the illuminating intensity,  $I_E$ , given by

$$t = \begin{cases} 1 - I_E/E_c & , 0 \leq I_E \leq E_c \\ 0 & , E_c \leq I_E \end{cases}$$

where  $E_c$  is a constant. The transmission function of the hologram will contain all the information in the illuminating beam if  $I_E = E_c$ ; otherwise there will be a "clipping" of the illuminating beam and therefore distortion in the stored hologram. This "clipping" is in fact used to select a band of spatial frequencies that will be stored in the hologram. With the simple model described above we have no "clipping" if  $\max(|F|) \cdot (|F| + R)^2 \leq E_c$ , some clipping if  $(|F| + R)^2 > E_c$ , and complete clipping if  $(|F| - R)^2 < E_c$ . Now if we select the reference beam amplitude, R, so that  $R = |F(f_c)| = T$ , where  $f_c$  is some specific spatial frequency, and in addition, adjust the exposure time so that  $(R^2 T)^2 = E_c$ , then we get no clipping or distortion for spatial frequencies such that  $|F(f)| \geq |F(f_c)|$  and complete clipping if  $(|F| - R)^2 > (|F| - T)^2 \geq E_c = (T + R)^2 = 4T^2$  or  $|F| \geq 3T$ . We see that there is a transition region between T and 3T where there will be a nonlinear distortion of the stored transform F. The model which was adopted neglects this transition region and assumes that the transmission of the hologram is directly proportional to F for all spatial frequencies such that  $|F(f)| < T = R$ , and that the transmission is zero for all other spatial frequencies. Thus when another image is transformed, say to produce G(f) and then used to illuminate the hologram, the resulting correlation component is obtained from the product  $G^*(f) F(f)$  where F(f) is a modified version of the transform of F(f) as indicated above; specifically, it is a band pass version of F(f) in that only those spatial frequencies for which  $|F(f)| \geq |F(f_c)|$  will yield nonzero outputs. Figure 2 illustrates typical results obtained from such a model applied to a digitized image of an M-60 tank (taken on a 512 x 512 pixel format with approximately 36 pixels across the tank width). These images correspond to the reimaged versions of modified transforms of the tank (set  $G^*(f) = 1$ ). The three different filters were obtained by selecting three different frequencies at which the threshold T was placed. Some of these thresholds correspond to the amplitude of the minor lobes in the Fourier transform of the tank along the frequency axis corresponding to the small dimension (width) of the tank. A plot of the transform along this axis is shown in Figure 3. The correspondence between these images and those obtained in an analog optical system is excellent. Figure 4 then contains the corresponding autocorrelation functions obtained with these matched filters (setting  $G^* = F^*$ ). Again, the correspondence with the analog system is excellent; particularly the dominant diamond shape at the center of the correlation signal for all filters.

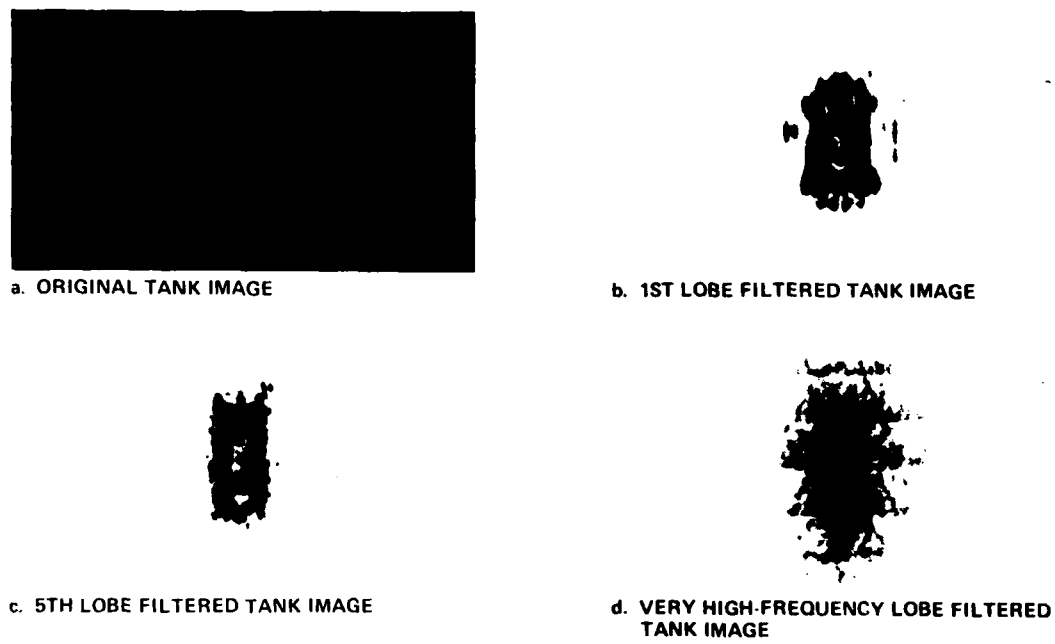


Fig. 2 Filtered Tank Images Obtained From  
the Simulation of the Holographic  
Matched Filter

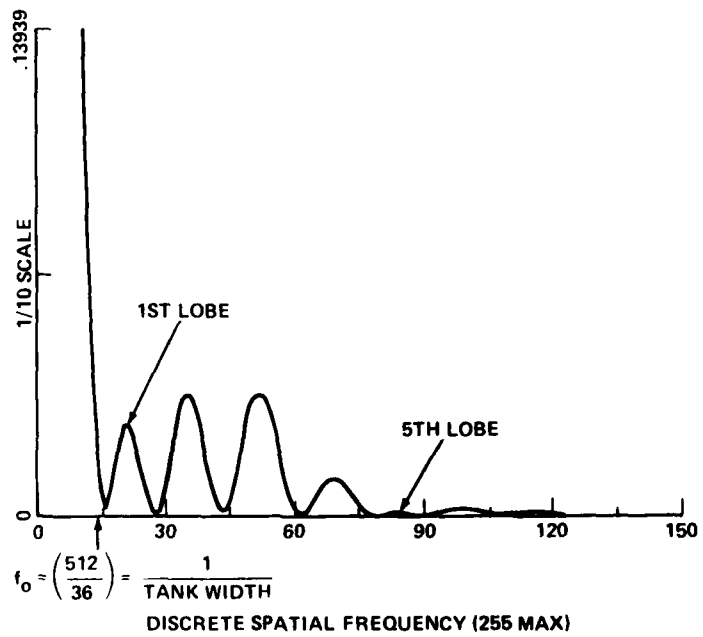


Fig. 3 Digital Simulation of the Amplitude of the M-60 Tank  
Spatial Fourier Transform Along the Frequency Axis  
Corresponding to the Small Dimension of the Tank

DIGITAL ANALYSIS OF THE EFFECTS OF TERRAIN CLUTTER ON THE PERFORMANCE OF  
MATCHED FILTERS FOR TARGET IDENTIFICATION AND LOCATION

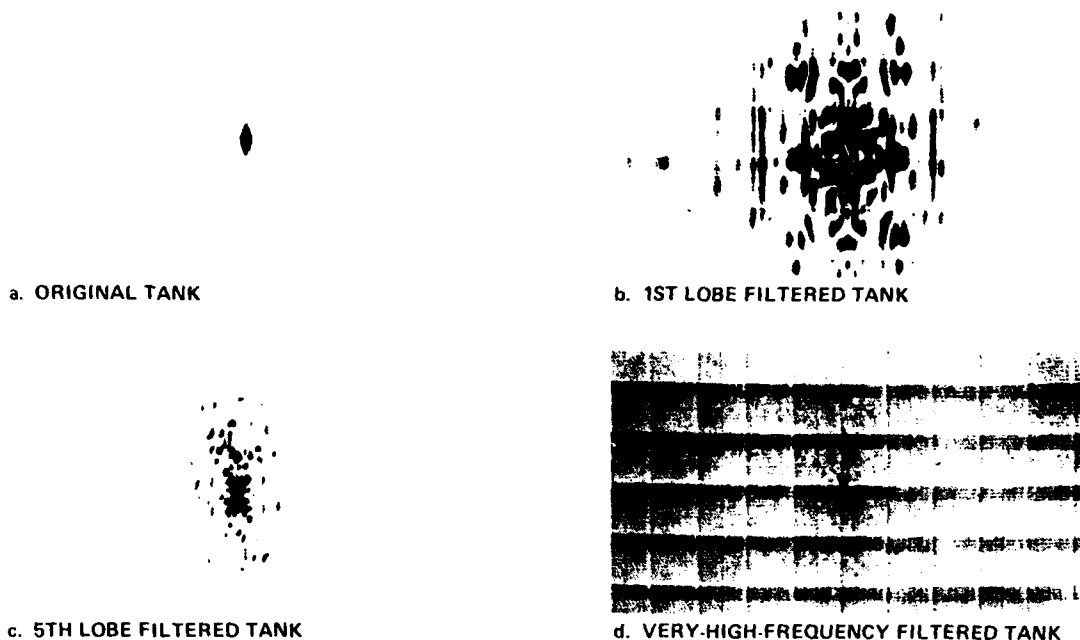


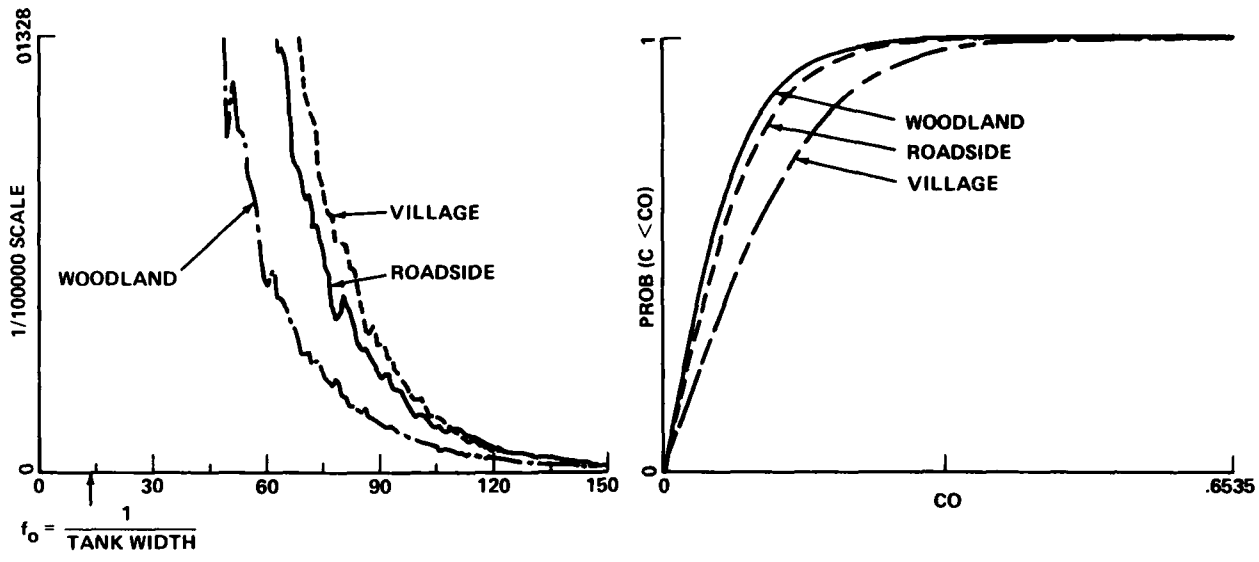
Fig. 4 Autocorrelations Obtained from the  
Simulated Matched Filter of Fig. 2

The results shown in the previous figures were obtained from a tank image that was digitized on a 512 x 512 pixel format; subsequently, all the two-dimensional Fourier transform operations were carried out using a two-dimensional Fast Fourier Transform (FFT) algorithm. The simulation was implemented on a minicomputer system consisting of a Data General Eclipse S/200, with 32K memory, a 10 megabyte disc, magnetic tape for long term storage of the images, and a scan converter/TV monitor output from which the images that appear in the figures were photographed.

Simulations of Target Detection in Various Terrain Backgrounds

The performance of various modifications of the matched filter were then studied using both the previously discussed thresholding and by restricting the total spatial frequency band used (by simply eliminating all spatial frequencies above some given cutoff frequency). Three different terrain views were utilized to ascertain the amount of clutter or false target response that would be produced in the various matched filters. Figure 5 shows the variation of the magnitude of the Fourier transform of these three scenes (again obtained with a 512 x 512 discrete FFT). Note the village scene and roadside scenes have greater high-frequency content than the woodland, as might be expected since these scenes have greater numbers of sharp edged discontinuities in contrast. Various matched filters of the M-60 tank were simulated, and the scenes were passed through these filters to determine the cross correlation. Figure 6 shows a cumulative histogram of the magnitude of the two-dimensional cross correlation between the three scenes and a single 3rd lobe matched filter with the output normalized to the maximum value of the autocorrelation of the tank. (The peak crosscorrelation on any one of the three scenes was 0.6535 of the autocorrelation.) The curves demonstrate that the correlation values or clutter signals are higher statistically across the village scene than the other two and that the woodland scene has the lowest clutter of the three. As an aside, we note that the cross-correlation with the M-60 tank is a quantitative measure of the clutter in the scenes relative to the tank as a standard, and this quantification could be of value to those trying to obtain nonphysiological measures of such concepts as clutter.

Table 1 contains a compilation of the peak clutter signals as well as their relationship to the peak autocorrelation values from the M-60 tanks for a variety of matched filters. In all cases, the matched filters were thresholded to the indicated suppression level (given as a fraction of the value of the magnitude of the zero frequency component of transform of the original tank), but otherwise all frequencies were present. We note that the zero order filter (unsuppressed) yielded unacceptable performance in all cases



DISCRETE SPATIAL FREQUENCY (255 MAX)

Fig. 5 Distribution of the Magnitude of the Fourier Transform of Three Different Scenes Used in the Study

Fig. 6 Cumulative Histogram of the Two-Dimensional Correlation (C) Signal Obtained Between a Third Lobe Matched Filter of an M-60 Tank and the Three Scenes (Normalized to the Peak Auto-correlation of the Tank)

Table 1. Digital Simulation of the Auto and Cross Correlation of Various Order Matched Filters of an M-60 Tank with the Three Scenes

Terrain	Lobe Order	Suppression Level	Peak Auto	Peak Clutter	S/C (DB)
Woodland	0	1.00000	168.783	265.462	-3.93347
	1	1.85138 E-02	30.6461	11.3396	8.63555
	2	2.47506 E-02	35.5385	16.8633	6.47514
	3	2.47455 E-02	35.4695	16.8008	6.49053
	4	7.34271 E-03	16.9125	6.45378	8.36788
	5	6.90004 E-04	3.90986	1.78171	6.82648
Roadside	6	1.23787 E-03	5.73741	2.24171	8.16271
	0	1.00000	168.783	225.261	-2.50712
	1	1.85138 E-02	30.6461	15.3904	5.98251
	2	2.47506 E-02	35.5385	20.6673	4.70832
	3	2.47455 E-02	35.4695	20.7427	4.65980
	4	7.34271 E-03	16.9125	10.1173	4.46287
Village	5	6.90004 E-04	3.90986	1.71455	7.16022
	6	1.23787 E-03	5.73741	2.91552	5.87997
	0	1.00000	168.783	248.933	-3.37507
	1	1.85138 E-02	30.6461	20.2929	3.58065
	2	2.47506 E-02	35.5385	23.2104	3.70033
	3	2.47455 E-02	35.4695	23.1797	3.69496
	4	7.34271 E-03	16.9125	12.7060	2.48399
	5	6.90004 E-04	3.90986	2.53437	3.76583
	6	1.23787 E-03	5.73741	4.21209	2.68436

(i.e., the peak clutter exceeded the peak tank signal) and that other suppressions yielded various levels of acceptable performance. Figure 7 displays typical performance variations obtained on the village scene (as we additionally imposed a frequency cutoff on the filter). It contains three of the previously mentioned M-60 matched filters, as well as one additional filter having a much lower suppression level, which tends to pass only much higher frequencies. We see that the very low suppression level filter produces the best performance (lowest peak clutter-to-peak signal), but at the expense of requiring a much higher

DIGITAL ANALYSIS OF THE EFFECTS OF TERRAIN CLUTTER ON THE PERFORMANCE OF MATCHED FILTERS FOR TARGET IDENTIFICATION AND LOCATION

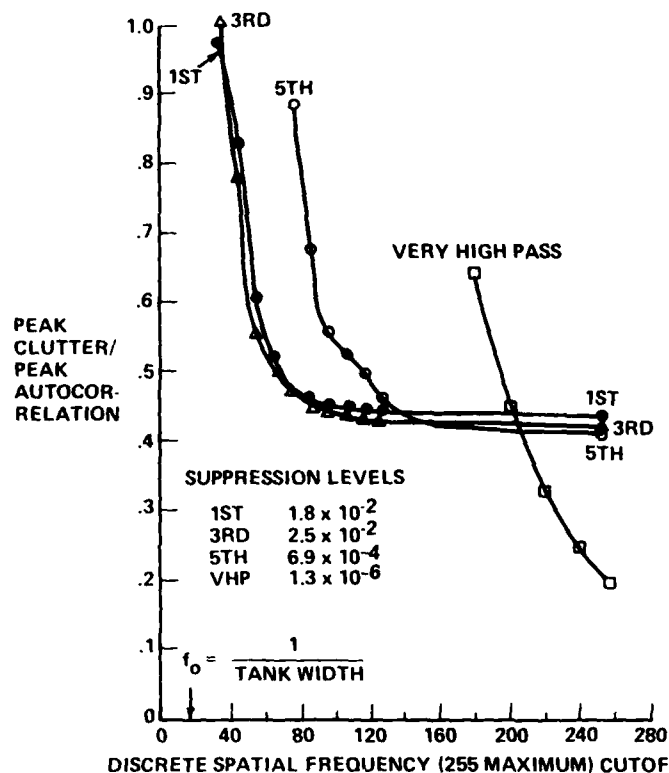


Fig. 7 Performance of Various Matched Filters of an M-60 Tank (Used on the Village Scene) with Various Cutoffs

Fig. 8 Location of Peak Matched Filter Output of Two M-60 Tank Filters on a Village Background Containing Four Tanks

frequency cutoff; i.e., the 1st, 3rd and 5th order filters could have been cutoff at a normalized frequency of 140 and still produce essentially the same performance ratio as would have been achieved at a cutoff of 255, but the very high frequency filter requires the full 255 cutoff to achieve the desired improvement.

Finally, a simulation was conducted of the performance of a variety of M-60 matched filters in locating tanks in the three scenes. Figure 8 and Table 2 contain the results of these studies for the village scene. In Figure 8, the location of certain output correlation plane peaks (local maxima) are shown in relation to four tanks that have been "digitally" placed into the scene. All peaks are shown whose amplitude exceeds the smallest value needed to locate all four tanks. A peak located a tank if it fell on the tank, and once a peak was found at some point in the scene all other peaks that fell within a region centered on that point with dimensions of the tank were not recorded as additional peaks. These results demonstrated that the very high pass filter, which we saw in Figure 7 had the least clutter ratio and was thus considered superior to the others, did not perform as well as anticipated. The reason for this was that the results quoted in Figure 7 (as well as in Table 1) used the autocorrelation of an isolated tank (white background) to form the ratio of signal-to-clutter used as the performance criterion. The alternative would have required a computation to be made with the tank placed in a large number of positions in the scene -- clearly an excessive burden. Now when the targets are positioned in the scene, as was done to obtain the results given in Table 2 and Figure 8, the effects of the nearby scene around the tank are felt in the peak correlation signal on the tank. This is borne out by the impulse responses of the various matched filters of the tanks (see Figure 2). One sees that the filtered tank images "spread out" beyond the boundaries of the original tank, and thus the nearby terrain will make a contribution to the correlation peak on the target. The very high frequency filter spreads out well beyond the tank outline and in a way that is very sensitive to the nearby terrain.

Table 2. Simulated Performance of Various M-60 Matched Filters  
in Locating Four Tanks in Various Positions in the  
Village Scene

	Village			
	1st Lobe Filter <sup>3</sup>	5th Lobe Filter <sup>3</sup>	Very High Pass Filter <sup>4</sup>	Low Frequency 5th Lobe Filter <sup>5</sup>
Range of Correlation Signals on Targets <sup>1</sup>	0.88-0.50	1.31-0.75	0.41-0.20	1.29-0.60
Max. Clutter 1,6	0.47 (.44)	0.45 (.46)	0.38 (.204)	1.15
Error's in Target Locations <sup>2</sup>	1/36, 1/36, 1/36, 1/36	1/36, 1/36 1/36, 1/36	1/36, 9.1/36 26/36, 28/36	0/36, 1/36 1.41/36, 1.41/36

#### Notes

- 1 Expressed as the squared ratio of the peak of the correlation signal on the target to the peak of the filtered autocorrelation signal of the target on a blank background.
- 2 Error in location of the four targets in the field of view expressed as fractions of the maximum width of the target.
- 3 1st and 5th lobe filters were limited to a frequency band that was less than 8.45 times the characteristic frequency corresponding to the target width.
- 4 The very high pass filter suppresses all frequency components larger in magnitude than  $1.35 \times 10^{-6}$  times the magnitude of the zero frequency component, but it had no frequency cutoff as did (3).
- 5 5th lobe filter with a normalized frequency cutoff of 4.23 times the characteristic frequency corresponding to the target width.
- 6 Numbers in parenthesis are the squares of the ratio of peak clutter signals with no targets present to the peak of the filtered autocorrelation signal of the target on a blank background.

#### Summary

Some selected results of a digital simulation, using two dimensional FFT algorithms, of an analog optical matched filter correlation system have been presented. These results demonstrate that excellent correspondence can be obtained between simulation and analog system by means of a linearized model of the holographic image storage medium. This in turn allows a simple Fourier transform model of the process to be employed that can be dealt with efficiently on a minicomputer system using a two-dimensional FFT algorithms. The resulting simulation enabled a study to be made of various techniques that would yield a reduction in the physical space allocated for the storage of a holographic matched filter. This work is part of a study of means to achieve large capacity optical memories for correlator applications and demonstrates that simulations can be effectively used in achieving that objective.

#### References

1. Grumet, A. U.S. Patent #3,779,492, "Automatic Target Recognition System," December 1973.
2. Leib, K., Bondurant, R. and Wohlers, M., "Matched Filter Correlator Memory Techniques and Storage Capacity," Proceedings of Soc. of Photo-Optical Instrumentation Engineers, Optical Information Storage, Vol. 177, April 1979.
3. Goodman, J., Introduction to Fourier Optics, McGraw Hill, New York, 1968.

## Digital methods in the design of optical matched filters for target recognition\*

J. Mendelsohn, M. R. Wohlers  
Research Department, Grumman Aerospace Corporation  
Mail Station A08-35 Bethpage, New York 11714

### Abstract

A digital simulation of an optical matched filter is described. Two important aspects of the optical device are investigated using the digital techniques. The first study involves the preprocessing of the image prior to performing the analog matched filtering operation and the second the sensitivity of the device to rotation of the target. These studies are carried out using a military target in common scenes such as villages, woodlands, and roads.

### Introduction

For the past several years, the Research Department of Grumman Aerospace Corporation has been investigating optical matched filtering as a means of detecting targets in a variety of military situations<sup>1-4</sup>. The system depicted in Fig. 1 and patented by A. Grumet allows for storage of a large number of matched filters and their simultaneous interrogation. The speed of such a system makes it feasible to overcome the traditional problems of the sensitivity of the matched filter to scale and orientation by storing many versions of the matched filters in various sizes and orientations. However, the optimization of the analog devices with respect to its many parameters (number of filters, spacing, bandwidth, etc.) is tedious and time consuming because of the laboratory time consumed in constructing a single matched filter, and the difficulty of precisely controlling this procedure. With this in mind, a digital simulation of the optical device was undertaken. During the course of the development of this digital simulation and subsequent investigations it became evident that digital preprocessing of the image could possibly enhance the performance of the optical devices. In a previous paper<sup>3</sup>, we discussed the studies performed to modify the basic matched filter and to optimize the bandwidth of the resulting matched filters. In this paper we will concentrate on two areas of investigation: digital preprocessing of the imagery and rotational sensitivity of the filter.

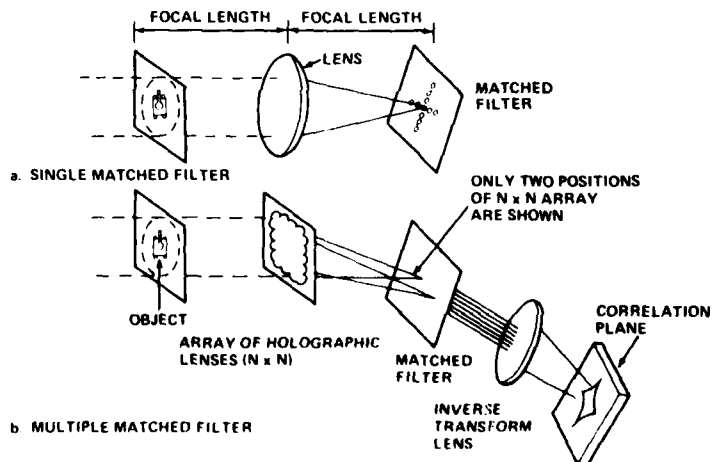


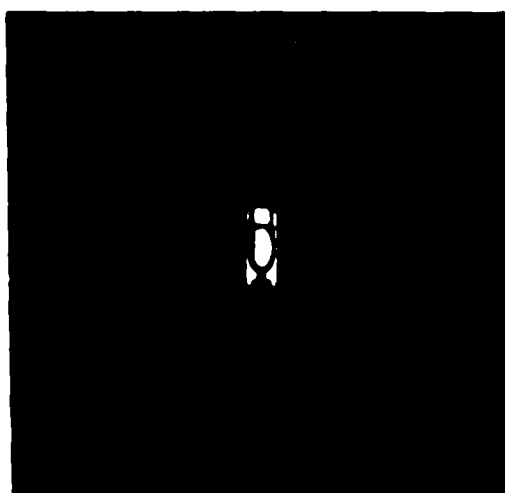
Fig. 1 Achievement of large arrays of identical transforms through use of multiple holographic lenses

### Digital simulation

The digital simulation used in this study is discussed in detail in our May 1979

#### DIGITAL METHODS IN THE DESIGN OF OPTICAL MATCHED FILTERS FOR TARGET RECOGNITION

paper.<sup>3</sup> The basic tool used in the simulation is a 512 x 512 two dimensional Fast Fourier Transform (FFT). Photographs of scale models of three typical backgrounds (woodland, village, and roadside) and an M-60 tank were digitized in a 512 x 512 pixel format and stored. (See Fig. 2.) Then the FFTs of the stored arrays were taken and the results conjugated to form an approximation to the matched filter used in the optical method. Agreement between the digital matched filters constructed in this way and the analog filters were excellent. Once the digital representation of the object have been obtained, it is a simple matter to perform controlled studies of the effect of filter modifications. The limiting factor becomes the time to perform the calculation (primarily the 2D FFT). In the analog world, the construction of a single matched filter may take several hours and it is a relatively difficult matter to maintain precise control of the process. The advantages of the digital simulation is clear, since with even moderate computational capability one can construct five digital matched filters (512 x 512) in an hour, with complete reproducibility.



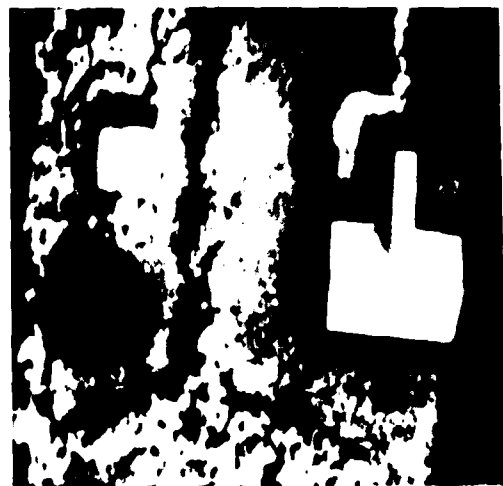
M-60 Tank



Woodland



Roadside



Village

Fig. 2 M-60 tank and three typical background scenes

Criteria for evaluation

In performing digital studies two criteria were used in the evaluation of the relative worth of a filter. The first was the peak-signal-to-peak-clutter ratio (S/C) which was obtained by finding the maximum intensity in the cross-correlation plane between the target, and the scenes without the target in them, and then comparing that value to the maximum cross correlations between the target on a clear background and the matched filter.

The second method was designed to provide an operational criteria for a particular matched filter. To obtain such a measure, four tanks were placed at random in a scene (See Fig. 3). The matched filter under study was then cross-correlated with that scene, and then the resulting cross-correlation plane was scanned. A hit was recorded if the point of maximum intensity in the plane landed on one of the tanks. A lethal radius (approximately half the dimension of the tank) was then imposed so that in the next scan this area was excluded. The process then was repeated until all four tanks were hit (or 20 weapons were expended). We now proceed to the two principle investigations of this paper; digital preprocessing and rotational sensitivities.

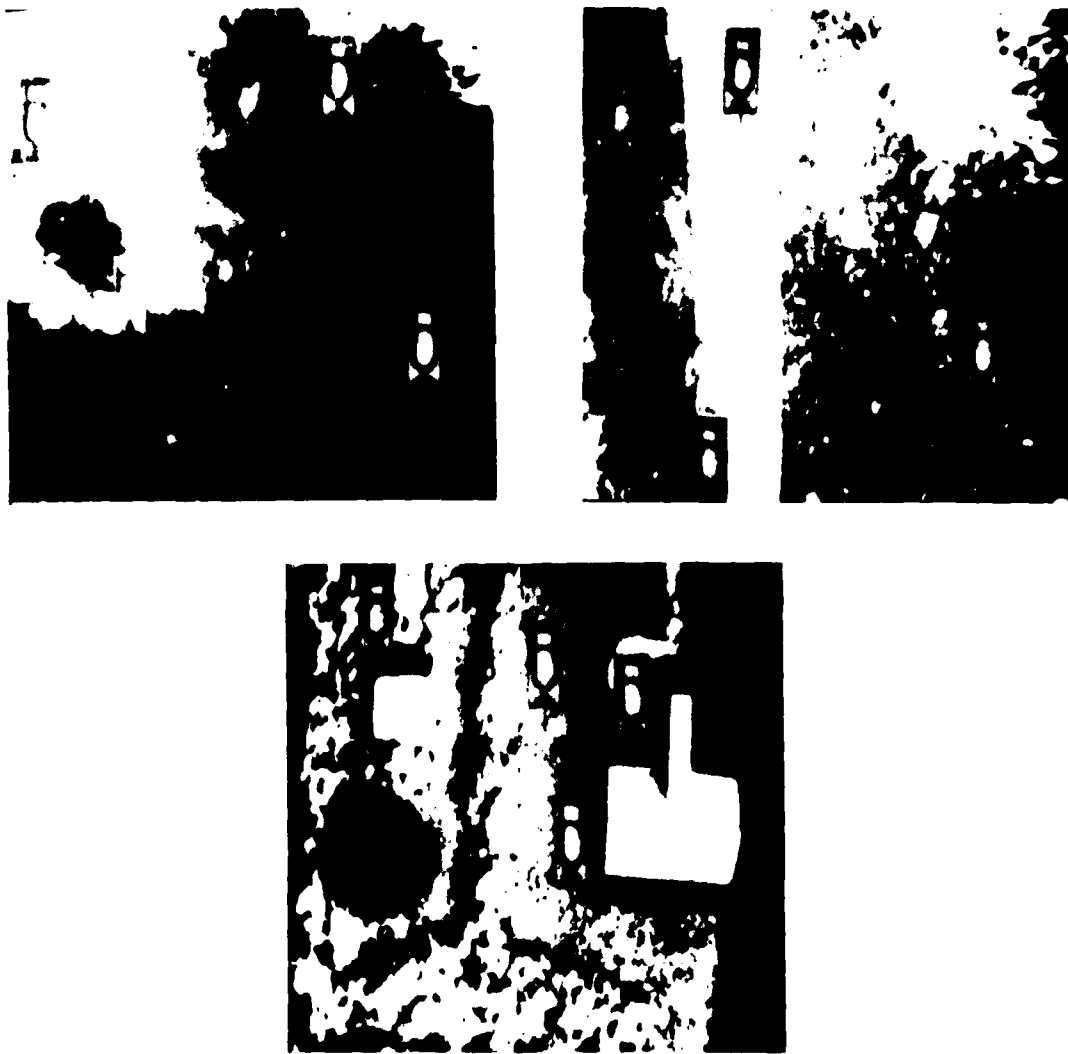


Fig. 3 M-60 tanks in three typical background scenes

DIGITAL METHODS IN THE DESIGN OF OPTICAL MATCHED FILTERS FOR TARGET RECOGNITION

Digital preprocessing

It has been established that a matched filter thresholded in such a way as to suppress amplitude values which are greater than the value at the 5th lobe of the Fourier transform of the target, perform relatively well<sup>3</sup>. Such a filter can be realized in an entirely analog fashion by using photographic techniques to suppress the lower lobes. We did, however, have evidence that processing the scene before applying the matched filter could improve on this performance without compromising the speed of the analog filter<sup>4,5</sup>. The important requirement is that the preprocessing could be performed in real time. A 3 x 3 convolution such as the Laplacian represented by the mask

$$\begin{matrix} 0 & -1 & 0 \\ -1 & 4 & -1 \\ 0 & -1 & 0 \end{matrix}$$

was chosen as a candidate after screening several other possibilities. The procedure was to apply the mask to the M-60 tank and to the scenes and then take the Fourier transform of the resulting images. Using the Laplace tank as the basis for the matched filter, the two previously discussed criteria were applied. Two versions of the Laplacian preprocessing technique were evaluated. In the first method, the Fourier transform of the absolute value of the Laplacian image was used. This we designate as the magnitude Laplacian. The second technique did not attempt to change the negative values of the Laplace image and we denote it as the signed Laplacian. The magnitude Laplacian is of interest because it presents a somewhat easier problem of implementation to the analog device.

In Table 1, the results for three filters on each of three scenes is given with respect to the S/C criteria. In general, the results indicate that the woodland presents the least problem with respect to clutter and the village the most severe. The only contradiction is the signed Laplacian which does equally well in the woodland and village. In any case, the signed Laplacian does uniformly better than the other two filters and the magnitude Laplacian is the worst of the three.

Table 1 The Results of Three Filters on Three Scenes

Filter	Signal/Clutter (DB)		
	Woodland	Road	Village
5th lobe(1)	6.8	7.1	3.7
Magnitude Laplacian	.8	.6	-.8
Signed Laplacian(2)	10.9	8.8	10.9

(1) The signal is the cross correlation between the 5th lobe filtered tank and the unfiltered tank.

(2) The signal is the autocorrelation of the Laplace tank.

Table 2 shows how each of the techniques performed against the scenes containing the 4 targets. We see that the signed Laplacian and the 5th lobe filter perform equally.

Table 2 Operational Criterion

Filter	Woodland		Road		Village	
	No. of Weapons (1)	Avg. Miss Dist. (2)	No. of Weapons	Avg. Miss Dist.	No. of Weapons	Avg. Miss Dist.
5th Lobe	4	0.25	4	1.1	4	1.0
Magnitude						
Laplacian(3)	14	0	8	1.0	4	1.0
Signed						
Laplacian(3)	4	0.25	4	1.1	4	1.0

(1) The number of weapons that would be required to score hits on all 4 targets.

(2) Miss distance in pixels averaged over the 4 targets. The targets dimensions were 36 pixels wide and 80 pixels long.

(3) Laplace operator applied to reference target and scene.

In all three scenes, the tanks were hit with the first four weapons with the miss distance averaging around 1 pixel. The miss distance refers to the Euclidean distance in pixels between the desired aim point (in our case a point on the turret of the tank) and the point on the tank at which the hit occurred. The performance of the magnitude Laplacian is again inferior to the other filters. Fourteen scans (weapon firings) of the cross-correlation plane were required to score hits on the four targets in the woodland scene and 8 scans were required for the roadside. However, the magnitude Laplacian does as well as the other two in the village. This is quite surprising since the village scene yields the smallest S/C. While the overall performance of the 5th lobe and signed Laplacian filters were better than the magnitude Laplacian, the behavior of the latter in the village scene warrants further investigation. For the remainder of this paper, only the first two filters will be studied. To this point, only the S/C allows us to discriminate between the remaining two filters, and with respect to that

criterion (Table 1) the Laplacian clearly dominates. If it is necessary to threshold the correlation plane at some intensity such that returns less than that intensity will be considered clutter, then the filter with the higher S/C should perform better. We now turn our attention to the problem of the rotational sensitivity of the two filters

#### Rotational Sensitivities

The sensitivity of the matched filter to a change in the target orientation has been a problem in the application of this technique. The optical device attempts to overcome this by storing many matched filters of the target in different aspects and performing multiple simultaneous matched filtering operations. However, the fewer the filters required the more cost effective the overall device, so that the question of rotational sensitivity remains one of interest.

We first examined the effect of rotating the filtered tank and correlating it with the unrotated tank. This is in effect the correlation that would take place if the target tank had been rotated in the scene. In the case of the Laplacian, we considered two situations; the first, in which both the reference tank and the target tank are filtered by the Laplace operator and the second in which only the reference tank is filtered.

Since the candidate filters tend to act like high pass filters, we include in the comparisons the results for the all pass or DC filter. It is clear from the results in Table 3 that the modified filters suffer significant losses due to the rotations. The 5th lobe filter and the second case of the Laplace filter are very similar. The first Laplace filter (Laplace reference vs Laplace target) is significantly worse than the other two. All the filters are of such low total energy and high frequency that it could be expected that misalignment of the target would cause significant degradation of the correlation signal. It should be emphasized that the DC filter is included here only for comparison purposes. Previous studies have shown its performance to be unsatisfactory.

Table 3 Cross-Correlation of the Rotated and Unrotated Tank (dB)

Rotation (deg)	5th Lobe	Signed Laplacian		DC
		(1)	(2)	
0	0.0	0.0	0.0	0.0
1	-0.66	-2.4	-6.9	-0.06
2	-1.3	-4.4	-1.3	-0.11
3	-2.4	-7.1	-2.3	-0.19
4	-3.4	-9.0	-3.3	-0.30
5	-4.3	-10.7	-4.2	-0.39
6	-5.0	-11.2	-5.1	-0.51
7	-5.8	-12.2	-6.1	-0.63
8	-6.4	-12.7	-7.0	-0.76
9	-6.8	-13.5	-7.9	-0.87
10	-7.5	-14.5	-8.9	-0.88

(1) Rotated Laplace tank cross-correlated with unrotated Laplace tank.

(2) Rotated Laplace tank cross-correlated with unrotated tank.

We next examined how the various filters performed in locating the tanks in the scenes. To investigate this we made up the modified versions of the matched filters from tanks rotated through 1-10 degrees and correlated these matched filters with the scenes containing the unrotated tanks. We then searched the correlation plane in the manner described in the section on the evaluation procedures.

Table 4 gives the results for the woodland scene. The superiority of the second Laplace filter is clear. Through all 10 degrees of rotation it remains quite stable, never requiring more than 5 weapons to hit the 4 tanks and holding the miss distance to less than 3 pixels. The 5th lobe filter and the first Laplace perform about equally. The first Laplace is unsatisfactory at 5° and the fifth lobe at 7°.

In the village scene both Laplace filters outperform the 5th lobe filter which is unstable even at the very small angular rotations. The performance of the 5th lobe filter in the village could be expected because of the very low S/C reported in Table 1.

The second Laplace is quite a bit better than the first Laplace with respect to the average miss distance, although at the very high rotations it does require more weapons to hit the 4 tanks. However, for rotations less than 8 degrees it is better with respect to both miss distance and weapon requirements.

DIGITAL METHODS IN THE DESIGN OF OPTICAL MATCHED FILTERS FOR TARGET RECOGNITION

Table 4 Rotational Sensitivity in Woodland Scene

5th Lobe Filter		Signed Laplace(1)		Signed Laplace(2)	
No. of Weapons	Average Miss Dist.	No. of Weapons	Average Miss Dist.	No. of Weapons	Average Miss Dist.
4	.25	4	.5	4	2.57
4	.25	4	.5	4	2.42
4	.25	5	.75	4	2.42
4	.25	5	9.7	4	2.65
4	0.5	10	7.4	4	2.65
6	6.8	12	16.8	4	2.65
10	.5	9	17.3	4	2.42
15	9.5	10	14.6	4	2.65
12	22.15	8	10.2	5	2.65
12	19.12	12	16.1	5	2.65

(1) Laplace operator applied to reference target and scene.

(2) Laplace operator applied to scene only.

Table 5 Rotational sensitivity in Village Scene

5th Lobe Filter		Signed Laplace (1)		Signed Laplace (2)	
No. of Weapons	Average Miss Dist.	No. of Weapons	Average Miss Dist.	No. of Weapons	Average Miss Dist.
4	1.3	4	1.1	4	1.4
5	1.0	4	1.1	4	1.4
15	1.0	4	1.4	4	1.4
7	1.0	5	11.1	4	1.4
20*(2)	1.4	16	8.6	4	1.4
20*(1)	41.4	6	23.7	6	1.4
20*(1)	1.4	14	14.4	9	1.3
20*(0)	---	9	12.7	12	1.4
20*(1)	22.0	17	27.6	20*(3)	1.4
20*(1)	12.0	11	15.3	20*(3)	1.4

(1) Laplace operator applied to reference target and scene.

(2) Laplace operator applied to scene only.

\* Search program concluded after 20 weapons were fired. Numbers in parenthesis represent number of hits at that time.

#### Conclusions

Various modifications of matched filters have been examined. A Laplacian was found to yield excellent results with respect to S/C and rotational sensitivities. Results of a simulation show that the Laplace filter performs best when applied only to the reference target and not to the scene. Our investigation of the optical matched filter and its modifications for target cueing and location are continuing.

#### Acknowledgement

This work was partially supported by the Air Force Office of Scientific Research under contract F49620-78-C-0051.

#### References

1. Grumet, A., U.S. Patent # 3,779,492, "Automatic Target Recognition System," December 1973.
2. Leib, K., Bondurant, R., Wohlers, M., "Match Filter Correlator Memory Techniques and Storage Capacity," Proceedings of Soc. of Photo-Optical Instrumentation Engineers, Optical Information Storage, Vol. 177, April 1979.
3. Mendelsohn, J., Wohlers, M., "Digital Analysis of the Effects of Terrain Clutter on the Performance of Matched Filters," Proceedings of Soc. of Photo-Optical Eng., Digital Processing of Aerial Images, Vol. 186, May 1979.
4. Wohlers, M., Mendelsohn, J., "Target Detection Using Hybrid Digital-Analog Correlation Techniques," Published in proceedings of MICOM Workshop on "Imaging Trackers and Autonomous Acquisition Applications for Missile Guidance," Nov. 19-20, 1979, Huntsville, Ala.
5. Pratt, W. K., "Digital Image Processing" John Wiley & Sons, New York, 1978.

## **APPENDIX F**

### **ANALYSIS OF AN OPTICAL MATCHED FILTER GUIDANCE SYSTEM FOR TACTICAL HOMING APPLICATIONS**

This paper was presented at the AIAA/NASA Conference on "Smart" Sensors, NASA Langley Research Center, Hampton, VA, November 1978. It represents an extension of the initial concepts of large capacity optical memories developed in this program to tactical homing applications.

30. ANALYSIS OF AN OPTICAL MATCHED  
FILTER GUIDANCE SYSTEM FOR  
TACTICAL HOMING APPLICATIONS (U)

By: Kenneth G. Leib, M. Ronald Wohlers, Hans K. Hinz, and Gardner Moyer<sup>+</sup>

(U) Abstract - This paper describes an Optical Matched Filter Image Correlator (OMFIC) that can identify targets and their number, and provide information about their bearing, positional coordinates, range interval, and velocity. Thus, it has potential for the missile or projectile guidance application. The OMFIC system can be implemented using holographic techniques to achieve large capacity optical memories, and lasers to achieve coherent signal processing. Real time implementation is possible using electro-optic incoherent-to-coherent image transducers. The optical memory size and real time transducer update requirements are two of the most important aspects of the OMFIC system when used for guiding a projectile. An analysis of these factors is given which shows that the memory bank requirements are manageable and within current technology capabilities. Other aspects of the OMFIC memory bank and transducer requirements are developed in the paper including a system simulation yielding CEP performance information based upon T-6 THAD test missile.

1. Introduction (U)

(U) The advent of the laser has given impetus to the development of various electro-optical approaches for missile or projectile guidance. One of the first was a semiactive guided projectile using a laser designator (Ref. 1.). More recently, artillery shells containing surveillance television systems have been demonstrated in a simulated flight (Ref. 2). These efforts and others between and since show the serious interest in projectiles which ultimately lead to "fire and forget" type of weapons. This is confirmed by the issue of a specification for at least one such projectile (Ref. 3).

(U) The Optical Matched Filter Image Correlator (OMFIC) is a system under development in which targets can be identified and selected and the resulting signals used to provide information for terminal guidance. Considering the amount of information that the system can, in principle, reveal about one or more targets, it would seem to be a logical candidate for an electro-optic missile guidance system. (See Table 1). In this

---

<sup>+</sup>Messrs. Leib and Hinz are Staff Scientists, G. Moyer is Research Mathematician, and R. Wohlers is Head, Electrophysics Laboratory of the Research Department of Grumman Aerospace Corporation, Bethpage, New York 11714.

(U) Table 1 – Information That OMFIC System Can  
Reveal About Targets (U)

- POSITIVE IDENTIFICATION OF TARGETS
- NUMBERS AND TYPES OF TARGETS
- BEARING INFORMATION
- POSITIONAL COORDINATES OF EACH TARGET
- RANGE (WITHIN AN INTERVAL)
- IF PROVIDED, SPEED AND DIRECTION OF TARGETS
- OUTPUT AVAILABLE FOR TRANSMISSION TO REMOTE STATION

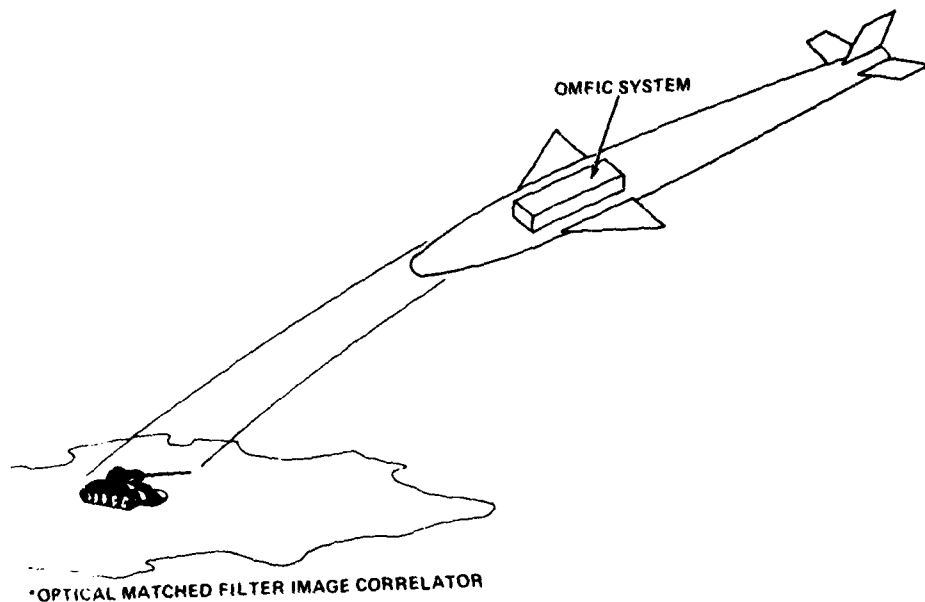


Figure 1 OMFIC\* System in Tactical Homing Applications

paper we summarize the results of an analysis on two of the chief elements of the system, present some results to date, and indicate several technology areas under investigation. These all bear upon the use of the OMFIC system for tactical homing applications. (Fig. 1)

## 2. Basic Elements of the OMFIC System (U)

(U) The OMFIC system has been described in detail elsewhere (Refs 4 and 5), but the basic elements are shown in Fig. 2. A noncoherent image (the target in the terrain) is put on a transducer that functions to convert the image into a coherent replica on a laser beam. One such device is a liquid crystal transducer, although solid crystalline ones are also available (Ref. 6). A coherent beam is then directed through the transducer to pick up the image and transfer it to a multiple holographic lens. This lens performs a Fourier transformation in replication and directs it to corresponding positions in the matched filter plane. Many views of one or more targets are stored with high density in the matched filter plane, and in some cases several are stored in each position. The input scene is compared with the stored information and when a target coincidence occurs, the corresponding correlation signals can be obtained by taking a second (but inverse) Fourier transformation. Under any circumstance, signals are observed in the correlation plane and through baseline subtraction, or thresholding, the target correlations can be detected.

(U) A priori information about the matched filter and the subsequent detection of a target give rise to target identification and positional information. This is the case since there is an almost linear relationship between input and output location and movement. Thus the information derived in the detection processor can be used to derive guidance information.

(U) From an optical point of view, the matched filter memory and input transducer are the most important elements and are the subject of this analysis.

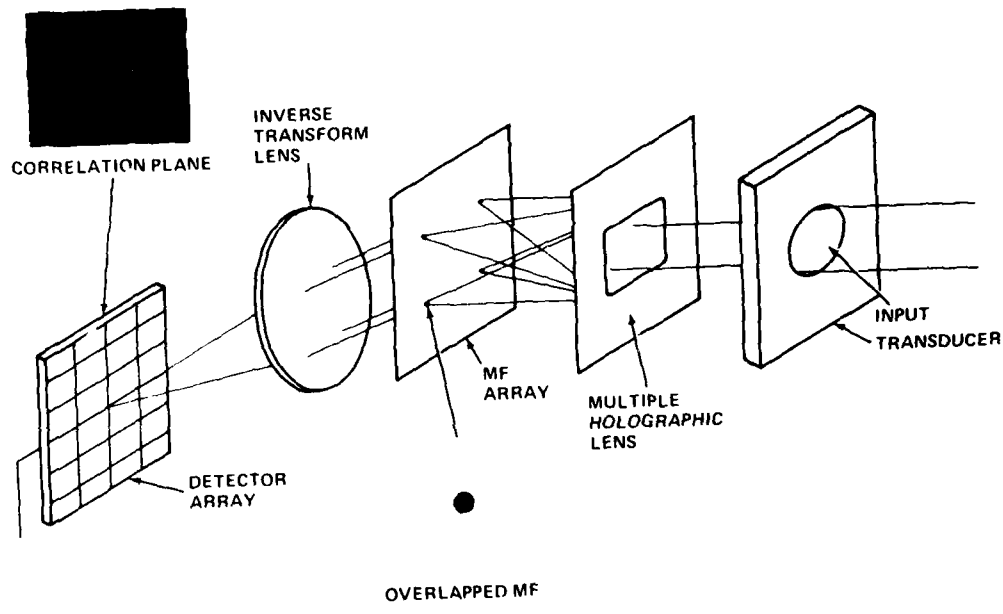
## 3. Requirements on OMFIC System (U)

(U) Figure 3 illustrates the change of image size as a function of time for a terminal guidance scenario in which the target is to be initially acquired at a range

$$R_{ACQUISITION} = 1.5 \text{ km}$$

where the missile velocity is assumed to be

$$v = 210 \text{ and } 300 \text{ m/sec}$$



OVERLAPPED MF

Figure 2 OMFIC System

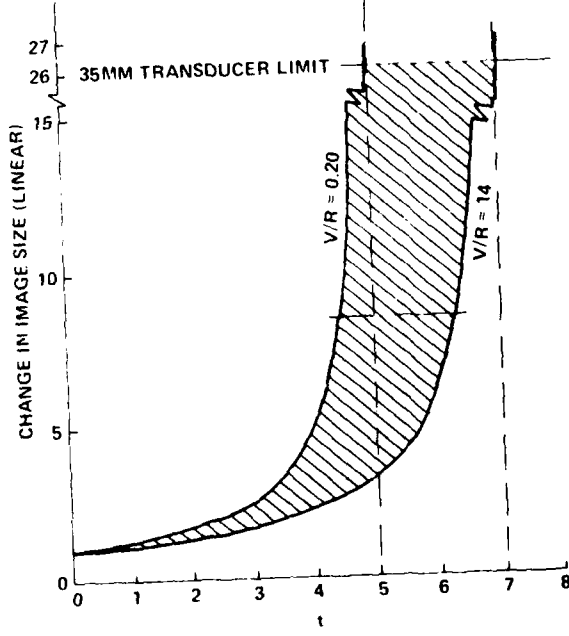


Figure 3 Image Changes as a Function of Time

(U) From this information, and knowing the discrete nature of a memory element, the number of matched filter "range bins" needed to provide complete guidance coverage to some final range to the target can be determined.

(U) Figure 3 also illustrates the changing requirement on image smear as the missile approaches the target. During flight the duration of exposure for recording the image on the transducer is comparable to that for photographic exposures in aerial reconnaissance cameras without the benefit of image motion compensation. The percentage enlargement smear is given by

$$S = V \left[ \frac{1}{(1 - Vt)^2} \right] \Delta t \times 100 \quad (1)$$

where  $V = v/R$  and  $\Delta t$  is the transducer write time.

(U) Since there is no a priori knowledge of a targets aspect, allowance must be made in the memory bank for all views likely to be encountered. Figure 4 illustrates the variation in matched filter response for an M-60 Tank target vs orientation. This parametric sensitivity like any others of concern, shows that the parametric limits vary according to the degree of discrimination desired. One often accepts a (-3dB) variation. Thus, if it were desired to identify an M-60 among other tanks, an orientational sensitivity of  $\pm 8^\circ$  is the maximum for normal discrimination so that  $\frac{360}{16} = 23$  whole filters would be required for a full  $360^\circ$  coverage. In a similar fashion, we could determine the sensitivity of the matched filter to scale change, we will define  $\alpha$  to be the fractional linear scale change to produce a (-3dB) change in correlation. The number of matched filters can then be determined in order to provide both scale and orientation coverage from the equation

$$\# MF = W \left[ \frac{\log F}{\log \left( \frac{1 + \alpha}{1 - \alpha} \right)} + 1 \right] \quad (2)$$

where  $F$  is the total linear size variation over the guidance path and  $W$  is the factor corresponding to orientation, e.g.,  $W = 23$  in the above.

#### 4. Selected Results of Analysis (U)

(U) Using Eq. (2), the size of the memory bank can be computed. The results are summarized in Table 2 for various combinations of orientation and scale. It is quite apparent that as the degree of discrimination increases, exemplified by decreasing scale and orientation sensitivities, so does the number of required matched filter positions.

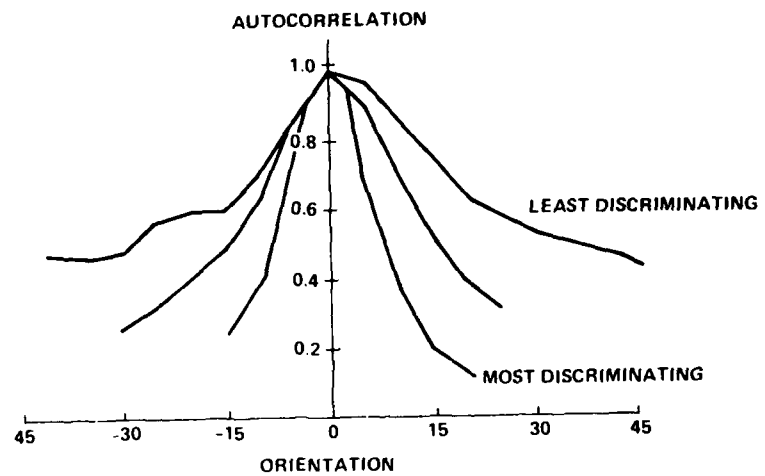


Figure 4 Representative Sensitivity Response

(U) Table 2 – Memory Requirements For Continuous Range Coverage  
1.5 KM – 50 M (U)

SCALE SENSITIVITY	NUMBER OF FILTERS TO COVER SCALE AND:		
	8° ORIENTATION	10° ORIENTATION	12° ORIENTATION
10%	397	311	259
15%	271	213	177
20%	208	163	136

(U) The image smear as a percentage of the image size when the shutter is opened is given by Eq. (1) and has been computed for two velocity ratios  $V = v/R$  and  $\Delta t = 10$  and 50 milliseconds. Then two exposure times were chosen because they bracket near term anticipated and current transducer technology. The results are shown in Fig. 5. It is not surprising that shorter exposures result in less smear, nor that near impact the smear is greatest.

(U) In carrying out our analysis it was initially assumed that either the transducer cycling or the guidance update requirements would dictate the overall system cycling time. For the transducer, the cycling time was set equal to the time interval,  $T$ , that the target is in the "final range bin" matched filter with nominal range  $R_0$ . The result is

$$T = \frac{2\alpha}{1-\alpha^2} \frac{R_0}{v} \quad (3)$$

(U) Using two velocity ratios  $V$  and several parametric sensitivity increments we obtain the results of Table 3.

(U) It can be seen that under the conditions given, the most severe transducer requirement called for is akin to TV frame rates. As is shown below, the guidance update rate is less severe, so, overall, the decision becomes more one of properly selecting memory elements since neither fast transducer operation nor a large number of memory positions are necessarily required.

(U) One method used to assess the target identification aspects of system performance was to determine the probability of detection as a function of false alarms. This was done by using terrain scenes such as those in Fig. 6. Then, the (signal/clutter) ratio in the correlation plane was determined, and the false alarm rate computed for decreasing threshold levels. A relationship between the target detection probability as a function of threshold level and number of target parameters that are varying statistically was derived (Ref. 7). Equating the two by eliminating the threshold yields the target detection probability as a function of the percentage false alarms. Selected results from this analysis are given in Table 4.

#### 5. Results for Complex Terrain Target (U)

(U) Although the present analysis is for the tactical scenario involving a military target, one might consider an entire scene as the target (Ref. 8) such as a power plant region. One scene obtained from a TV monitor is shown in Fig. 7 along with the matched filter and correlation spot. The tabular insert gives the restrictions on the various parameters of concern. A memory bank providing for continuous coverage with-

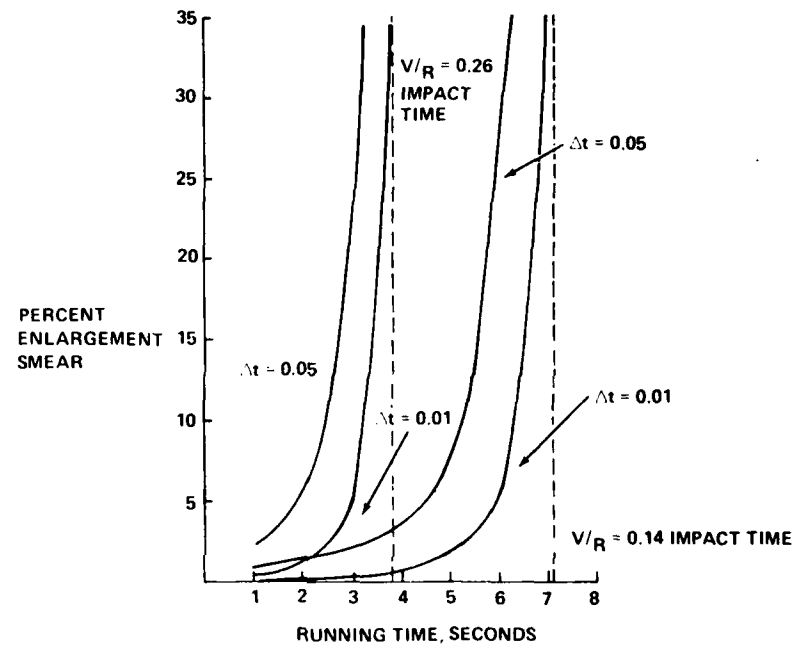


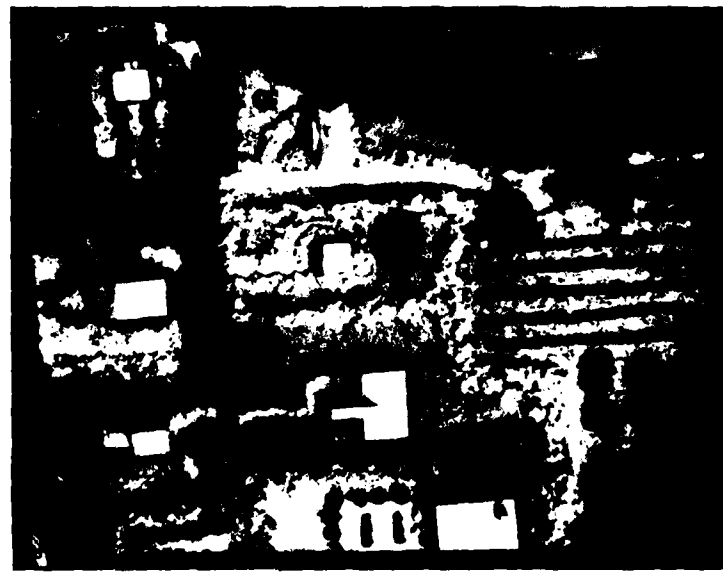
Figure 5 Enlargement Smear As A Function of Flight Time

(U) Table 3 – Transducer Update Requirements (U)

VELOCITY RATIO (v/R)	IMAGE SCALE SENSITIVITY INCREMENT ( $\alpha$ )	REQUIRED UPDATE INTERVAL (MS)	FINAL RANGE "BIN" INTERVAL (M)	IMPACT TIME (SEC)
0.14	0.05	30.54	64 – 70	7.14
	0.10	28.69	29 – 35	
	0.15	27.04	18 – 24	
	0.20	27.53	14 – 20	
0.20	0.05	31.91	95 – 105	5.00
	0.10	30.00	46 – 56	
	0.15	25.64	26 – 35	
	0.20	28.90	22 – 32	



(A) WOODLAND



(B) VILLAGE

Figure 6. Representative Test Terrains

in these restrictions would require 354 matched filter positions, a number comparable to the requirements of a vehicle.

#### 6. Large Capacity Optical Memories for Correlators (U)

(U) In analog correlators storage is in the format of Fourier transform holograms, and large numbers of them are required so that the question of information capacity is required but is generally undefined. We can however, consider the basic element of storage, the matched filter. It is usually optimized at some spatial frequency, and to obtain a prescribed level of correlation, say 95%, one needs additional spatial frequencies. This can be described by some factor  $Nv_o$  where N is a positive number  $\geq 1$  and  $v_o$  is the optimizing spatial frequency. Also, filters can be geometrically placed to maximize the use of storage space. Furthermore, such techniques as spectrum bifurcation, filter addition and various angles of the reference beam all help to increase the overall capacity. Considering these factors, a capacity can be defined by the equation

$$C_A = \frac{25 S P G}{(N v_o \lambda F)^2} \text{ matched filters/cm}^2 \quad (4)$$

where the factors S, G, P represent spectrum splitting, geometrical placement and overlaying, and F is the transform lens focal length. A practical set of values is  $S = 1$   $G = 1.3$ ,  $Nv_o = 8.3$   $P = 4$ ,  $\lambda = 0.488 \mu\text{m}$  and  $F = 25 \text{ mm}$  to yield  $2500 \text{ MF/cm}^2$ . Thus, one can see that large capacities are not out of the question, and that the 250-350 required for the scenarios presented in this analysis are a small fraction of attainable densities.

(U) Equation 4 does incidentally also apply to the case of bit-by-bit serial recording for a computer usage. In that case for  $G = 1$ ,  $Nv_o = 0.063$  and  $P = 1$ , a system would yield  $10^6 \text{ bits/cm}^2$  a value often cited in the literature.

(U) There is a practical aspect to this and it implies that while the memories required for a given scenario are not approaching theoretical limits, they are exceeding our ability to normally make them. Obviously, resort to computer generation may be necessary, but for missiles a dedicated system for such a "production line" is feasible.

(U) Table 4 - Probability Of Detection of M-60  
Tank in Terrain (U)

TERRAIN	THRESHOLD LEVEL NO. 1		THRESHOLD LEVEL NO. 2	
	% FA	% P <sub>D</sub>	% FA	% P <sub>D</sub>
WOODLAND	1.00	97.2	10.0	99.9
VILLAGE	1.70	90.0	14.0	99.9



POWER PLANT IMAGE FROM TV MONITOR

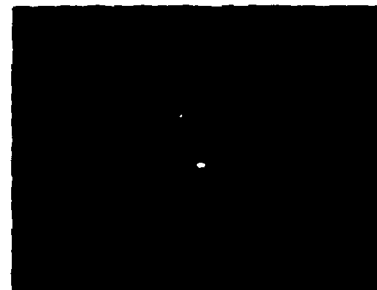
PARAMETRIC STABILIZATION RESTRICTIONS  
AFTER LOCK ON

PARAMETER	INTERVAL
RANGE	0.9 - 2.000 km
ASPECT	•2.38
ROLL	•1
PITCH	•2
YAW	•2

REQUIRES 354 MF POSITIONS



MATCHED FILTER



AUTO CORRELATION

Figure 7 Terminal Homing Scenario With Complex Target

Matched filter density can be increased in a number of ways; these are:

- Coherent addition
- Noncoherent addition
- Interlace
- Off-set reference beams
- Off-set (signal and reference) beams

or some combinations of these, as well as a simple parallelling of complete channels. Several of these are illustrated in Fig. 8 and are self-evident.

(U) Each has its particular advantages and disadvantages both in fabrication and complexity of reading out. A current study is in progress directed toward optimizing the memories for Air Force applications.

#### 7. Missile Flight Simulation and Guidance Update Determination (U)

(U) The U.S. Army's T6 test missile was used as a model for our simulation, with data and equations taken from Refs. 9-11. The T6 missile is 65 inches long, 6 inches in diameter and weighs 71 pounds at launch. Ground launched, it has a maximum velocity of 1300 ft/sec and a range of about 5 miles. It can also be launched from helicopters, the scenario used in the OMFIC analysis.

(U) The simulation is two dimensional, includes rigid body and control actuator dynamics, but neglects launch rail dynamics, thrust acceleration, and seeker head dynamics. The T6 autopilot is replaced by a simple pitch damper, a gravity bias which is a function of velocity and a guidance law based on proportional navigation. The target (tank) is modeled as a point source moving at a constant 30 ft/sec velocity.

(U) Preliminary studies were made in which the initial velocity (600 to 1500 ft/sec) and initial range (3000 to 25,000 ft) were varied. In all cases the initial altitude was 600 ft and the flight path horizontal. Using proportional navigation with exact line of sight rate information the missile is well behaved with miss distances usually well below one foot.

(U) The seeker head for the OMFIC guidance system, however, does not have exact, nor continuous, line of sight rate information. Instead, the processing of visual information is completed every  $\Delta t_g$  seconds, and because of image blowup, this processing stops at a range of  $R_F$  feet, and the missile is guided only by previously stored information. This is shown in Fig. 9. For this and all other scenarios only one initial velocity, 800 ft/sec, and one initial range, 1500 meters, was

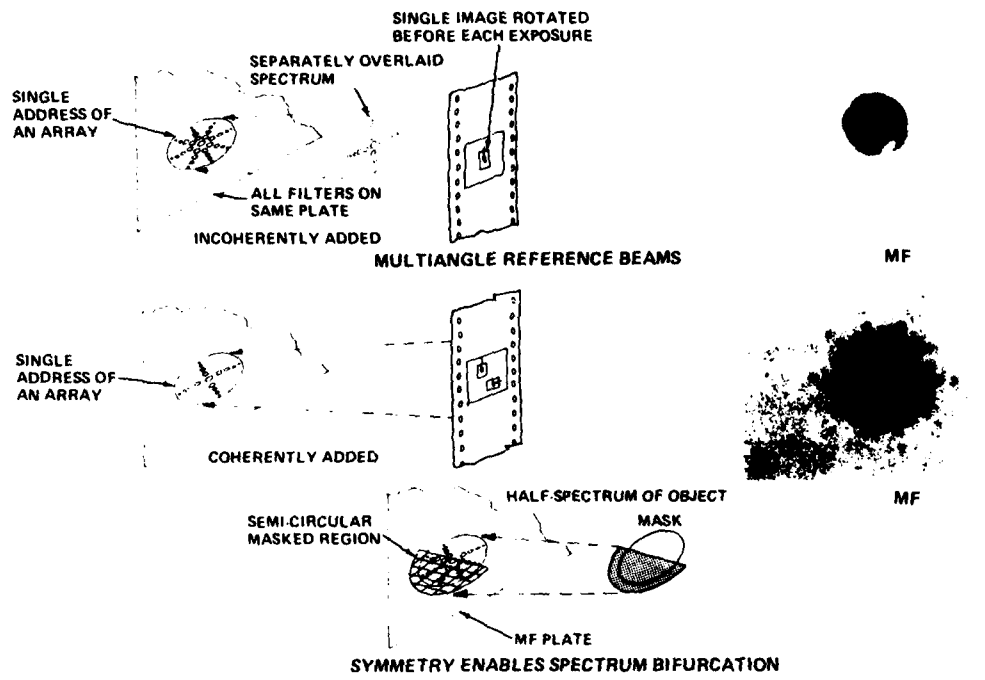


Figure 8 Techniques for Large Optical Memories

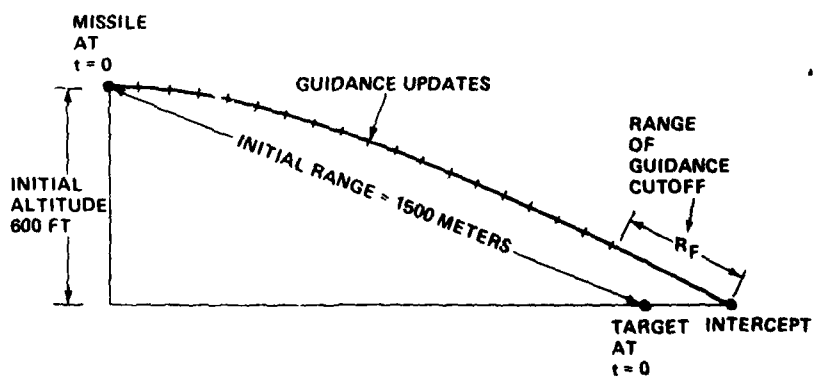


Figure 9 Scenario for T6 Missile Simulation

studied. The seeker head measures the angle  $\phi + \theta$  (Fig. 10), subtracts the gyro-measured angle  $\theta$ , and stores the line of sight angle  $\phi$ . This is repeated every  $\Delta t_g$  seconds. A simple parabolic curve fit is made from three consecutive points,

$$\begin{aligned}\phi &= a + bt + ct^2 \\ \dot{\phi} &= b + 2ct\end{aligned}$$

and  $\dot{\phi}$  is extrapolated and used during the next interval. This procedure is repeated at every guidance update. The parameters  $\Delta t_g$  and  $R_g$  were varied and the results shown in Fig. 11 (no turbulence). Only combinations of  $\Delta t_g$  and  $R_g$  below this curve satisfy the one foot miss distance requirement.

(U) To evaluate the missile in a noisy environment, turbulence was added using a Dryden gust spectrum (Ref. 12) with a 6 ft/sec RMS gust velocity. Smoothing was added to the autopilot by using an N-point least-squares parabolic curve fit for  $\phi$ . N was varied from 3 to 11 (N=3 is unique, not least-squares). For each combination of  $\Delta t_g$ ,  $R_g$ , and N, five runs were made, each with a different 6 ft/sec RMS gust time history. RMS miss distances were calculated and the same one foot miss criteria was used. These results are shown in Fig. 11 (turbulent atmosphere). The number of points N is not very significant, with slight deterioration for N greater than six. Even N = 3 (no smoothing) was noted to be as good or better than the larger values.

(U) As an alternative to proportional navigation, pursuit guidance was also evaluated. Pursuit guidance is not as good, however, it is based on line of sight angle (not rate) information. Numerical differentiation of  $\phi$  to get  $\dot{\phi}$  is always risky. Assuming, at first, exact and continuous information for  $\phi$  and no turbulence, it was impossible to obtain a pursuit guidance system that would satisfy the one foot miss distance.

(U) A least-squares parabolic curve fit is a crude way to smooth discrete information; however, feasibility has been proven. Should the OMFIC guidance system some day reach the design stage, a more sophisticated method will surely be developed. Within the limits of this analysis then, it can be seen that the update intervals for small CEP (equivalents) exceeds those required by the transducer. Thus, the guidance update is the determining time constant.

#### 8. Preliminary Configurations (U)

(U) A preliminary configuration of the OMFIC - guided missile system concept is shown in Fig. 12.

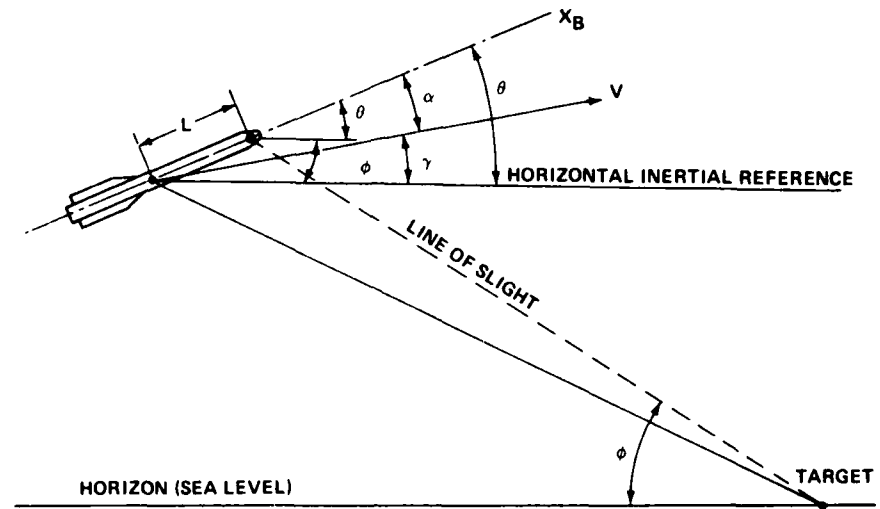


Figure 10 Angle and Line of Sight Geometry

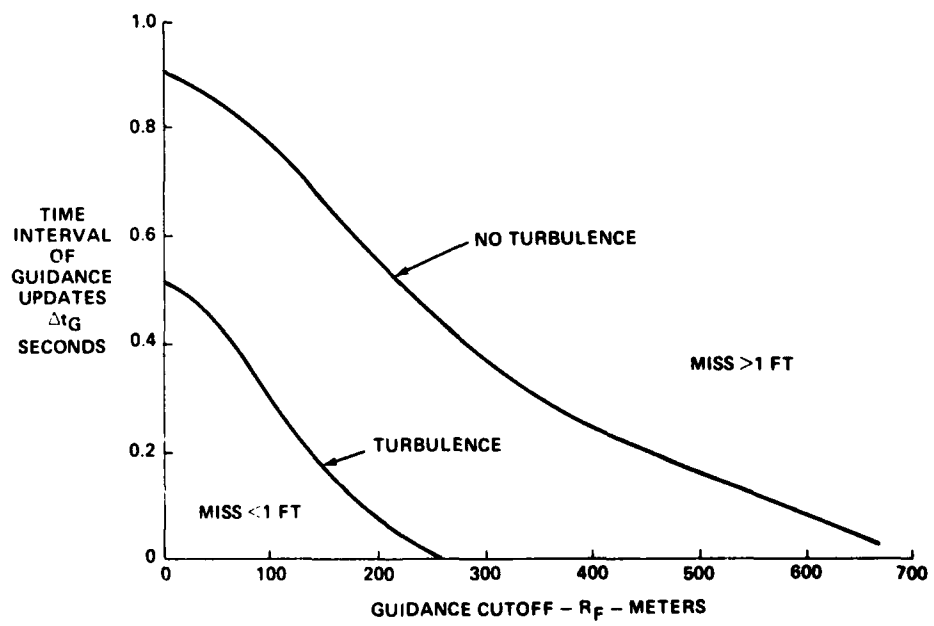


Figure 11 RMS Miss Distances With and Without Atmospheric Turbulence

(U) At the acquisition range turn-on, the master control unit initiates a clock generator from which all functions are timed. This unit turns power on and causes the various sequences to start. These include the transducer cycling, detector array scanning, laser cycling, detection, and thresholding controls.

(U) With all units powered and cycling, the shutter opens and the transducer is powered so that an image is stored. The transducer is postulated as cycling at twice per second based upon the preceding analyses. After the read cycle is complete, the shutter is closed and the laser activated. This enables the stored image to spatially modulate the collimated laser beam. The OMFIC operation proceeds as described earlier. The image is Fourier transformed by the holographic transform lens which presents the spectrum simultaneously to all positions of the matched filter memory bank. At the latter, correlation of the image takes place if a tactical target of interest is present. The inverse transform of the product of the matched filter OTF and image OTF is taken and presented to the detection array which has been activated and scanned. Activation includes battery power as well as threshold setting. Signals exceeding threshold activate the target decision logic where it is determined whether the target is a primary, secondary, or tertiary one. This decision is based upon information which has been stored a priori in the matched filter during fabrication. At the same time that the target decision process is taking place, the positional coordinates are being generated.

(U) Upon the target position decision, the offset, or guidance requirement to reduce offset, is determined. This information is then used to generate guidance power signals which effect an appropriate aerodynamic surface correction.

(U) The OMFIC system was laid out in the confines of the T6 missile previously considered in order to establish the reasonableness of construction. This layout is shown in Fig. 13 and is based mostly upon laboratory parameters rather than trade off studies. For example, considerable progress has recently been made in extending the coherence length of semiconductor lasers. When suitable, the use of this laser will have significant impact in reducing the size and cost of the entire package.

#### 9. Summary

(U) The OMFIC system has reached a state of achievement where its application to tactical homing applications can be considered and their performance analyzed. The two most critical elements of the OMFIC technology are the memory and the transducer. It was shown that memories are manageable and the required transducer cycle times are achievable. Preliminary sizing for the Terminal Homing Accuracy Demonstration (THAD) missiles shows the OMFIC system to be a reasonable fit.

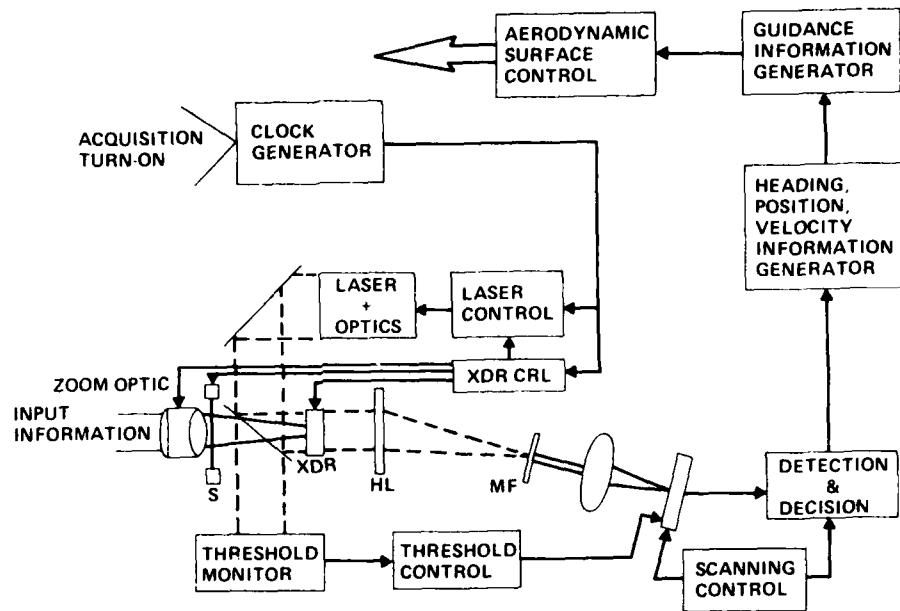


Figure 12 OMFIC-Guided Missile System Concept

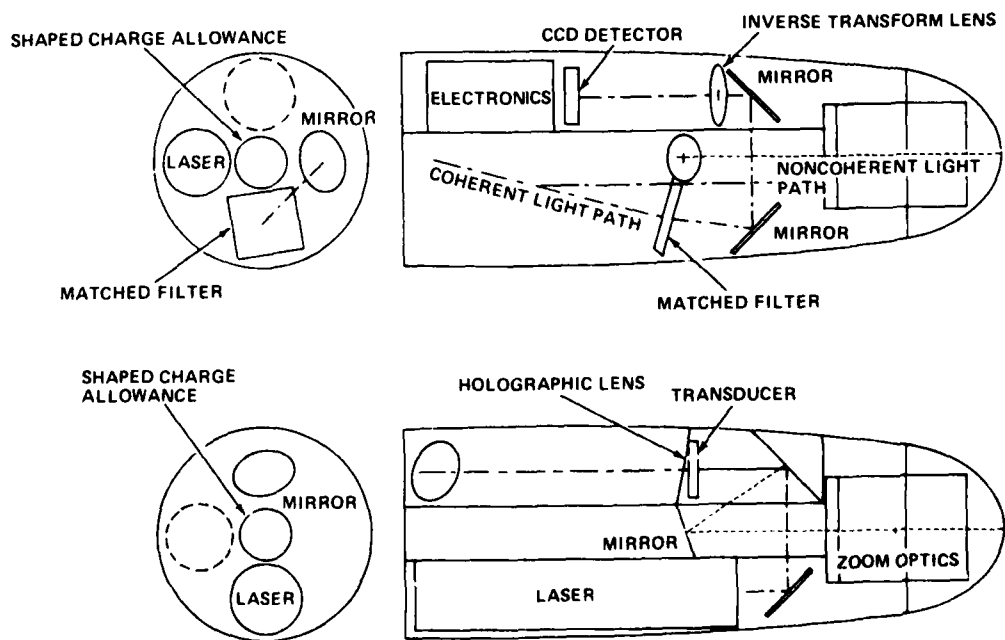


Figure 13 Preliminary Configuration of T6 (THAD) Missile With OMFIC Mounting

10. References (U)

1. G. Royce, "Gun Launched Guided Projectiles (U)," Vol. III, Fifth Conference on Laser Technology, Monterey, California, April 1972 (CONFIDENTIAL).
2. E. Ohlhoff et al., "Artillery Launched Television," SPIE/SPSE Conference East, Reston, Virginia, March 1976.
3. "System Specification for Projectile, 155 mm Cannon Launched Guided, XM712 (U)"; Specification No. WC-A-007-001-X, 25 June 1976. (CONFIDENTIAL).
4. A. Grumet et al., "Optical Matched Filter Image Correlator," Grumman Research Department RE-512, Final Report on Contract DAAK-02-74-C-0275, May 1975.
5. K.G. Leib et al., "Optical Matched Filtering Techniques for Automatic Interrogation of Aerial Reconnaissance Film," Grumman Research Department Report RE-524, Final Report on Contract DAAG53-75-C-0199, September 1976.
6. R.A. Sprague and P. Nisenson, "The ITEK PROM - a Status Report" Itek Corporation 1977.
7. K.G. Leib et al., "Baseline Test of a Matched Filter Correlator for Screening Aerial Reconnaissance Film," Electronic Industries Association Conference on Automatic Image Pattern Recognition, Silver Springs, MD., May 1977.
8. K.G. Leib and J. deCarlo "Optical Correlator Memory Bond Terminal Homing Missile Scenario against a Complex Target" Grumman Research Department Memorandum RM-660, August 1978.
9. J.D. Aitken et al., "T6 Missile Description," Technical Report RG-73-18, U.S. Army Missile Command, Redstone Arsenal, Alabama, August 1973.
10. R.F. Ball et al., "An Engineering and Programming Guide for a Six Degree of Freedom, Terminal Homing Simulation Program," Technical Report RG-73-22, U.S. Army Missile Command, Redstone Arsenal, Alabama, October, 1973.
11. Anon., Computer program listing of Monte-Carlo point target terminal homing simulation program, received from J.P. Leonard, U.S. Army Missile Command, Redstone Arsenal, Alabama, program listing dated August 1, 1977.

AD-A108 555

GRUMMAN AEROSPACE CORP BETHPAGE NY RESEARCH DEPT

F/G 9/2

INVESTIGATION OF LARGE CAPACITY OPTICAL MEMORIES FOR CORRELATOR--ETC(U)

F49620-78-C-0051

OCT 81 K G LEIB, J MENDELOHN

AFOSR-TR-81-0802

NL

UNCLASSIFIED

RE-634

343  
AFOSR  
1981



END  
DATE FILMED  
1 82  
DTIG

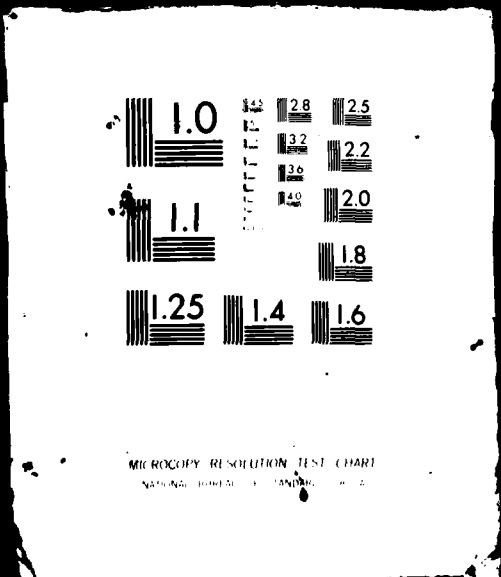
3 OF 3

D-A

108555

12. C.  
M.  
P.  
W.

Portic  
Solid  
Resear



2. C.R. Cholk et al., "Background Information and User Guide for MIL-F-8785B (ASG), Military Specification-Flying Qualities of Piloted Airplanes," AFFDL-TR-69-72, Flight Dynamics Laboratory, Wright-Patterson AFB, August 1969.

#### ACKNOWLEDGMENT

Portions of this work have received support from the Electronic and Solid States Sciences Directorate of the Air Force Office of Scientific Research under Contract F49620-78-C-0051.